On the Mechanical Design, Thermal Management, and Packaging of High Power Density Automotive Traction Inverters

On the Mechanical Design, Thermal Management, and Packaging of High Power Density Automotive Traction Inverters

Jigar Mistry, B.Sc

A Thesis submitted to the department of Electrical and Computer Engineering and the school of Graduate Studies at McMaster university in partial fulfilment of the requirements for the degree of Masters of Applied Science

McMaster University

Masters of Applied Science, Electrical and Computer Engineering

Hamilton, Ontario, Canada

Title: On the Mechanical Design, Thermal Management, and Packaging of High Power Density Automotive Traction Inverters

Author: Jigar Mistry

Supervisor: Dr. Ali Emadi

Number of pages: cxxviii, 128

This work is dedicated to my Parents, Grandparents, Family and Friends

Abstract

In order to reduce the impact of the adverse effects of climate change caused by excessive emission of greenhouse gases, it is important to move towards developing cleaner alternatives to technologies that have been relying on fossil fuels. This means electrification of transportation industry and the use of reusable Battery Energy Storage System (BESS) and relying more on solar, wind, hydroelectric and nuclear energy generation. At the heart of this electrification and shift to renewable energy lies advancement of Power Conversion Unit (PCU) and utilization of its abilities to full extent, specifically inverter technology. Inverters help in converting Direct Current (DC) power to Alternating Current (AC) power and vice versa depending on the application. In Battery Electric Vehicle (BEV) and Hybrid Electric Vehicle (HEV) the inverter is used to convert the DC power from the battery pack to AC power for the motor during driving and vice versa during regenerative braking. Similarly inverters are used in solar power generation to convert the AC power from the solar panels to AC power for the grid.

For wind, hydroelectric and nuclear power generation the inverters are used because even though the power output is AC it widely changes depending on the wind speed in the case of wind generators, water flow rate in hydroelectric generators and steam generation for nuclear power generation. The inverters take this widely varying power and convert it to smooth and consistent AC power that can be passed on to the grid.

This widespread adaptation of cleaner and greener electrified technology has accelerated the development of Inverters and they have steadily grown in their performance. Inverters contain semiconductor switching devices that help in the AC/DC or DC/AC power conversion. Historically Silicon (Si) Insulated Gate Bipolar Transistor (IGBT), commonly known as IGBT switches have been used for most automotive traction inverter applications. Recently, in an effort to increase power density and efficiency Wide-Band gap (WBG) devices such as Silicon Carbide (SiC) and Galium Nitride (GaN) Metal Oxide Semiconductor Field Effect Transistor (MOSFET) have started to replace IGBT switches.

While the power electronics have improved in their power density and efficiency, in order to fully utilize these switching devices to their full potential, it is important to provide adequate thermal management. This is because, even though the WBG devices have higher efficiency in general, as the power increases the heat dissipated due to losses also increases, and performance of these switching devices is directly tied to their junction temperature among other factors. Thus the full efficiency cannot be realized if the switching devices are running hotter.

Therefore, it is important to also scale the efficiency and performance of the thermal management system that goes along with power electronics. Additionally, the switching devices and the thermal management needs to be contained inside a housing that can withstand the harsh operating conditions and provide protection from the environment and mechanical vibrations.

This thesis aims to provide a detailed analysis on the development of a 120kW, and 250kW inverter with a cooling system integrated into the housing. In order to optimize for performance, reduce weight and volume, design tools such as Computational Fluid Dynamics (CFD) and Finite Element Analysis (FEA) are used in tandem with analytical equation driven solutions. This approach helps in creating fast and accurate thermal models that can be implemented in real time rather than simply relying on just CFD analysis. The thesis also outlines some of the basic Design For Manufacturing And Assembly (DFMA) rules that should be followed to ensure that the design can be manufactured and assembled with minimum cost and complications. Lastly, a prototype of 120kW inverter is built considering automotive standards as it represents some of the strictest, safest and harshest environments in which an inverter is being used. The prototype is then used to further investigate and validate the effectiveness and reliability of the tools and techniques described in this thesis.

The thermal management is integrated into the housing not only because the housing acts as heat sink that spreads and dissipates the heat away from the switching devices, but also because it provide mechanical structure and rigidity to the housing, protecting it from mechanical loads and vibrations.

Acknowledgments

I would like to express my gratitude to my supervisor Dr. Ali Emadi for his support and guidance. He has always pushed me to be the best and develop my skills as an engineer and a student. I am glad that he accepted me into his lab as a research assistant where I was given great opportunities to learn and contribute towards some of the most advanced engineering projects. This research was also undertaken, in part, thanks to funding from the Canada Research Chair in Transportation Electrification and Smart Mobility.

I would like to thank my parents Ashish and Nehal, my grandparents Bhaskarrai and Jashumati for their continuous support, love and kindness throughout my life. Words cannot describe how grateful I am to have parents and grandparents like you, you all mean the world to me. I would also like to thank my friends Mansi and Saksham for always being there for me and supporting me. All of you have always encouraged me to be the best version of myself, without you all I couldn't be where I am today.

I would also like to thank Peter Azer and Alex Wang for your support, guidance and all the help throughout my time at McMaster Automotive Resource Center (MARC).

Lastly, I would like to thank all my Professors, teammates and co-workers at MARC. I am grateful for all your teachings, help and advice.

Contents

List of Figures

List of Tables

Acronyms

AC Alternating Current

ANPC Active Neutral Point Clamped

BESS Battery Energy Storage System

BEV Battery Electric Vehicle

CAD Computer Aided Design

CAN Controller Area Network

CFD Computational Fluid Dynamics

CHS Capacitor Heat Sink

DC Direct Current

DFMA Design For Manufacturing And Assembly

DMLS Direct Metal Laser Sintering

DOE Department of Energy

DOF Degrees of Freedom

ECU Electronic control Unit

EMI Electromagnetic Interference

ESL Equivalent Series Inductance

ESR Eqivalent Series Resistance

EV Electric Vehicle

FDM Fused Deposition Modeling

FEA Finite Element Analysis

GA Genetic Algorithm

GaN Galium Nitride

HEV Hybrid Electric Vehicle

HVDC High Voltage Direct Current

ICE Internal Combustion Engine

IGBT Insulated Gate Bipolar Transistor

MARC McMaster Automotive Resource Center

MOSFET Metal Oxide Semiconductor Field Effect Transistor

OEM Original Equipment Manufacturer

PCB Printed Circuit Board

PCU Power Conversion Unit

PPS Polyphenylene Sulfide

PWM Pulse Width Modulation

Si Silicon

SiC Silicon Carbide

SPI Serial Peripheral Interface

SPWM Sinusoidal Pulse Width Modulation

SVM Space vector modulation

THD Total Harmonic Distribution

TIM Thermal Interface Material

VSI Voltage source Inverter

WBG Wide-Band gap

Symbols

A Area

A_{fb} Area of the entire fin base

A_{hd} Hydraulic area

α_l Coefficient of thermal expansion

α Rate of heat diffusion

C Damping coefficient

c_p Specific Heat capacity

D Diameter

$D_{cp,id}$ Copper pipe inside diameter

$D_{cp,od}$ Copper pipe outside diameter

D_{fin} Diameter of the fin

D_h Hydraulic diameter

ρ density

ε Roughness

η_{fin} efficiency of fins

$f(t)$ Force as a function of time

f_f Friction factor

f_{fin} Friction factor for staggered fined geometry

g Gravitational acceleration

G_w Closes horizontal distance between two fins

h Heat transfer coefficient

H_{fb} Height of the fin base

H_{fin} Height of the fin

h_{fin} Heat transfer coefficient around one fin

h_{fins} Heat transfer coefficient around the fins

h_L Head losses

h_{Lmajor} Major head losses

h_{Lminor} Minor head losses

k Thermal conductivity

k_{co} Thermal conductivity of the coolant

K_L Minor loss coefficient

k_{RFB} Thermal conductivity of the entire rectangular finned base

K_{st} Stiffness

l Pipe length

L_c Characteristic length

L_{fb} Entire length of the fin base

l_{fb} Length of the fin base surrounded by the coolant

l_{fin} Length of the fin

M Mass

$\dot{m}$ Mass flow rate

$\dot{m}_{CPFs}$ Mass flow rate across circular pin fins

$\dot{m}_{fin}$ Mass flow rate across rectangular fins

μ Dynamic viscosity

N_{fins} Number of the fins

N_L Number fin rows lengthwise

N_W Number fin rows widthwise

Nu Nusselt number

Nu_{fins} Nusselt number of staggered pin fins

ΔP Pressure drop

p Perimeter

p_{hd} Hydraulic perimeter

P_{in} Inlet pressure

P_{out} Outlet pressure

Pr Prandtl number

Q_{cond} Heat transfer through conduction

Q_{conv} Heat transfer through convection

Q_l Power loss

R_{cond} Conductive thermal resistance

R_{conv} Convective thermal resistance

$r_{cp,min}$ Minimum copper pipe bend radius

$R_{ds,on}$ Transistor On-state resistance

R_{fb} Thermal resistance of the fin base

R_{fin} Thermal resistance of the fin

R_{fins} Thermal resistance of the fin and the exposed are of fin base

R_{RFB} Thermal resistance of the Rectangular finned base

R_{th} Thermal resistance

Ra Surface Roughness

Re Reynolds number

Re_{max} Max Reynolds number corresponding to V_{max}

$\ddot{S}$ Acceleration

S_D Diagonal distance between two fins

$\dot{S}_{gen}$ Entropy generation

S_L Lengthwise distance between two fins

S_W Widthwise distance between Two fins

SA_{CPF} Surface area of a circular pin fin

SA_{RF} Surface area of a rectangular fin

t Time

T_{amb} Ambient temperature

T_j Junction temperature

T_s Surface temperature

V Fluid velocity

$\dot{v}$ Volume flow rate

V_{dc} Dc-Link voltage

V_{in} Inlet fluid velocity

V_{max} Maximum flow velocity around the fins

V_{out} Outlet fluid velocity

V_u Entrance fluid velocity

ω_i Angular frequency

W_{fb} Entire width of the fin base

w_{fb} width of the fin base surrounded by the coolant

w_{fin} Width of the fin

y_m Vertical distance between two MOSFETs

z Elevation

Chapter 1

Introduction

1.1 Motivation

In order for the electrified technology to succeed and compete with traditional fossil fuel powered technology, it is important to significantly increase the power density and efficiency. However simply improving the power density isn't enough, because with high power density comes higher power losses, even at very high efficiency. This means that a more aggressive thermal management system is required. The thermal management adds additional weight to the system and ultimately impacts the power density of the whole package. For example, the existing BEV are much heavier than Internal Combustion Engine (ICE) vehicles because the batteries used even in the most advanced BEV have a fraction of the power density when compared to fossil fuels. This means that a bigger battery is needed to achieve acceptable driving range when compared to ICE vehicle.

While, there are many advances being made in effort to improve the battery technology, it is also important to save weight wherever possible. One such target is the inverter inside the Electric Vehicle (EV). Typically after the battery pack, the second most critical component of a EV is the Inverter. Therefore, it is important to fully optimize the inverter design to minimize the weight and volume while increasing efficiency and performance. This can be achieved by designing a compact, yet optimal cooling system that provides the necessary thermal management to all the components that need cooling.

There are many solutions to designing a thermal management system. However, most of the existing solutions rely heavily on just CFD for the design process, and because CFD uses FEA at its core to reach solutions it is very challenging to incorporate any optimization tools or techniques to drive the cooling system design. Instead most common method used in design a cooling system is to iterate on a few key parameters of a cooling system and then select the best among them.

This thesis presents a partial equation driven cooling system geometry that can be then optimized to maximize the coolant flow rate, heat transfer rate and minimize pressure drop, while the rest of the cooling system geometry is designed based on traditional techniques such as iteration of key parameters to achieve best design. This combined method saves significant amount of computational time, design effort and produces truly optimal design solutions.

Similarly, the inverter housing also needs be as compact and light as possible, while being able to provide protection against dust, water and vibrations. Additionally, Inverters have many essential components enclosed inside them, and the optimal arrangement of these components is crucial as it determines volume, weight manufacturing and assembly feasibility of the entire inverter. By strategically organizing the components inside the housing multiple design goals can be realized such as providing thermal management and structural rigidity, improved power density, while maintaining low footprint, volume and weight.

1.2 Thesis Objectives and Contributions

The main objective of this thesis is to provide comprehensive guidelines and techniques to follow when developing and designing high power automotive traction inverters that can be assembled and manufactured with minimal challenges. The main contributions to realize these goals are listed below

1. Comprehensive analysis on the thermal management system design
2. Strategical integration of thermal management to improve power density
3. Analysis of mechanical loads subjected to the inverter
4. Designing and prototyping inverters to evaluate the proposed guidelines and techniques.

1.3 Thesis Outline

The thesis consists of 6 chapters including the introduction chapter. The introduction Chapter provides motivation behind designing an efficient thermal management system, and a light, strong and low volume inverter housing. Chapter 2 outlines all the main components of a high power traction inverter. The thermal management of a 120 kW SiC 3-level ANPC inverter is discussed in Chapter 3, and the numerous ways in which switching devices can be cooled are presented along with techniques to generate optimal designs. Next, Chapter 4 discusses inverter packaging to achieve higher power density, Thermal management integration and inverter housing design is presented for the 120 kW SiC 3-level ANPC inverter and a 250kW SiC 2-level inverter. Chapter 5 analyses the mechanical loads on the inverter Finally, Chapter 6 concludes the thesis and discusses future work to improve upon the design process of a inverter.

Chapter 2

High Power Automotive Traction Inverters

2.1 Power Components

There are four main power components in an Inverter, these components are the switching devices, DC-link capacitor, AC and High Voltage Direct Current (HVDC) connections and the discharge resistor. Typically the power components are responsible for carrying high voltage and high currents. The power components all together transfer the DC voltage and current from the vehicle battery and output AC power in the form of three-phase AC currents and voltage for the motor that drives the vehicle. Each of the power components mentioned above has a critical role in achieving the power conversion and is highly interdependent on other components to ensure safe, reliable and desired operation of the inverter.

2.1.1 Semiconductor Power Switching Devices

Semiconductor power switching devices are solid state switching devices that help with power conversion from one form to another, i.e from AC to DC, DC to AC, AC to AC and DC to DC. Typically, a switching device has two states, on or off that can be controlled via a gating signal. A PCU converts power by rapidly switching a set of switches on and off in a specific sequence and for a specific time. The frequency at which the switches are turned on and off determines not only the waveform of the output voltage and current, but also dictates the losses and efficiency of the PCU. Historically, IGBTs have seen wide spread use in automotive traction inverters and converters due to its low cost, high temperature resistance and high efficiency.

However, as the demand for higher power density and efficiency has increased in recent years IGBTs are not able keep up due to the material limit of Si [1]. The discovery of WBG materials such as SiC and GaN and their implementation in developing MOSFETs has enabled PCUs to reach even higher power density and efficiency. This is because WBG switching devices offer higher breakdown voltage, higher current density, higher temperature resistance, higher thermal conductivity, faster switching speeds and lower turn on resistance. Comparatively, GaN devices do have an edge over SiC devices specially in low power (<10kW) and high switching frequency applications (>80kHz), currently SiC MOSFETs are an ideal choice for automotive traction inverters because they offer similar performance to GaN MOSFETs at higher voltages (800-1200 V), and higher power (>10kW) and come in various packing options readily available to choose from.

Table 2.1 shows comparison of SiC, GaN and Si IGBT for a automotive traction inverter.

Table 2.1: Comparison of key specifications of SiC, GaN and Si IGBT

Parameters	SiC MOSFETs	GaN MOSFETs	Si IGBT	source
Switching frequency (kHz)	100	140	20	[2]
Voltage breakdown (V/mm)	3×10^6	3×10^7	3.5×10^7	[3]
Thermal conductivity (W/m k)	370	130	150	[3]
Maximum operational temperature (°C)	175	150	175	-
Voltage rating (V)	High	Low	Highest	-
Current rating (A)	High	Low	High	-
Switching losses (W)	Low	Least	Highest	-

The switching devices come in two forms: power module packages and discrete devices. The module packages can be divided into two categories: half-bridge single-phase leg, and 3-phase power modules commonly refereed to as just power modules . The discrete devices can be further categorized into surface mounted switches and through hole mounted switches. The four types of the switching device packages are shown in Fig. 2.1. The use of either discrete devices or power module depends on the specific constraints of the design and targeted power density. The discrete devices provide tremendous flexibility in terms of component placement, inverter topology selection and scalability. However, one of the biggest challenges in using discrete devices for high power density is the limitation of the PCB design and it's ability to carry high currents.

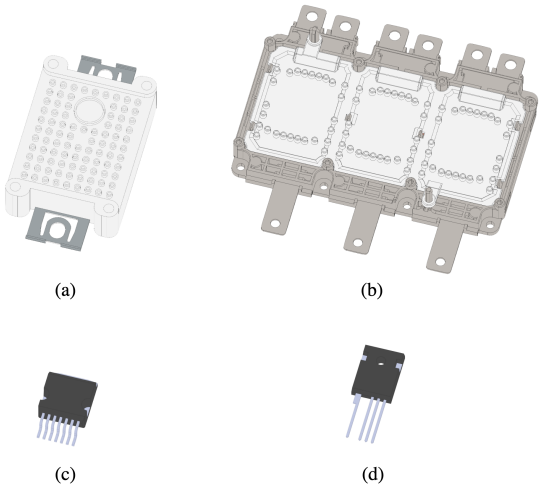

Figure 2.1: (a) Half-bridge power module, (b) 3-phase power module, (c) Surface mounted switch, (d) Through hole mounted switch

In order to mitigate these issues and utilize the best of both discrete devices and module packages manufactures such as Tesla and Audi have partnered with Original Equipment Manufacturers (OEMs) such as ST Microelectronics and Hitachi to create custom switching device packages shown in Fig. 2.2.

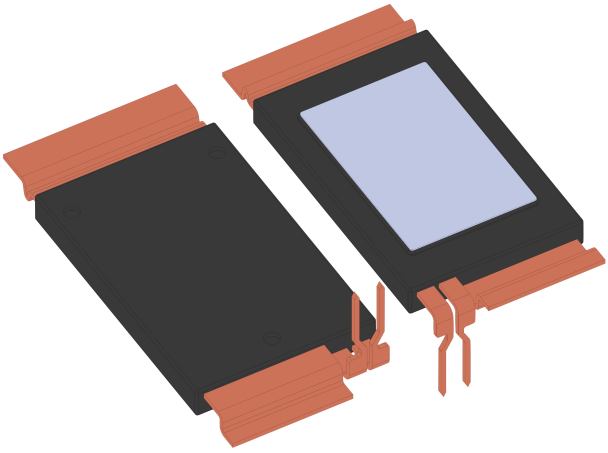

Figure 2.2: Custom SiC power module developed by ST Microelectronics for Tesla

2.1.2 DC-Link Capacitor

Dc-Link capacitor is the largest and bulkiest passive component in side a EV. It has three primary functions: absorb ripple current generated by the switching sequence, supply power difference between load and source during transients and help in filtering high frequency harmonics. There are three main capacitor technologies: electrolytic, film and ceramic capacitors.

Electrolytic capacitors have the highest energy density, however they can only operate at low switching frequencies and conduct limited ripple currents. In contrast, film capacitors can operate at high frequencies, high voltage, and can conduct large ripple currents provided the dielectric temperature is < 105 °C. Lastly, ceramic capacitors can conduct high ripple currents and handle higher temperatures, but the ceramic dielectric strength is highly dependent on temperature and the dielectric material is very rigid, therefore it can crack and break due to high vibrations and thermal stress. Additionally the dielectric strength breaks down at higher voltages, therefore more capacitors are needed in series or parallel to handle higher voltages [2]

In an EV inverter, the typical switching frequency is in the range of 25kHz [3] and therefore the use of electrolytic capacitors is not an option. Film capacitors are the most ideal choice and are commonly used in automotive industry due to their high reliability, safety, and the ability to handle high voltages despite often requiring active cooling to conduct high ripple currents. That being said, ceramic capacitors have the potential to replace film capacitors because of their higher temperature resistance and much higher energy density, provided the ceramic dielectric can handle high vibrations and thermal stresses.

The DC-link capacitors comes in either a discrete component or a bulk capacitor package as shown in Fig. 2.3 The bulk capacitor is nothing but a group of small capacitors arranged in series or parallel depending on its specifications and is encased in potting resin with integrated busbars. Bulk capacitor packages are most commonly used with power module packages, while discrete capacitors are often used with discrete switching devices and are mounted on a PCB. There are some discrete capacitors that can be used with power modules and separate busbars provided they can operate at higher voltage and current ratings.

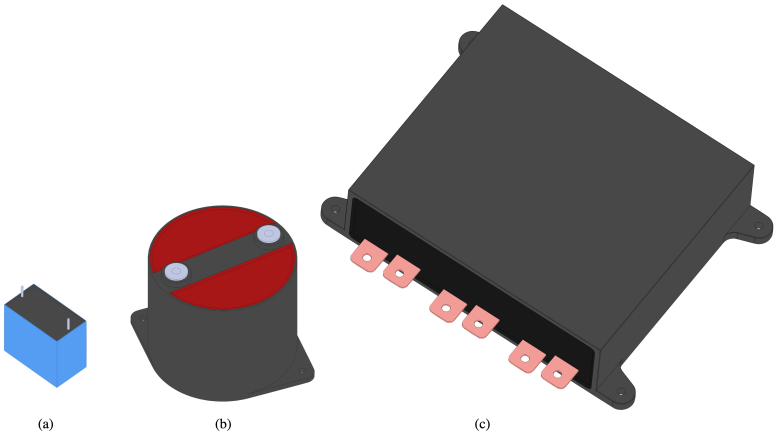

Figure 2.3: (a) Discrete capacitor PCB mounted, (b) Discrete capacitor with busbar connection, (c) Bulk capacitor for power modules

While selecting or designing capacitor specifications, it is important to ensure that the Eqivalent Series Resistance (ESR) and Equivalent Series Inductance (ESL) is minimized as much as possible, either by having short over lapping busbars or by minimizing PCB trace distances among other things [4]. This is because excess stray inductance can cause massive voltage overshoots and damage the switching devices and the capacitor itself.

2.1.3 HVDC and AC Connections

HVDC connection is the primary point through which the DC power from the battery is injected into the inverter. Therefore, it is important that the HVDC connection system provides safe, reliable and an easy way of connecting and disconnecting wires to the inverter, especially as the trend moves towards 800-1200 V architecture [5] Additionally, it also provides strain relief, Electromagnetic Interference (EMI) shielding, creepage and clearance insulation, along with environment protection. These features are critical because they protect the components of the inverter from vibrations, electrical noise and risk of short circuit due to water or dust ingress. Similarly, AC connection is the primary point through which three phase AC power is passed on to the motor. Just like an HVDC connection, the AC connection also needs to be safe and reliable, while providing the features mentioned above.

It is common for an EV inverter to have a receptacle for the HVDC connector harness, as it provides a reliable two step fool proof process to safely disconnect the inverter from the battery. Generally, the first step is to disengage the harness lock, followed by physically separating the two receptacles by pulling. An alternative to HVDC connector harness is cable cord grips, however they are not an ideal choice for automotive application because in the event of an emergency its challenging to disconnect a connection secured by a cord grip in a quick and safe manner. Additionally, unlike a HVDC harness that is keyed, it is difficult to ensure that the wires are connected with the right polarity.

2.1.4 Discharge Resistor

The discharge resistor or a bleeding resistor is a small passive component that is connected in parallel to the DC-link capacitor. It is used to dissipate stored energy in the DC-link capacitor when the inverter is turned off or in case of an emergency, for safety reasons. Additionally, It eliminates the possibility of a leftover charge in the capacitor so that the inverter is safe to handle for maintenance without causing electric shock. The main factor that governs the size of the resistor is the time it takes to discharge the capacitor, and for high power applications it may be necessary to provide some passive or active cooling to the discharge resistor so that it is not damaged.

2.2 Control Components

The control components are responsible for monitoring and controlling switching sequence, and frequency of the switching devices. The four main control components are: Control board, gate driver, current and voltage sensors and Communication I/O connectors. Each of these components aid and enable successful control of the switching sequence and frequency of the switching devices therefore they are considered as critical components and must have a high degree of reliability and redundancies built in to ensure safe operation.

2.2.1 Control Board and Modulation Schemes

The control board is used to implement control algorithms designed to govern the switching sequence and the frequency of switching devices. Two of the most common Pulse Width Modulation (PWM) control schemes are Sinusoidal Pulse Width Modulation (SPWM) and Space vector modulation (SVM).

SPWM is one of the easiest, most reliable and computationally inexpensive modulation scheme. However, traditional SPWM schemes has high Total Harmonic Distribution (THD) and the DC-link (V_{dc}) utilization is limited to $V_{dc}/2$. There are many multiple modified SPWM schemes that have improved performance [6], [7] and [8].

In contrast, SVM offers faster dynamic response, reduces THD, can readily utilize upto $V_{dc}/\sqrt{3}$ bus voltage and has multiple redundant switching states. One of the few drawbacks of SVM is it being complicated and computationally expensive. But the introduction of faster 32 bit microprocessors has helped bridge the gap and therefore, SVM is the preferred choice for real time digital implementation [6].

In addition to running and implementing control schemes, the control board is the desired location to receive external feedback from components such as the battery and motor. These feedback signals include but are not limited to: Battery voltage, Input current, motor position from resolver/encoder, current drawn by the motor and Controller Area Network (CAN) bus signals.

2.2.2 Gate Driver Board

The gate driver usually sits below the control board, takes input from the control board and amplifies it to control the switching sequence and frequency. In high power applications, the Gate driver board must be designed to drive sufficient current to utilize full switching speed of the switching device. A dedicated driver is used to apply the required voltage and provide the drive current to the gate of the power device. It is highly desirable to ensure that the driver circuit is as close as possible to the switches because this helps in reducing gate loop length and the associated parasitic inductances [9]

2.2.3 Current And voltage Sensors

Current sensors are a critical part of the control and feedback system because the decision made by modulation scheme is heavily dependent on the current that is being drawn from the load, as in the case of an EV-an electric motor. Therefore it is important to ensure that current sensor is located inside the inverter and can output current readings at extremely high frequency, with minimal noise and high accuracy.

Similarly, it is important to have a voltage sensor inside the inverter to read the input DC voltage form the battery. Just like knowing the current drawn by the load is critical, the exact voltage supplied by the source is important for the controller because it ensures proper voltage balancing of the capacitor and implementation of motor control.

2.2.4 Communication I/O

The communication (Input output)I/O is the primary point through which the inverter receives and sends signals to Electronic control Unit (ECU) and rest of the vehicle control systems. It is important for the I/O port to be dust, water and vibration resistant. Table. 2.2 lists necessary I/O signals along with their required channels and description. It is ideal to split the signals listed in 2.2 between two different connectors, where one of them carries all shielded signals and the other connector carries signals that don't need shielding.

Table 2.2: Number of I/O signals, channels and their description in a automotive inverter

Signal	Channels	Channel description
Resolver	6	Resolver excitation, Resolver excitation, resolver return sin + , sin -, cos +, cos - , shielded ground
Encoder	4	Encoder power, channel A channel B, Channel C
3-Phase motor current draw	4	Current U, current V current W, power
DC-Link voltage	1	Voltage +
2× CAN bus	3×2	Power, low signal high signal
Fault reporting	3	For any fault reporting
Temperature	6	Switching device $T_j(3)$, capacitor T_j (3)
Serial Peripheral Interface (SPI)	4	Serial clock, master slave in master slave out, slave select
Ignition Input	1	Motor start up sequence if needed
Start Input	1	Inverter start up sequence
Power supply	2	12 and 24 V
Redundant channels	6	For any user defined control channels
Ground	1	common ground for channels mentioned above
Shielded ground	1	shielded ground for any shielded channels
Total	46	Total of 46 channels for 13 signals

2.3 Cooling System

Cooling systems are arguably one of the most important inverter subsystems, there are numerous failure modes due to increase in junction temperature of the semiconductor switching devices [10], [11] [12] and [13], therefore it is important to design a reliable cooling system. In an effort to improve the heat transfer and reduce thermal resistance direct cooling has been implemented on several commercially available power module packages. However, this type of direct cooling is challenging to achieve on discrete devices because of their small foot print and it would violate existing packaging standards such as TO-247, T0-220, etc. Fig. 2.4 shows direct cooling and indirect cooling. The main difference between the two is that in direct cooling the internal layers of the switching device are directly soldered onto a heat sink, while in indirect cooling the internal layers are soldered to a copper base plate, which then needs to be mounted on a heat sink with an extra layer of Thermal Interface Material (TIM) in between.

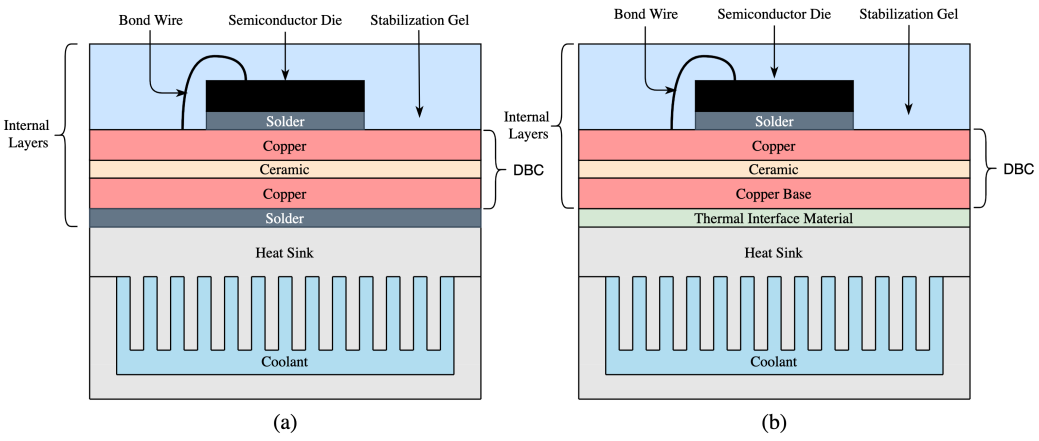

Figure 2.4: (a) Direct Cooling, (b) indirect cooling

2.3.1 Air Cooling

Air cooling is the most reliable and easy to implement cooling system mechanically speaking. It utilizes two out of three heat transfer mechanisms, convection and conduction. In convective heat transfer a material medium is required for the heat to transfer from the one place to another. But, the key difference between conduction and convection is that convection requires motion of the material medium. In the case of air cooling, the convection is possible because the air around the heat source is in motion.

Furthermore, air cooling can be classified into two more categories: Natural convection, and forced convection. Natural convection is when the fluid surrounding the heat sink is moving without any external driving force such a fan or a pump. The fluid motion occurs because warm air rises, and cold air sinks. Therefore, air surrounding the heat source heats up and rises, this creates a low pressure zone which is filled by cold air moving in from the surrounding to take place of the warm air. This cycle continues over and over again and in process cooling the component. Forced convection, is the opposite of natural convection and an external driver such as pump or fan is used to force the air around the heat source to move the air causing a cooling effect.

Air cooling can be realized in automotive applications and is demonstrated in may research papers [14], [15], [16] and [17]. But, either the volume of the inverter is too large, or the power density is low. The next section discusses water cooling and its advantages over air cooling.

2.3.2 Water Based Cooling

Water based cooling has been the norm in automotive industry, despite its complexity and reliability issues when compared to air cooling. With the trend moving towards higher and higher power density water based cooling is the clear choice for automotive applications, and with advancements in manufacturing, assembly and designing water cooling has never been more reliable and easy to implement. Just like air cooling water based cooling is a form of forced convective heat transfer. The reason why water based cooling is significantly better is because the Specific Heat Capacity (c_p) of water is 4200 J/kg.k vs 9.93 J/kg.k [18] this means that water is four times as good at storing heat than air, additionally the thermal Conductivity (k) of water is 0.58 w/m.k vs 0.024 w/m.k for air [18], meaning water can conduct heat twenty-four times better than air.

One of the few challenges when designing water based cooling systems is to ensure that the cooling system is easy to assemble and integrate into an inverter. The coolant loop must be leak proof, and be able to sustain pressure fluctuations due to change in coolant temperature (-20 ° C upto 75 ° C). It should have the lowest possible pressure drop, while utilizing minimal weight, materials, volume and provide effective thermal management. The design philosophy and tools to achieve these targets are discussed in detail in the next chapter.

Jet and Spray cooling

To tackle the high heat flux generated by high power electronics spray and jet cooling solutions have been designed and presented in numerous researches [19], [20], [21], [22], [23], [24] [25]. Fig. 2.5 shows spray and jet cooling for switching device packages.

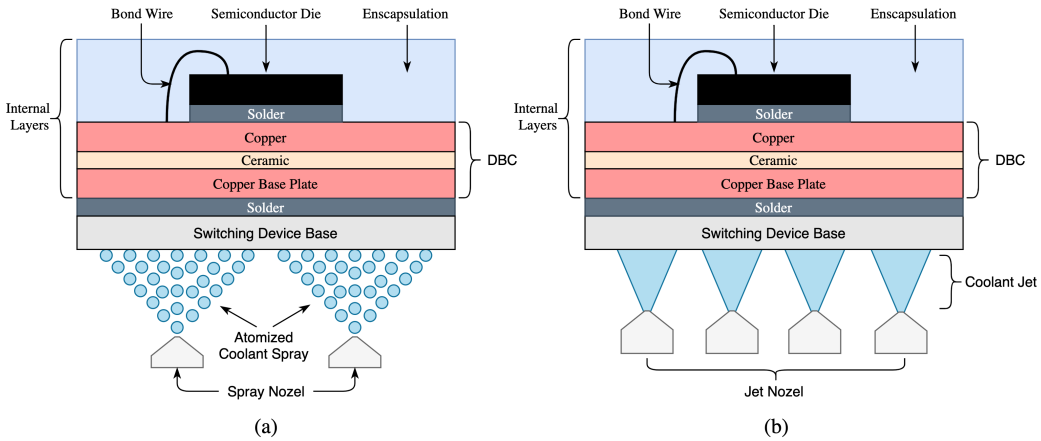

Figure 2.5: (a) Illustration of spray cooling, (b) Illustration of jet cooling

The goal behind spray cooling is to force coolant through a very small orifice causing it to split into multiple tiny droplets (atomization of coolant), and directing these droplets directly towards heat sources. The tiny droplets absorb heat from the source warm up condense and flow away from the heat source, and this cycle repeats as more coolant is pumped and atomized. This a form of multiphase cooling because the coolant changes it phase during the cooling process. The biggest advantage of spray cooling is its ability to maintain homogeneous temperature distribution among the switching devices.

Jet cooling is similar to spray cooling where the coolant is forced through a small orifice, but the key difference is that the coolant is not atomized, instead it exits the orifice as a fast moving turbulent fluid. The combination of turbulent and fast moving fluid increases heat transfer rate, and provide cooling to the heat source. Just like spray cooling, the biggest advantage of jet cooling is its ability to maintain homogeneous temperature distribution among the switching devices

However, Neither spray or jet cooling has been adopted in the automotive industry because of its high pressure drop, manufacturing challenges and reliability issues. The spray and jet nozzles are prone to clogging by rust or the small debris in the coolant loop, because the small nozzle diameter. Additionally, creating a single prototype of spray or jet cooling is relatively simple, however it is not scalable if thousands of parts need to be produced, most spray or jet cooling systems described in the literature rely solely on subtractive manufacturing, and cannot be made using more traditional manufacturing techniques like various forms of metal casting.

Lastly, the thermal performance improvement is not significant enough to justify the challenges associated with the high pressure drop of up to 145 kPa [19]. Specially considering that the cooling systems presented in the following chapter can provide equivalent thermal performance while having significantly less pressure drop.

2.4 Summary

Chapter two presents an overview of three main subsystems in an inverter: Power components, control components and the cooling system. Power Components section explains semiconductor switching technology and its packaging, DC-link capacitor technology and its packaging, the importance of HVDC connections, AC connections and the discharge resistor. Control components section presents the importance of control board and gate driver board design along with the need of having voltage, current feedback and communications I/O to monitor and control the inverter operations. Lastly, cooling system section presents two of the most common ways in which a automotive traction inverter is cooled; Air cooled and Water based cooling, with a brief explanation of challenges and advantages of each cooling method. Fig. 2.6 shows the inverter subsystems and how they work together

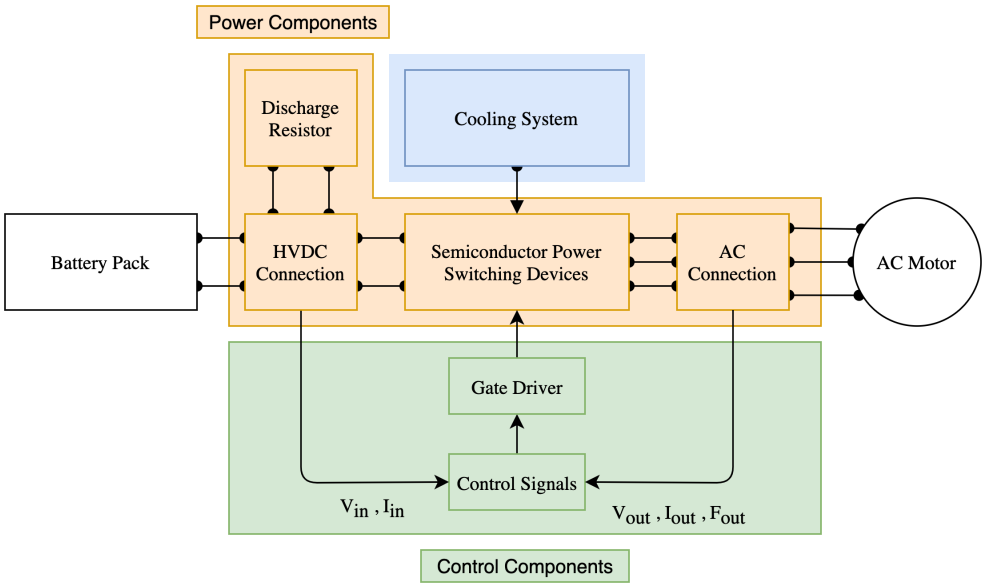

Figure 2.6: Block diagram of inverter subsystems and how they work together

Chapter 3

Thermal Management for a 120 kW Traction Inverter

3.1 Inverter Topology and Specification

The thermal management presented in this chapter is designed for a 120kW three level ANPC inverter and its switching devices. Due to the relatively lower power of the inverter, active cooling is not necessary for capacitors. The inverter presented in this thesis is designed for 800 V automotive traction application which leverages the higher voltage to boost efficiency. Fig. 3.1 shows the ANPC topology.

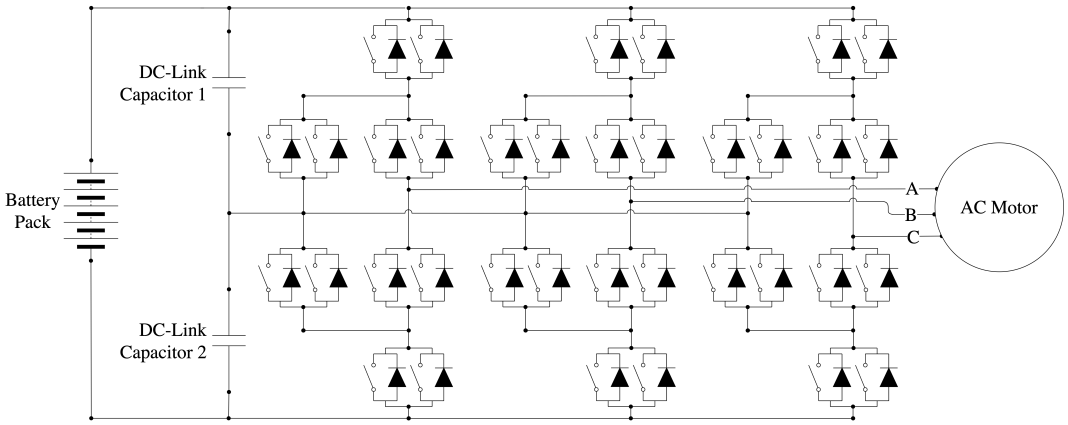

Figure 3.1: Topology of a three level ANPC inverter

Discrete SiC MOSFETs in a SO-247-4 package are used to create a three level ANPC topology. The layout and arrangement of the MOSFETs used to physically make the circuit is show in Fig. 3.2. The spacing between the MOSFETs is a function of the electrical and PCB design, therefore it cannot be reduced any further to save area.

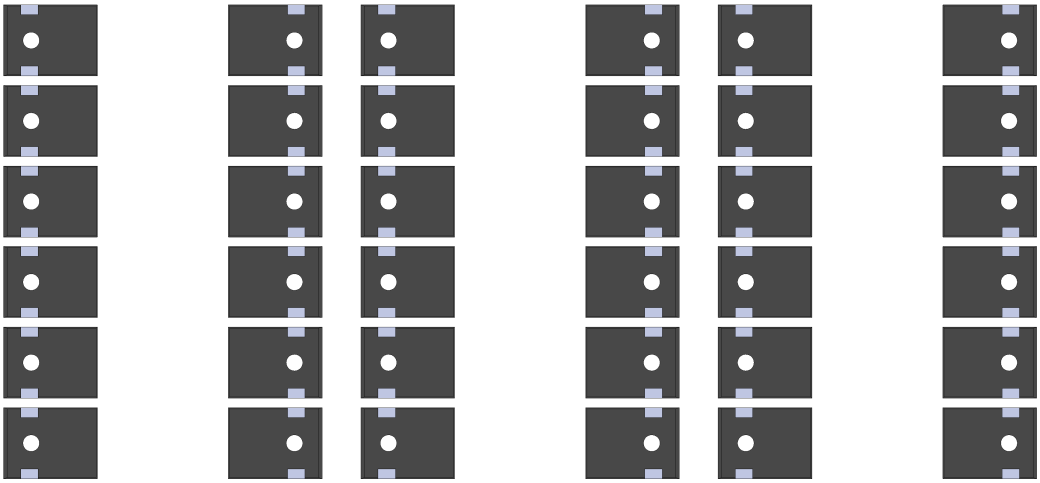

Figure 3.2: Layout and arrangement of the SiC MOSFETs in the 120kW ANPC inverter

As seen in Fig. 3.2 there are a total of thirty-six switches with each of them dissipating 60 watts of power adding up to a total of 2160 watts of loss for the entire inverter. The losses assumed for the thermal management design represent worst case scenario and lowest efficiency. One of the thermal design constraints is to limit the junction temperatures of the switching devices to 150 °C. This is 25 °C lower than the maximum allowable junction temperature of 175 °C listed in the data sheet [26] of the MOSFETs.

3.2 Cooling System Design Criteria

In general, a safe, reliable and efficient automotive traction cooling system should comply with the following criteria:

- Maintain low operational temperatures
- Ensure homogeneous cooling of switching devices
- Maintain low pressure drop
- Is easy to manufacture, assemble and is highly reliable
- Has a low volume and a lightweight design

The next sections explain in detail the importance and motivation behind setting these criteria. Three different types of thermal management solutions are provided for the specifications listed above with each design being an improvement over the former while increasingly satisfying all the design criteria listed.

3.2.1 Importance of Maintaining Low Operational Temperatures

In a typical traction inverter a cooling system is necessary for the switching devices. Additionally, the DC-link capacitor my also require cooling if it is conducting high ripple currents. Research has shown that the SiC can sustain operating temperature of up to 600 ° C [27] , [28], [29] But, the operation of SiC is generally limited to 175-200 ° C because operation at high temperatures comes at the expense of lower efficiency. The efficiency is impacted by an increase in conduction losses generated due to increased turn on resistance $R_{ds,on}$.

It also risks the possibility of thermal runaway because an increase in junction temperatures (T_j) causes more losses, effectively setting up a positive feedback loop. Furthermore, even if the SiC die can operate at such high temperatures, and the risks of thermal runaway can be navigated, other components inside the switching device package such as solder will melt if the temperatures are pushed past 350 ° C.

Another challenge in operating at extreme temperatures is possibility of critical failure as a result of thermo-mechanical stress. As shown in Fig 3.3 the internal layers of switching device packages are made of different materials that have different thickness. This difference in materials corresponds to a difference in coefficient of thermal expansion (α_l). Most materials experience a change in shape and size when it is subjected to a high change in temperature.

In an automotive application it is common for the temperatures to change significantly due to transient loads, this temperature delta combined with difference in α_l can cause layers to expand at different rates inducing stress on their neighbouring layers. The induced stress can cause the layers to peel, solder joints to break and wire bonds to crack [30], ultimately leading to a short circuit followed by critical failure.

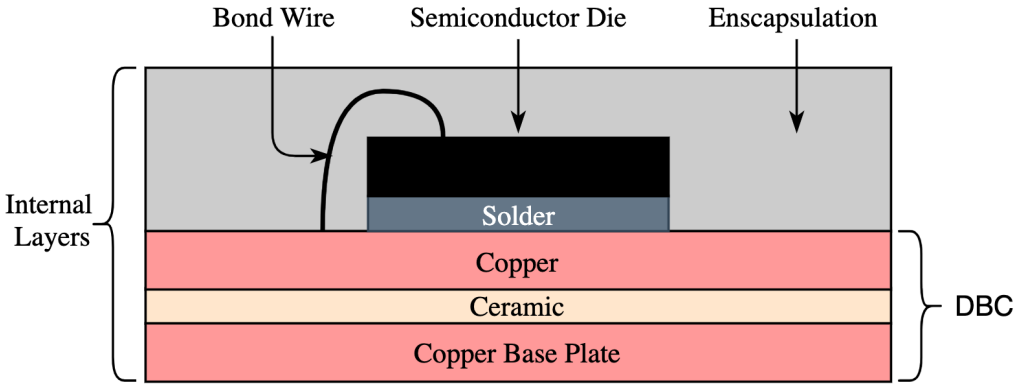

Figure 3.3: Layers inside a typical switching device package

3.2.2 Ensuring Homogeneous Cooling of Switching Devices

In a typical cooling system the coolant travels a long distance between the inlet and outlet. This means that the coolant heats up as it absorbs heat from the switching devices and therefore each subsequent switching device along the way receives warmer coolant. Fig. 3.4 shows how the coolant has to flow from left to right or vice-versa in a commercially available 3-phase power module package. This type of design may create an undesirable temperature gradient.

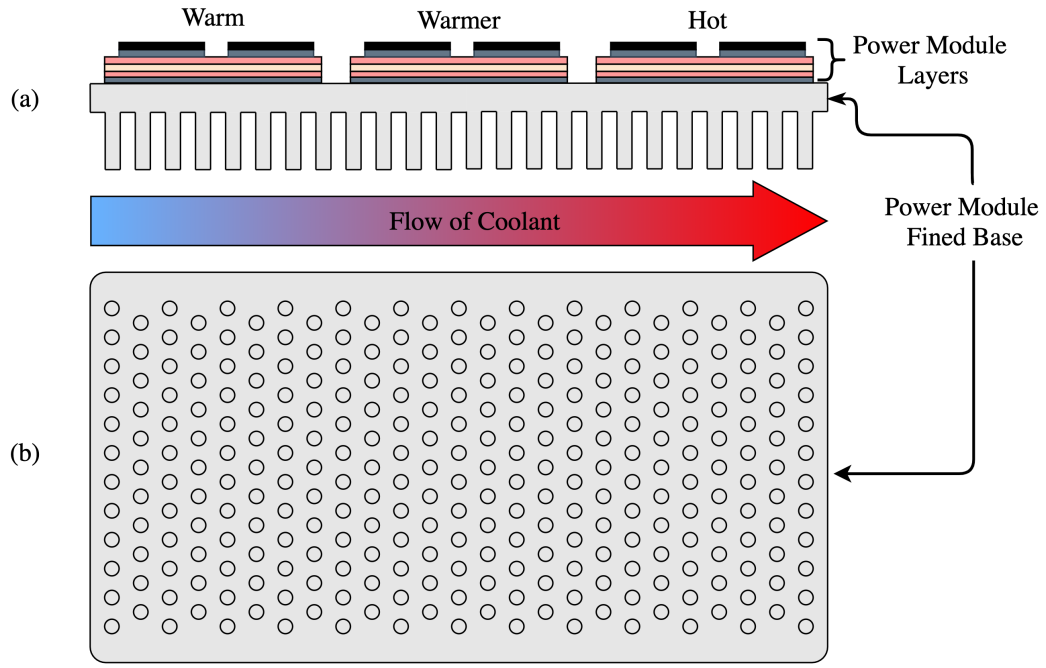

Figure 3.4: Power module pin fin base and the direction of coolant flow [31]: (a) Side view, (b) Bottom view

A temperature gradient in coolant temperature and switching devices in inevitable simply due to the physics of the fluid flow and heat transfer. However, the goal is to minimize the temperature gradient and homogenize the coolant temperature along the entire cooling surface. In this case minimize the temperature delta between left side switches and right side switches in Fig3.4 (a).

If the temperature deltas between the switches is too high it can create a reliability issue as warmer switching devices age faster and earlier [32]. This is specially undesirable for automotive application because the typical lifespan of a component must be at least ten years.

3.2.3 Maintaining Low Pressure Drop

Most EV have 3 coolant loops, one for the cabin temperature control, one for the battery thermal management and the last one for power electronics thermal management. Fig. 3.5 show a power electronics coolant loop. Cold coolant from the radiator gets pumped into the inverter first, followed by the DC-DC converter, On board battery charger, and lastly to the traction motor. The DC-DC converter revives coolant before the battery charger because if the car is on, the DC-DC converter is always working to provide auxiliary power to low voltage components, while the on board battery charger only generates heat when the rest of the car is turned off and the battery is charging. This arrangement also eliminates the use of a chiller and a heater to either cool or heat the coolant. This is because at any given point the coolant is never too cool for the inverter, and a fan on the radiator ensures that the coolant entering the inverter is not too hot.

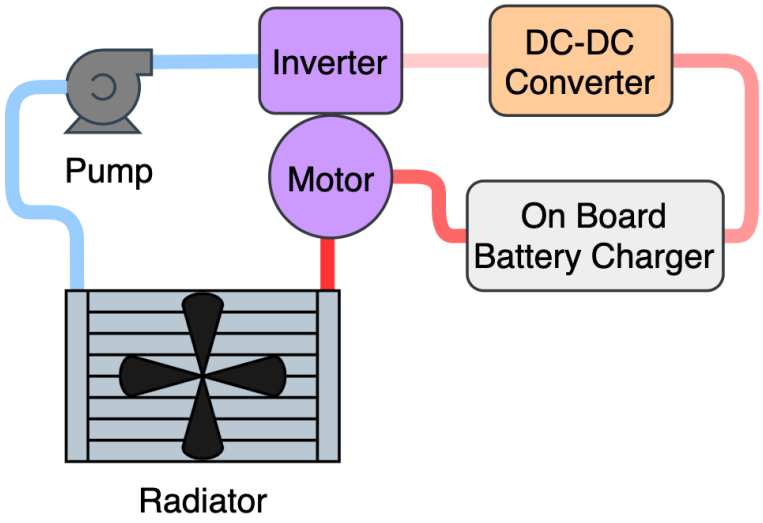

Figure 3.5: Coolant loop for power electronics component

The coolant provides effective cooling to the subsequent components after it passes through the inverter, thus it is necessary to minimize the pressure drop in each of the components including the inverter. Low pressure drop helps in reducing the strain on the pump, size of the pump and increases its life span, while eliminating the need for a second pump because a single pump can overcome the pressure drop of the entire coolant loop. This significantly reduces assembly complications, plumbing, cost, weight and auxiliary power draw, all of which are necessary to reduce in an automotive application.

In an effort to reduce the pressure drop even more and reduce the number of coolant loops, manufactures such as Tesla have completely eliminated the coolant loop for cabin temperature control, and coupled the battery coolant loop and power electronics coolant loop together [33].

Tesla uses the chiller and heater used to maintain precise coolant temperature of the battery loop to reuse and recycle heat to maintain cabin temperatures all the while reducing plumbing necessary for a third loop, reducing the number of pumps form three to two, and drawing less auxiliary power . One of the only few drawback of such an system is the added complexity due to increased number of flow valves and temperature control scheme, in addition to reduced reliably in providing adequate thermal management to the battery, power electronics and the cabin at the same time.

3.2.4 Ease of Manufacturing, Assembly and High Reliability

Manufacturing, assembly and component reliability is extremely important in the automotive industry. There are various possible solutions to challenging issues such as thermal management and pressure drop reduction, however these solutions do not consider the means of manufacturing as part of the design constraint. This results in great designs that work on paper, but cannot be utilized easily in a practical application.

Designs that can be manufactured using traditional manufacturing methods such as sand casting, die casting, injection moulding and in some cases subtractive manufacturing are always favoured over designs that require more exotic manufacturing processes such as additive manufacturing. Even if additive manufacturing is considered for a component intended for production vehicles, most Fused Deposition Modeling (FDM) plastic 3D-printers do not offer automotive grade materials and their structural reliability is questionable. Direct Metal Laser Sintering (DMLS) metal 3D printers can produce strong and reliable parts, that have seen special use cases in the aerospace and bio-medical industry but are unable to scale the rate of part production to automotive requirements.

That being said, additive manufacturing is invaluable in the early design stages as it helps a designer quickly prototype, test a component, and based on the results quickly iterate on the designs. This cuts the development time significantly, and yields more reliable components that have been tried and tested.

3.2.5 Low Volume and Lightweight design

One of the biggest challenges faced by electric vehicles is extremely high weight of the entire vehicle compared to gas powered vehicles. This impacts the range of the vehicle [34], [35] so great care focus must be put into ensuring that the vehicle is as light as possible.

Since the traction inverter is one of the most essential and largest component inside of an EV the Department of Energy (DOE) has set an aggressive target of achieving a power density of 100 kW/L by 2025. Simply improving the power density of the stitching devices will not help in achieving this aggressive target. Inside an inverter, in addition to the switching devices, the the DC-capacitor, the cooling also system occupies a significant amount of weight. Thus optimizing weight and volume of the cooling system is crucial.

Historically, most heat sinks and heat pipes in cooling systems were made from copper due to is superior thermal conductivity, however this came at an expense of the increased weight. A good alternate to copper is aluminum, it is 107 % lighter, but the thermal conductivity is about 79 % lower. Thus a hybrid approach is used where majority of the cooling system is made from a lighter material, and heat sinks are made from copper. For example, the power module packages both half bridge and full 3-phase packages have plastic body with copper base plates either with or without copper fins, similarly the MOSFET case is made from plastic or potting resin, but the base is made from copper. This thesis aims to replace copper heat sinks with aluminum heat sinks in the proposed designs in an effort to save even more weight without compromising thermal performance.

3.3 Fundamentals of Heat Transfer and Fluid Mechanics

3.3.1 Heat Transfer

Conduction Heat Transfer

In order to design an effective cooling solution, it is important to understand the underlying physics that governs the heat transfer. There are two modes of heat transfer that are responsible for cooling the SiC MOSFETs - conduction and convection. The heat generated by the SiC die inside the MOSFETs flows through the various layers underneath it until it reaches the boundary where the heat sink and the coolant are in physical contact. From there, the fluid motion around the boundary absorbs the heat and transports it out via convection.

Generally, the rate of heat transfer decreases when the thickness of the medium is increased, while the heat transfer rate increases when the area or temperature difference across the area through which heat is dissipated is increased. This evidence suggests that the that rate of heat transfer through conduction is proportional to the temperature difference across the medium, and the area perpendicular to the heat transfer, and is inversely proportional to the thickness of the medium. This can be represented by,

$$\text{Rate of heat conduction} \propto \frac{(\text{Area})(\text{Temperature Difference})}{\text{Thickness}}$$

or by equation 3.1

$$Q_{cond} = kA\frac{T_s - T_{amb}}{\Delta x} \tag{3.1}$$

where, the constant of proportionality k is the thermal conductivity of the medium and it represents the measure of a material to conduct heat. A is the perpendicular area through which heat is conducted. T_s is the temperature of the heat source and T_∞ is the temperature of the ambient air or the coolant, where $T_\infty > T_s$. Equation 3.1 can be rearranged to form equation 3.2 and it can be used both for conduction and convection, as long as the thermal resistance(R_{th}) is known. where Q_l represents the losses

$$Q_l = \frac{T_s - T_\infty}{R_{th}} \tag{3.2}$$

For most switching devices the areas and thickness of the internal layers are unknown, therefore representing it as a lumped value of R_{th} simplifies the equations and cooling system design process. Depending on the heat transfer mechanism, conduction or convection, R_{th} is defined by equation. 3.3 or equation 3.4 respectively. Where, h is the heat transfer coefficient and L is the thickness of the conducting material

$$R_{cond} = \frac{L}{kA} \tag{3.3}$$

$$R_{conv} = \frac{1}{hA} \tag{3.4}$$

It's important to note that the thermal resistance is not a constant value, because as the material heats up, it experiences thermal expansion changing its overall area. The thermal conductivity of a material is also a function of the material temperature, therefore its not a constant value [31]. However, for most practical applications and in this thesis the thermal resistance value corresponding to a specific k and h can be consider as a constant. Another important material property to consider is the thermal diffusivity, it represents how fast heat is diffused through a material and it is defined as

$$\alpha = \frac{k}{\rho c_p} \tag{3.5}$$

Where, density times specific heat capacity ($\rho\ c_p$) represents the measure of a material to store heat, therefore α is the ratio of heat conducted to heat stored per unit volume. This plays an important role in designing a heat sink because it is critical to reduce the value of α so that most of the heat is propagated through the layers, to the heat sink and finally into the coolant and not just getting stored into the layers and the heat sink.

Based on the equations above it is clear that, for a given ambient temperature and power loss the best way to reduce the heat source temperature is to reduce R_{th} and α. For conduction this can be achieved by maximizing the area and the thermal conductivity. For convection, the heat transfer coefficient (h) must be maximized in addition to the area (A). Reducing α is generally not practical since it is associated with material property, and there are only a handful of materials that are suitable for automotive applications.

Convection Heat Transfer

As Mentioned earlier conduction and convection are responsible for cooling the SiC MOSFETs. Convection is heavily dependent on the fluid motion, and it can occur due to buoyancy effects (natural convection) or due to forced fluid motion forced convection. Convection heat transfer is quite complicated because it involves fluid motion and heat conduction. The fluid motion improves heat transfer because colder fluid absorbs the heat from its surrounding and then moves away, and is replaced by new fluid. In fact faster the fluid flow, higher the heat transfer.

Convective heat transfer depends on fluid properties such as the dynamic viscosity (μ), thermal conductivity(k), density (ρ), specific heat capacity (c_p), fluid velocity (V). It also depends on the geometry and its surface roughness (Ra) and roughness (ε). Lastly, the type of fluid flow i.e laminar, transient or turbulent flow greatly influences convective heat transfer. Despite this complexity, convection rate of heat transfer can be represented by Newtons law of cooling and is shown in equation 3.6.

$$Q_{conv} = hA(T_s - T_\infty) \tag{3.6}$$

One of the biggest challenge of convective cooling system design is determining h, and as mentioned earlier it depends on many other factors.

In order to reduce the number of variables and simplify the equations, a lot of the variables are combined to form nondimensionalized numbers. One such important number is the Nusselt number and it is defined as,

$$Nu = \frac{hL_c}{k} \tag{3.7}$$

Where, L_c is the characteristic length. For simple geometries such a flow over a planar surface L_c is just the lenght of the surface. As the geometry gets complex, defining L_c becomes challenging. Nusselt number in general is the ratio of convective heat transfer to conductive heat transfer.

3.3.2 Fluid Mechanics

All fluids have an intrinsic property known as viscosity, and it represents how a fluid resists to a sudden change in its shape. As the coolant moves along the cooling system, viscous forces act on the fluid resisting its overall flow. However, depending on the initial conditions such as velocity, temperature and geometry the viscous forces can dominate the path of the fluid and subsequently the heat transfer. The viscosity of automotive coolant is low enough that the vicious forces do not dominate the flow, except in the boundary layers which will be discussed in the following sections, thus the overall flow is considered as inviscid. Similarly all fluids are compressible, however the forces required to naturally compress the coolant in a cooling system simply are not generated, therefore the flow is treated as incompressible. These assumptions greatly simply the analysis without sacrificing accuracy.

Velocity Boundary Layer

A overall fluid flow can be considered as multiple layers of fluid stacked on top of each other, the fluid layer closest to a solid boundary layer has zero velocity due to the friction between the solid and fluid. This layer of fluid slows down the layer of fluid above it because of the friction between them, the following layer is also slowed down relative to the layer below it so on and so forth until some distance δ . Beyond this point the velocity of the fluid is nearly same as the initial bulk velocity. This phenomenon is true for fluid flow over a planar surface, and not blunt objects such as cylinders. Fig. 3.6 shows the velocity boundary layer.

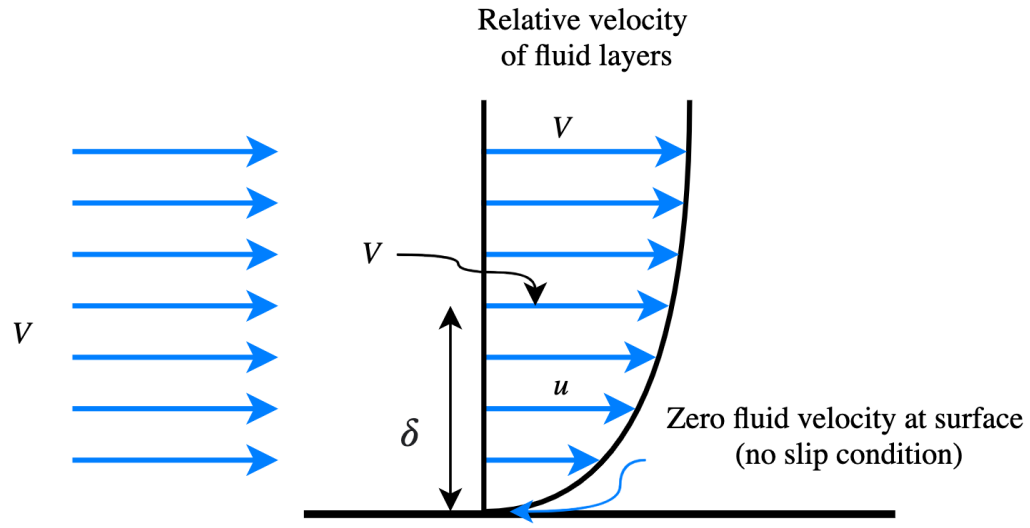

Figure 3.6: Velocity boundary layer due to no-slip condition and friction [36]

The region of fluid above δ has negligible frictional effects, while the layer below can be significantly impacted by changes in initial condition such as V, and subsequently influencing heat transfer.

Thermal Boundary Layer

Similar to the velocity boundary layer, when a fluid of specific temperature flows across solid with different temperature a temperature boundary layer is developed. Consider a fluid with uniform temperature moving across a planar surface with temperature. The fluid layer closest to the solid surface will have same temperature as the solid surface. The fluid layers then exchange energy with the layers above it, creating a temperature profile that reaches form T_s to T_∞ as shown in Fig. 3.7

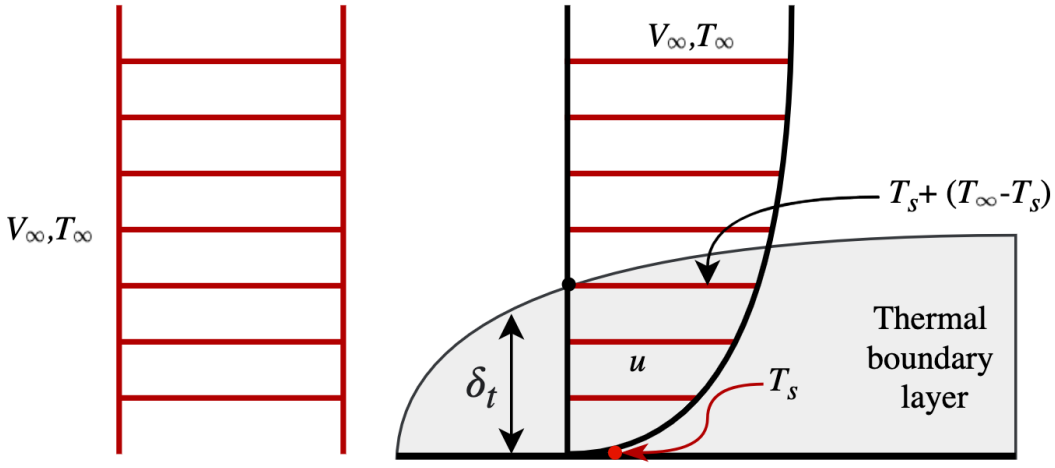

Figure 3.7: Thermal boundary layer where $T_s > T_\infty$ [36]

Based on 3.7 it can be noted that the heat transfer rate along the surface is related to the temperature gradient. The velocity of the incoming fluid has a significant impact on the shape of the temperature gradient. To avoid excessive press drop due to high velocities and maximize the heat transfer it is ideal to have $\delta = \delta_t$. This is almost impossible to achieve in practice because determining the thermal and velocity boundary is extremely challenging for complex geometry, let alone engineering a flow and geometry so that $\delta = \delta_t$.

Laminar Flow

Laminar flow is smooth and orderly motion of fluid particles relative each other. This type of flow is generally observed in fluids with high viscosity moving at low speeds, or by fluids with low viscosity but moving at specific speeds (usually high speeds) through a smooth channel. Because of the smooth and orderly flow, the pressure drop experienced due to laminar flow is the smallest, and therefore pipes and connectors used in automotive industry are designed to maintain laminar flow when the coolant is in transit form one component to another. Great care and effort is needed to maintain this laminar flow, typically most laminar flows will devolve to a turbulent flow over time and through the course of its path. It is ideal for the flow to start devolving into turbulent flow as it enters the inverter, and exits as a laminar flow or develops into a laminar flow.

Turbulent Flow

Turbulent flow is chaotic and the motion of fluid particles relative to each other is highly randomized. As mentioned earlier, most laminar flows devolve into turbulent flows, however this change is not sudden and it happens over time where the flow fluctuates between laminar and turbulent before becoming fully turbulent. This phase of fluctuations is known as transient flow. The random mixing of fluid in turbulent flow enhances rate of heat heat transfer between fluid molecules and the thermal boundary layer.

Therefore special considerations are made to insure that the flow is turbulent to enhance heat transfer, however this comes at an expense of high pressure drop because the frictional forces also increase as the fluid mixes randomly.

The type of flow regime mainly depends on the geometry, fluid velocity, surface roughness, temperature and the characteristics of the fluid. The influence of these parameters can can be captured by two main forces, inertial forces and viscous forces. The Reynolds number, which is a dimensionless quantity is the ratio of inertial forces to viscous forces and is represented by,

$$Re = \frac{V \rho L_c}{\mu} \tag{3.8}$$

Flows with Re number less than 2300 are considered as laminar, flows with $2300 > Re < 4000$ are transitional flows, and lastly flows with $Re > 4000$ are turbulent.

Another dimensionless number that is frequently used in thermal analysis is the Prandlt number Pr. It describes the ratio of the momentum of diffusivity to thermal diffusivity, as is given as

$$Pr = \frac{c_p \mu}{k} \tag{3.9}$$

The equations and fundamentals mentioned above will help in analytical analysis going forward.

3.4 Pipe Embedded Cold Plate

A pipe embedded cold plate is a viable thermal management solution for cooling discrete devices. A typical cold plate is composed of a block of aluminum with channels around regions of heat source where a circular copper pipe that is press fit into the channels. Fig. 3.8 shows an aluminum cold plate with copper pipe embedded into ideal number of channels. Each channel is directly below the MOSFETs so that the path of heat transfer from the MOSFETs to the coolant underneath is direct and as short as possible.

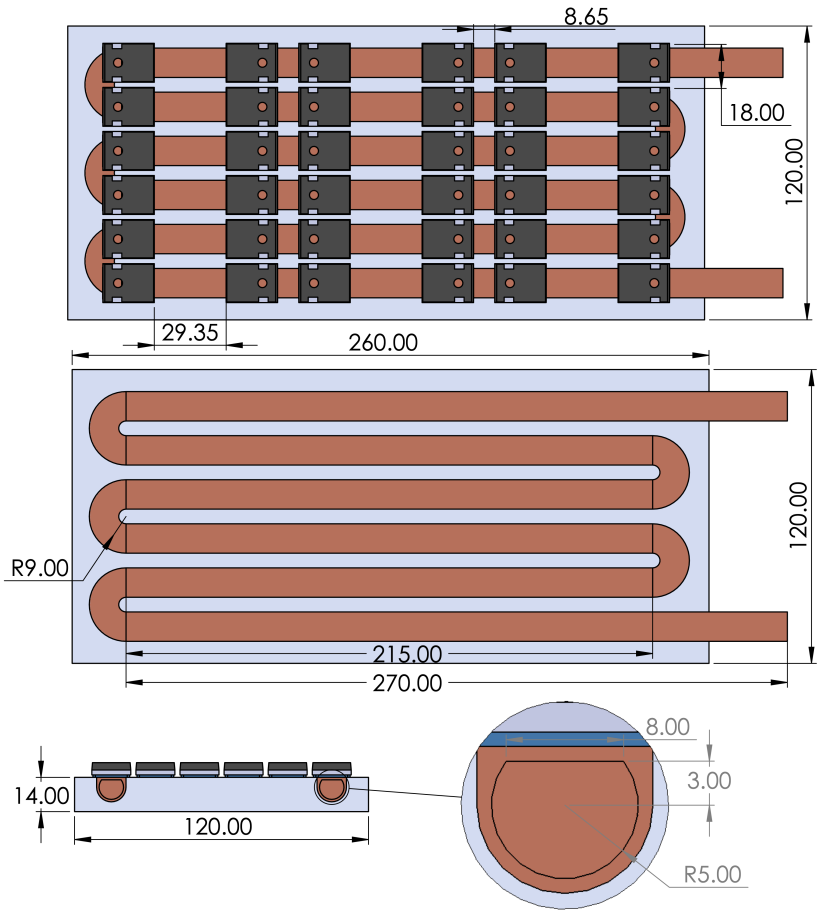

Figure 3.8: Ideal cold plate with wide copper channels underneath every MOSFET

However, this is challenging to achieve practically because the copper pipe cannot be bent with such tight radius. A general rule of thumb while bending pipe stock is to achieve a minimum bend radius of two times the outer diameter of the pipe.

$$r_{cp,min} = 2 \times D_{cp,od} \tag{3.10}$$

The copper channel layout in Fig. 3.8 uses a pipe with 12 mm Internal diameter and 14 mm outer diameter. Using equation 3.10 a pipe with outer diameter of 14 mm would require a bend radius of 28 mm, which is greater than the vertical distance (y_m) between two MOSFETs. To ensure that there is coolant flow underneath each MOSFET the copper pipe outer diameter can be reduced to 4.5 mm. This change would worsen the pressure drop and increase velocity. Since the width of the coolant channels is smaller and velocity is higher the combined effect will impact the thermal performance.

An alternate solution is to reduce the number of channels, but this would mean that the each MOSFET will not have a coolant channel underneath it. Each solution has its tradeoffs in terms of thermal performance and pressure drop. The temperature gradient cannot be calculated analytically because as the coolant moves past each MOSFET the coolant temperature increases, this increase in temperature will affect heat transfer of subsequent MOSFETs. Therefore, Ansys Fluent will be used to model the temperature gradient, but the pressure drop can be calculated analytically. The following sections will discuss the tradeoffs mentioned above quantitatively.

3.4.1 Pressure Drop Analysis

The pressure drop in the cold plate pipe channels can be modelled as pressure drop in pipe. There are two main forces that cause pressure drop; hydrostatic forces due to change in elevation and frictional forces due to friction between the solid and fluid, and between the fluid particles itself. Frictional losses(h_L) can be divided into minor losses and major losses as shown in equation 3.11. Major losses are a result of viscous forces on the boundary layer, while minor losses are due to every bend, valve and joint in the pipeline.

$$h_L = h_{Lminor} + h_{Lmajor} \tag{3.11}$$

Where, h_L is the total head loss, h_{Lminor} is the minor head loss and h_{Lmajor} is major head loss. Minor and major head loss can be calculated using the following formulas,

$$h_{Lminor} = \sum K_L \frac{V^2}{2g} \tag{3.12}$$

$$h_{Lmajor} = f_f \frac{lV^2}{D2g} \tag{3.13}$$

Where, K_L is loss coefficient, f_f is Darcy friction factor, l is the length of the pipe, D is the diameter of the pipe and g gravitational acceleration. $K_L$is are a function Re and geometry, while f_f is a function of Re and relative roughness which is defined by ε/D. where ε is the roughness of the pipe.

As seen above, the pressure drop is function of many parameters

$$\Delta P = F(V, D, \varepsilon, \mu, \rho, l) \tag{3.14}$$

The sheer number of variables that affect pressure drop make solving for pressure extremely challenging, especially if the geometry is complex. However, for simple geometry such as a pipe variables in equation 3.14 can be integrated into Bernoulli's energy equation 3.15 to determine pressure drop analytically.

$$P_{in} + \frac{1}{2}\rho {V_{in}}^2 + \rho g z_1 = P_{out} + \frac{1}{2}\rho {V_{out}}^2 + \rho g z_2 + \sum K_L \rho \frac{V^2}{2} + f_f \rho \frac{l V^2}{D2} \tag{3.15}$$

Where, P_{in} is the pressure at the inlet, P_{out} is the pressure at the outlet, z_1, z_2 represent change in elevation, V_{in} is the inlet velocity and V_{out} is the outlet velocity. Note that the last two terms in equation 3.15 represent the head losses(h_L). The expressions given in the stand alone equations(3.13 and 3.12) gives head losses in losses meters (m), while the expression integrated into 3.15 give head losses in Pascals Pa.

f_f can be determined using Moody chart shown in [36], originally made by Lewis F. Moody in [37]. K_L for 90 degree bends can also be found in [18] for 90 ° along with K_L for various other scenarios and shapes. Note that in cases where the pipe is bent to a "U" shape, minor losses for two 90 degree bends are added up.

Alternatively, equation 3.16, can be used to determine f_f, however this formula is an approximation of the the Moody chart, and was originally formulated by Haaland in [38]

$$f_f = \left(\frac{1}{-1.8log\left[\left(\frac{\varepsilon/D}{3.7} \right)^{1.11} + \frac{6.9}{Re} \right]} \right)^2 \tag{3.16}$$

For non-circular inlet and outlets, equation 3.17 is used to convert the non-circular profile to an equivalent diameter known as hydraulic diameter.

$$D_h = \frac{4A}{p} \tag{3.17}$$

Where, D_h is hydraulic diameter, A is the area of the inlet or outlet and p is the perimeter of the inlet or the outlet. The hydraulic diameter is used in place of normal diameter in any calculation that requires use of the inlet or the outlet diameter that is non-circular.

The velocity of the coolant at the inlet is determined using equation 3.18.

$$V = \frac{\dot{v}}{A} \tag{3.18}$$

Where, V is the velocity of the flow at the inlet, $\dot{v}$is the volume flow rate and A is the cross sectional area perpendicular to the flow at the inlet.

3.4.2 Cold Plate With Four Pipe Embedded Channels

Fig. 3.9 shows a cold plate with four pipe channels, it uses a pipe with 14 mm outer diameter and 12 mm internal diameter that is press fit into the cold plate.

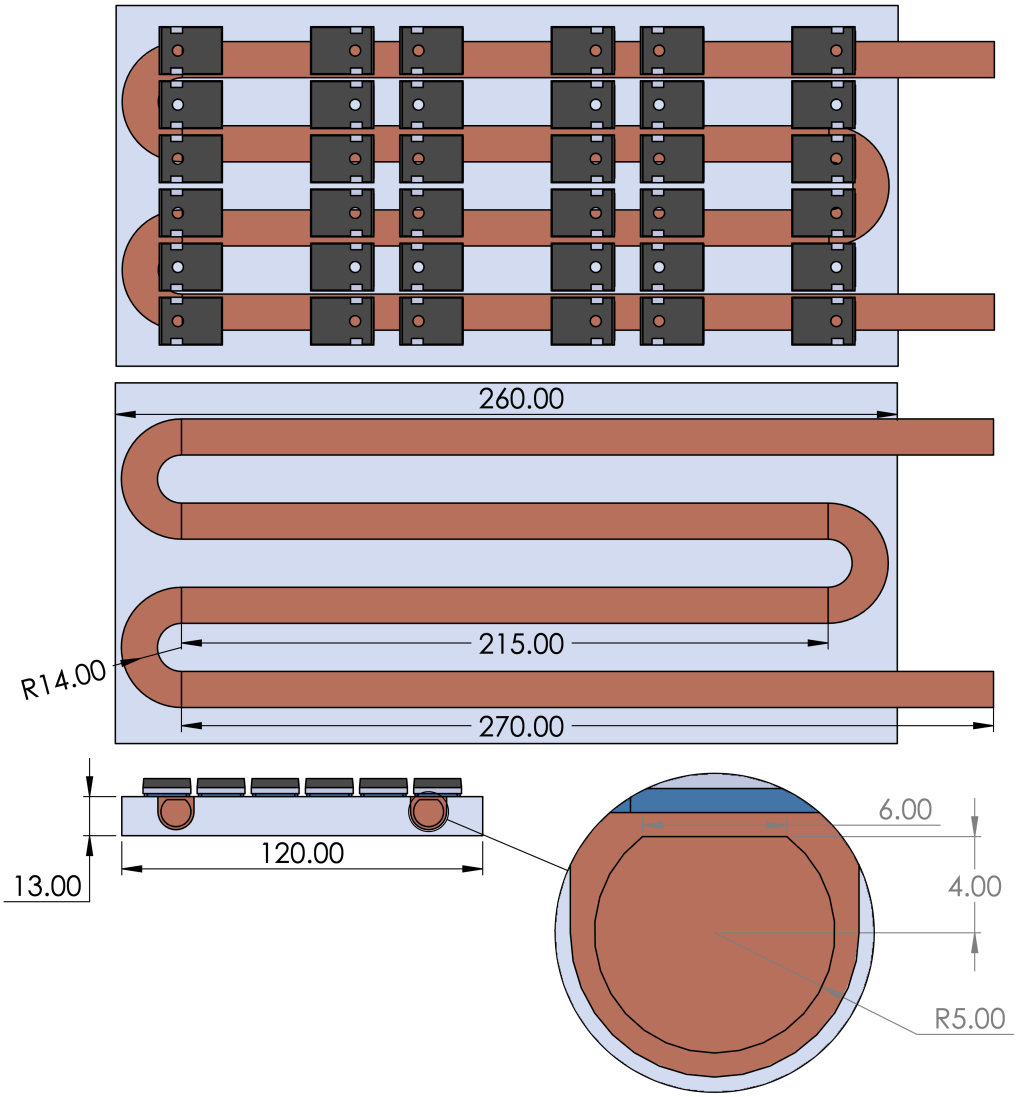

Figure 3.9: Cold plate with 4 channels for embedded copper pipe

In Fig. 3.9 the internal and outer diameters are deformed to a non-circular profile when the pipe is press fit into the channels, therefore equation 3.17 is used to determine equivalent diameter. Table 3.1 summarizes the parameter values that are used in equation 3.15 to compute the pressure drop in cold plate with 4 channels for embedded copper pipe.

Table 3.1: List of parameters and their values used in equation 3.15

Parameter	Value	Units
Glycol 50/50 density (ρ)	1031	kg/m^3
Glycol 50/50 dynamic viscosity (μ)	1.98×10^{-3}	kg/m s
Drawn copper pipe roughness (ε)	0.005	-
Copper pipe internal hydraulic diameter ($D_{cp,id}$)	0.0096	m
Copper pipe hydraulic area (A_{hd})	7.44×10^{-5}	m^2
Copper pipe hydraulic perimeter (p_{hd})	0.039	m
Copper pipe length l	0.970	m
Change in elevation ($z_1 - z_2$)	0	m
Change in velocity (V_{in}-V_{out})	0	m
Minor loss coefficient for 90 degree bend K_L	0.22	-
Darcy friction factor f_f	0.0286	-
Number of 90 ° bends	6	-

The pressure drop calculated analytically using equations 3.17 , 3.18, 3.8, 3.16 and 3.15 show the pressure drop to be 6751 Pascals(Pa). The inlet and outlet areas are the same, therefore, the inlet velocity is equal to the outlet velocity due to conservation of mass. Lastly, the change in elevation is also zero because the copper pipes are all on the same level, relative to each other.

Table 3.2: boundary conditions for CFD simulations

Boundary Condition	Value
Coolant type	Glycol 50/50
Coolant flowrate	8L/min
Coolant inlet temperature	65 °C
Ambient temperature of the MOSFETs	105 ° C
Total power dissipated by the MOSFETs	2160 Watts

Fig. 3.10 shows layering of components and their thermal resistances in a typical pipe embedded plate assembly. The losses generated in the MOSFETs are modelled as heat flux generated on the top surface of the TIM.

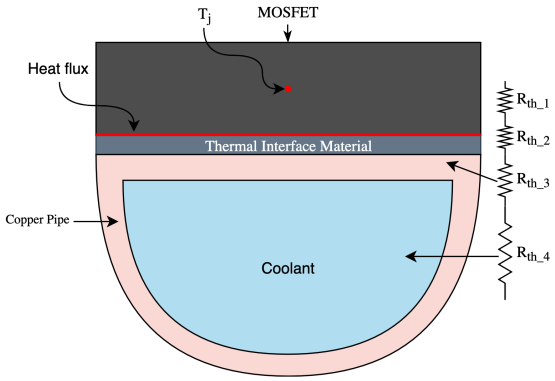

Figure 3.10: Layering of components and their thermal resistances in a typical cold plate assembly

R_{th_1} is the thermal resistances between the MOSFET junction and case, R_{th_2},R_{th_3} are the thermal resistances of the TIM [39] and the heat sink respectively. Lastly, R_{th_4} is the thermal resistance between the coolant and heat sink. R_{th_2}-R_{th_4} are determined by the CFD software based on the material and geometry, while R_{th_1} is found in the MOSFET data sheet [26].

Simulation Results: Cold Plate With Four Pipe Embedded Channels

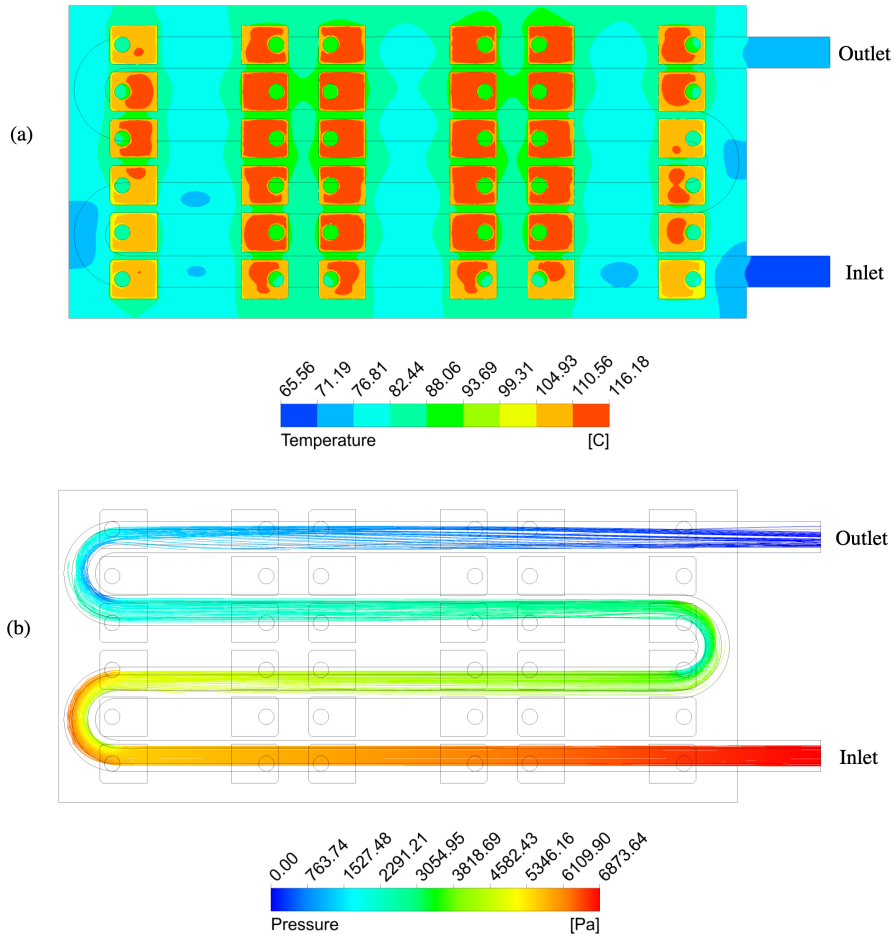

Figure 3.11: Simulation results of a 4 channel pipe embedded cold plate:(a) MOSFET case temperature gradients (b) Pressure drop in the

Shown in Fig. 3.11(b) the pressure drop value closely matches the analytical value of 6751 Pa. The temperature shown in 3.11 (a) is the case temperature of the MOSFETs. Using equation 3.3 and the R_{th_1} from the MOSFET data sheet [26] the maximum junction temperature is calculated to be 140 ° C.

3.4.3 Cold Plate With Six Pipe Embedded Channels

The temperature and pressure drop shown in Fig. 3.11 are reasonable, however as discussed earlier, another solution is to use smaller pipe so that the coolant flows under each MOSFET. Intuitively this configuration is expect to show better thermal performance because the heat generated in each MOSFET has a direct path to the coolant, while the pressure drop is significantly higher. Fig. 3.12 shows a cold plate with 6 channels with copper pipes

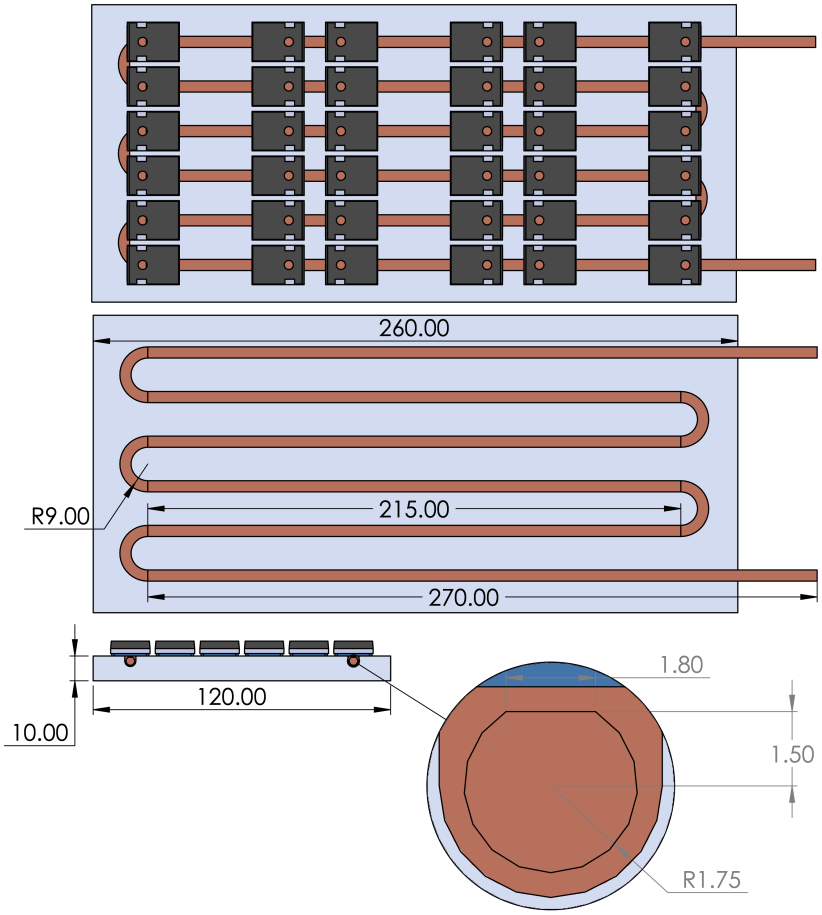

Figure 3.12: Cold plate with 6 narrow channels for embedded copper pipe

Simulation Results: Cold Plate With Six Pipe Embedded Channels

The pressure drop is calculated to be 1229 kPa and the overall maximum case temperature is reduced by approximately 12.5 ° C. This results in junction temperature of 126.5 ° C. Fig. 3.13 shows the simulation results of 3.12, and it can be seen that the analytical pressure drop matches simulated one closely.

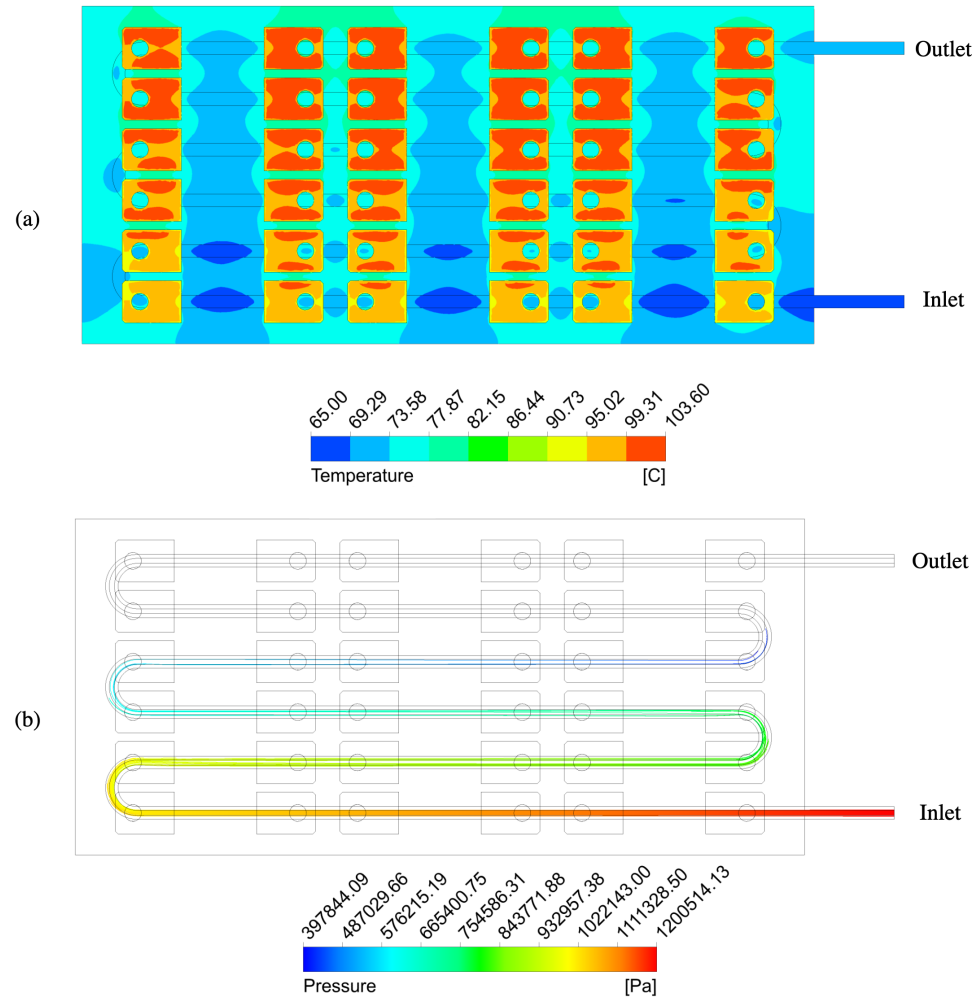

Figure 3.13: Simulation results of a 6 channel pipe embedded cold plate: (a)MOSFET case temperature gradients (b) Pressure drop

The 12.5 ° C difference in junction temperature is not worth the extreme pressure drop in designs shown in Figs. 3.9 and 3.12. Additionally, both designs have a temperature delta of 8 ° C and 11 ° C respectively, while the temperature deltas are not bad, there are other design approaches that can help minimize the temperature delta, reduce the pressure drop and junction temperatures.

Note that in both designs the MOSFETs closer to "U" bends have lower temperature, this is because the turbulence and velocity around the bends is higher, resulting in a higher rate of heat transfer. One way of eliminating this is by extending the length of the cold plate and copper pipe so that the MOSFETs are always underneath an un-bent section. This will result in a cold plate with marginal improvement in thermal performance at the expense of additional weight and volume.

The design shown in 3.12 can be improved by increasing the width of the copper pipe so that a larger area of the MOSFETs receive cooling. However, this is not possible due the manufacturing constraints. Both design are also challenging to integrate into an inverter housing because of the extending copper pipes beyond the cold plate. This prevents the cold plate to be inserted directly into the housing, additionally the non-circular diameters and extending copper pipes make it harder to securely connect a coolant hose. The next section shows designs that can avoid some of the short comings of the designs already shown.

3.5 Serpentine Cold Plate

A cold plate with coolant channels is a simplified version of pipe embedded cold plate. Instead of embedding a copper pipe in the channels, a flat pate is used to cover the channels in Fig. 3.14. This bypasses the challenging and constraining requirements of bending copper pipes. The thermal performance and pressure drop is not expected to improve significantly, but the manufacturing and assembly is greatly streamlined.

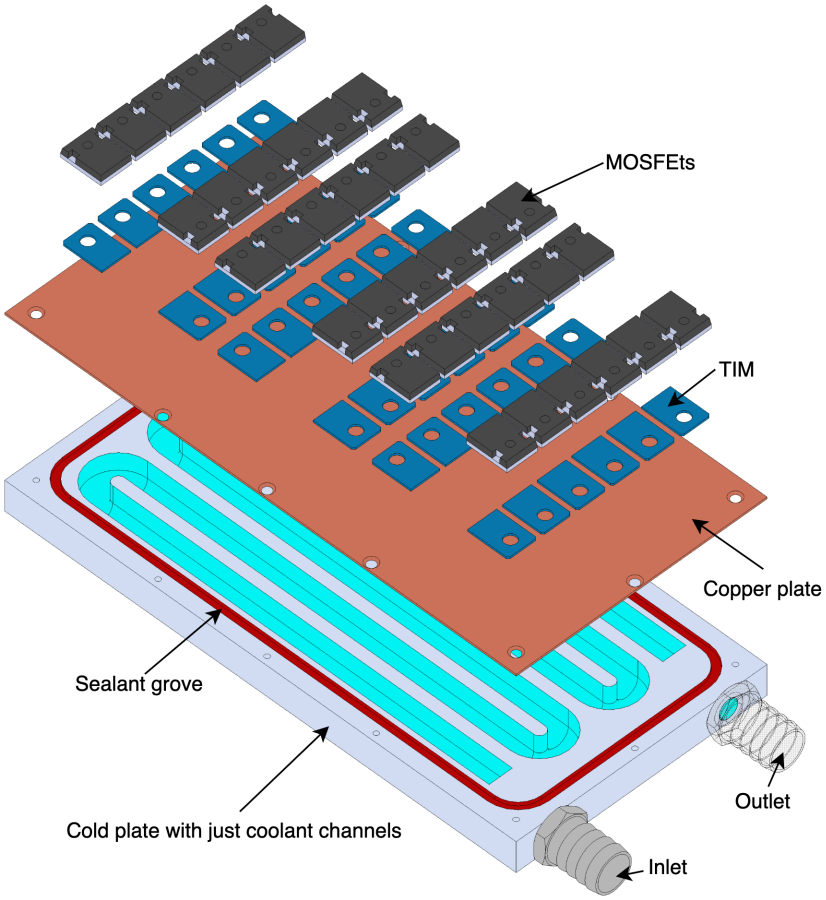

Figure 3.14: An isometric exploded view of a cold plate with serpentine coolant channels

3.5.1 Horizontal Serpentine Channels

Figure 3.15 shows a cold plate with six serpentine channels. The channels are arranged so that each MOSFET has coolant channel underneath it, since the machining and manufacturing of the channel is not limited by any constrictions the coolant channels have a tighter bend radius while having larger channels, this reduces pressure drop however the thermal performance is impacted.

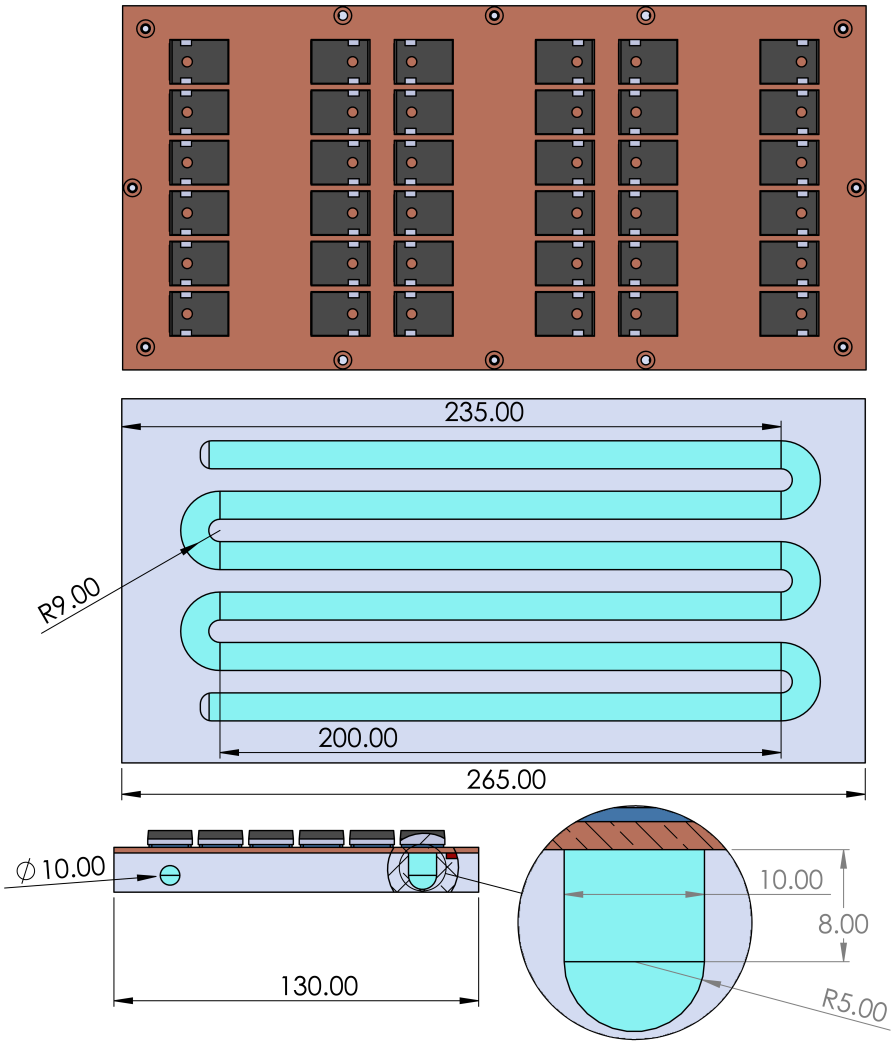

Figure 3.15: Cold plate with 6 serpentine channels in horizontal configuration

Simulation Results: Horizontal Serpentine Channels

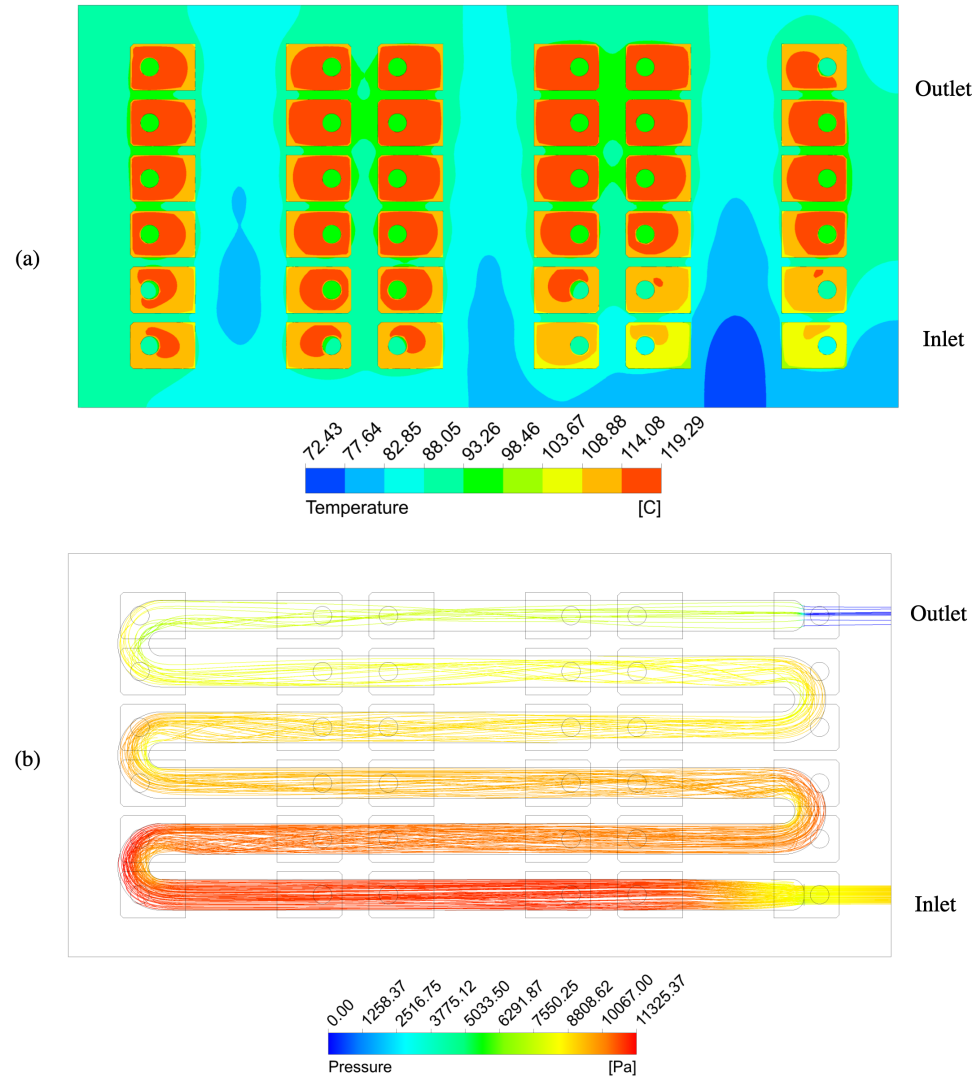

Figure 3.16: Simulation results of a cold plate with 6 horizontal channels:(a) MOSFET case temperature gradients (b) Pressure drop

As seen in Fig. 3.16(b) the pressure drop value is similar to the analytical value of 12080 Pa. The temperature shown in 3.17 (a) is the case temperature of the MOSFETs. Using equation 3.3 and the R_{th_1} from the MOSFET data sheet [26] the maximum junction temperature is calculated to be 142.7 °C.

3.5.2 Vertical Serpentine Channels

Figure 3.17 shows a vertical variation of the 6 channel serpentine coolant block. Just like the horizontal version the channels in vertical version are also directly underneath each MOSFETs. The width of the channel is increased by 2mm in order to decrease the pressure drop.

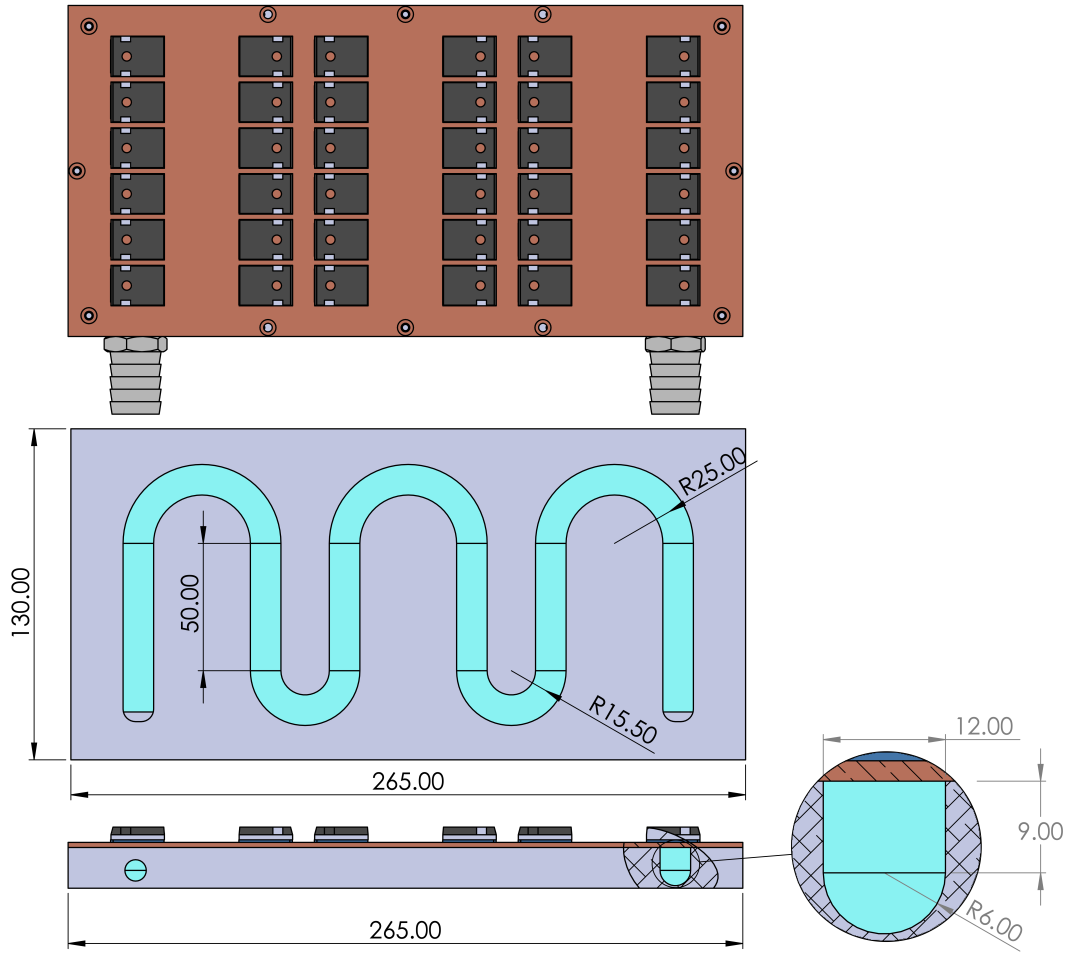

Figure 3.17: Cold plate with 6 serpentine channels in vertical configuration

Simulation Results:Horizontal Serpentine Channels

The analytcial value of the pressure drop is 5357 Pa and closely matches the simulated results shown in 3.18 (b). The maximum case temperature is 138 °C, this corresponds to a MOSFET junction temperature of 161.4 °C. Additionally the vertical configuration has the worst temperature distribution, however the maximum junction temperature is still 14 °C less than the maximum value in the data sheet [26].

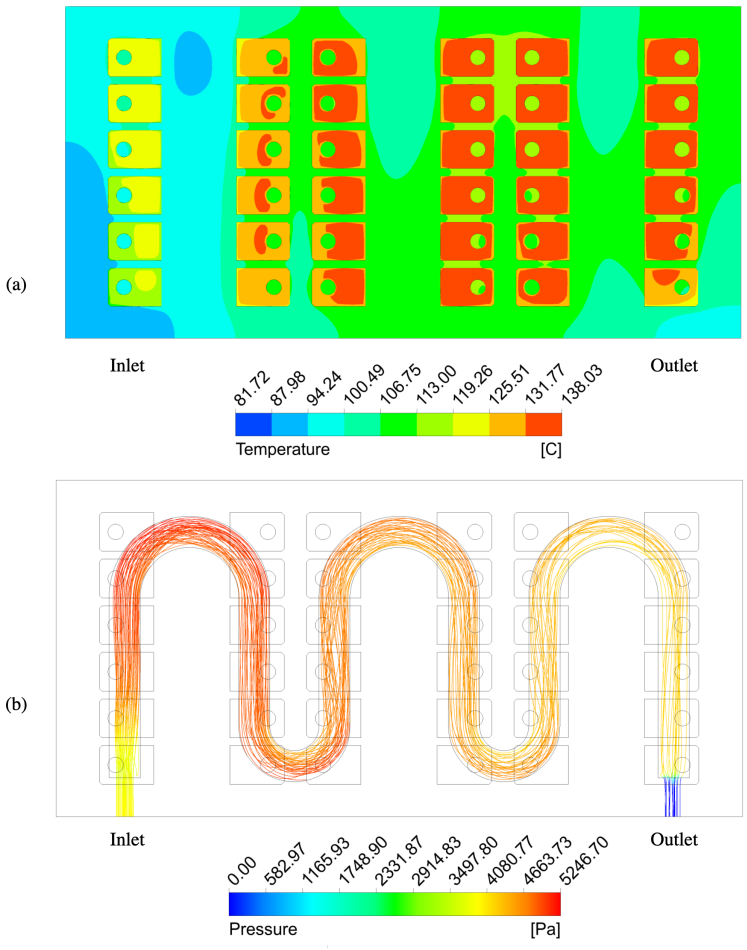

Figure 3.18: Simulation results of a serpentine channel cold plate with 6 vertical channels (a) MOSFET case temperature gradients (b) Pressure drop

3.6 Fined Base With Coolant Block

The cooling system designs discussed earlier have shown incremental changes in design so that manufacturing and assembly is easier. Despite, these changes the pressure drop in both pipe embedded cold plate and serpentine channel cold plate are high, while the thermal performance is acceptable. The goal of the fin based cooling system is to significantly improve upon the pressure drop while maintaining acceptable thermal performance. As discussed earlier and shown in the simulation results the rate of heat transfer is heavily dependent on the fluid velocity. However, the changes in velocity significantly impact pressure drop.

A fin base with coolant block aims to mitigate these issues by maintaining a low coolant velocity and increasing the surface area through which the heat is transferred. The design is split into two main parts; the design of the coolant block and the design of the fin base. The coolant block is responsible for providing a path for the coolant to flow through the fin base.

The design of the coolant block is crucial because it dictates the coolant distribution and entrance velocity. While, the fin base acts as a heat sink and provides a large surface area for heat transfer to occur when the coolant flows around the fins. However, the large surface area of the fins also blocks the coolant flow, this can reduce the rate of heat transfer and increase the pressure drop.

Finding an optimal design where the fin surface area, heat transfer and pressure drop are balanced is extremely challenging due to the number of interdependent variables involved. The following sections will discuss in detail how to achieve optimal designs for the coolant block and the fin base.

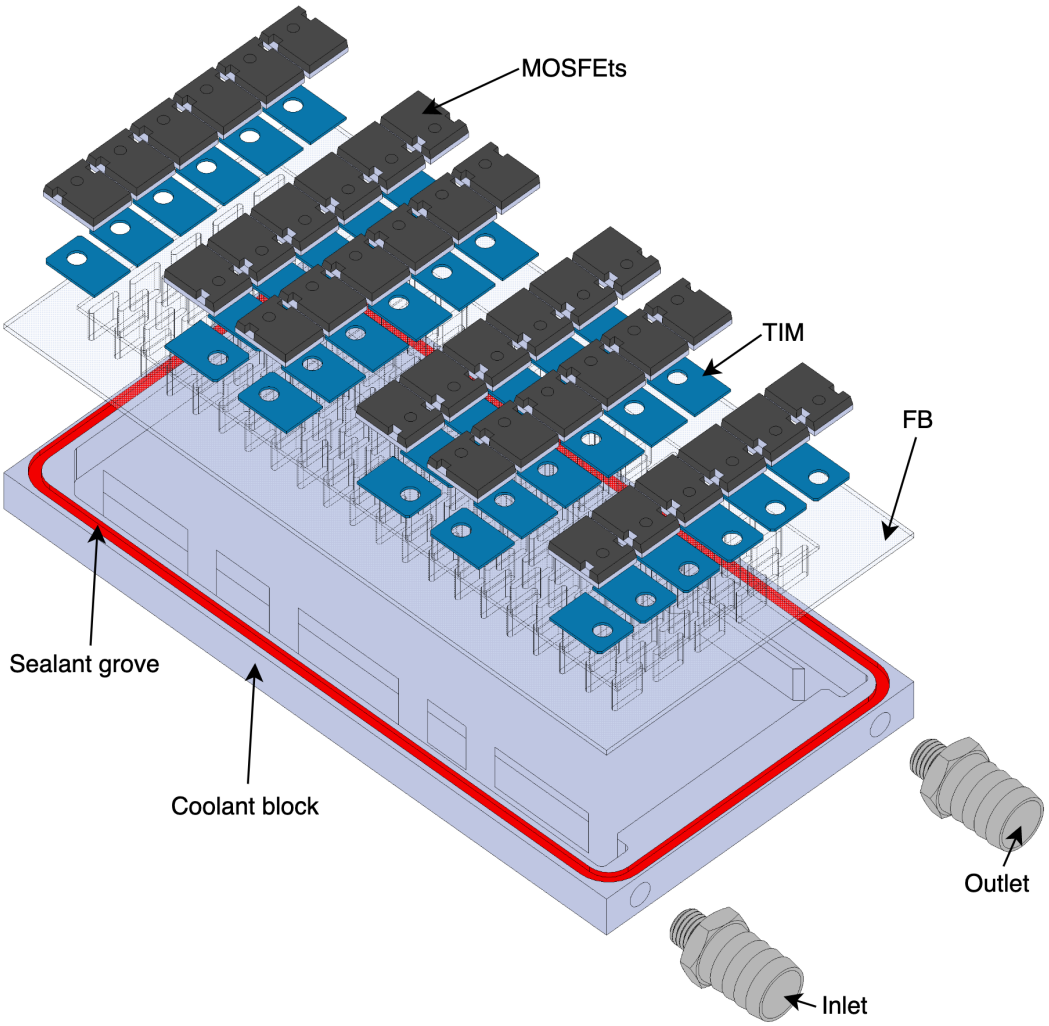

Figure 3.19: An isometric exploded view of a fin base with coolant block

Fig 3.19 shows an exploded view of an fin base with coolant block assembly. The fin base is shown in transparent view to visualize the fins.

3.6.1 Coolant Block Design

The coolant block has one location for the inlet and one location for the outlet. In order to ensure that coolant flows underneath each row of the MOSFETs the coolant block geometry is designed to split the flow where needed. Fig.3.20 shows the coolant block geometry and the number of sections it is split into. Sections 1 and 4 are smaller than sections 2 and 3, but sections 2 and 3 have two rows of MOSFETs while section 1 and 4 only has one row of MOSFETs.

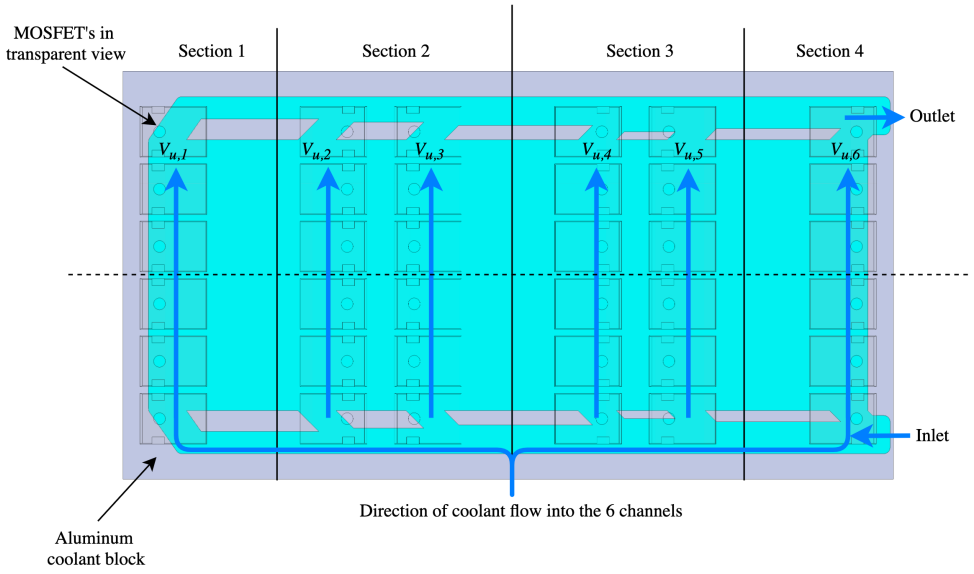

Figure 3.20: Coolant block design

The goal of the coolant block to ensure that $V_{u,1}$ and $V_{u,6}$ are same, while $V_{u,2}$-$V_{u,5}$ are the same. Intuitively $V_{u,1}$ and $V_{u,6}$ can have a lower velocity because the power dissipated is less in sections 1 and 4, however, at steady sate the cross coupling thermal effects can causes almost even distribution of the temperature on heat sink. Therefore the velocity at each section must be equal as shown in equation 3.19.

$$V_{u,1} = V_{u,6} = (V_{u,2} + V_{u,3}) = (V_{u,4} + V_{u,5}) \tag{3.19}$$

Intuitively when the coolant enters the inlet it has a forward momentum and inertia, thus, it does not easily divert to section 4. Similarly the moment and inertia of the coolant is damped at the end of section 1. This can result in uneven velocity distribution and thus uneven junction temperatures. To minimize this effect sharp angles are used to shear part of the flow to split into channels 1 to 4. In channel 5 the cross sectional area is reduced to increase the velocity of the coolant locally to counter the damping from the bend.

Creating an analytical model that accounts for the inertial physics of the flow is challenging without some experimental correlations. To tackle this problem and still generate a design that has uniform velocity a parametric sweeping approach is used in modeling and simulating the velocity at each channel. Fig.3.21 shows the final geometry of the split coolant flow. Parameters x_1 to x_5 are varied in increments of 1mm from an initial value of 12mm to generate geometries of various combinations such that equation 3.19 is satisfied.

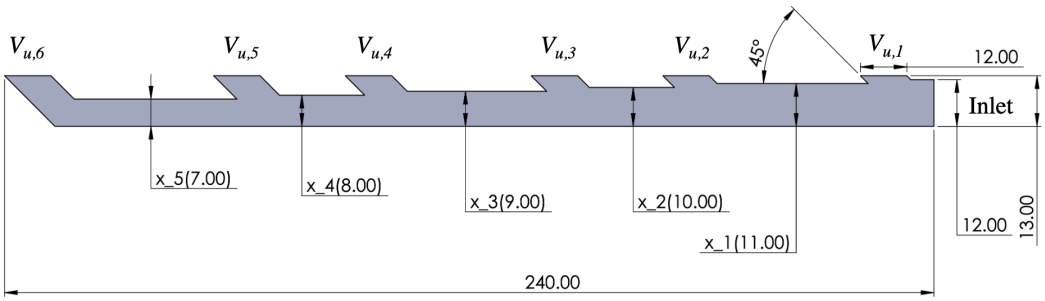

Figure 3.21: Coolant block channel geometry and its design parameters

These geometries are simulated in Ansys fluent and Fig.3.22 shows the simulation results of the coolant velocity distribution in final geometry. The same geometry is mirrored on the opposite side for the outlet channels. This makes the machining and manufacturing process straight forward while providing the flexibility to interchange the inlet and outlets since they are symmetric.

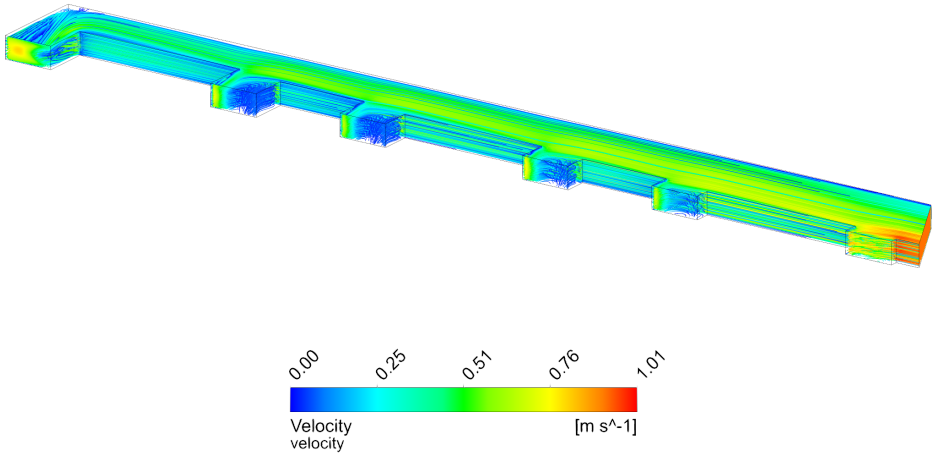

Figure 3.22: Coolant velocity streamline of final coolant block geometry that splits the flow into different channels

The coolant is distributed in parallel because the distance the fluid travels across the finned geometry is only 100 mm, as compared to 240 mm of finned geometry if the coolant was distributed perpendicularly. The parallel distribution first and foremost reduces pressure drop, secondly it offers more design control to ensure that each section has a uniform flow velocity and subsequently uniform cooling. Additional benefit of having parallel channels is that the inlet and outlet ports are on the same side of the geometry, simplifying the coolant loop and making integration of cooling system into the housing easier.

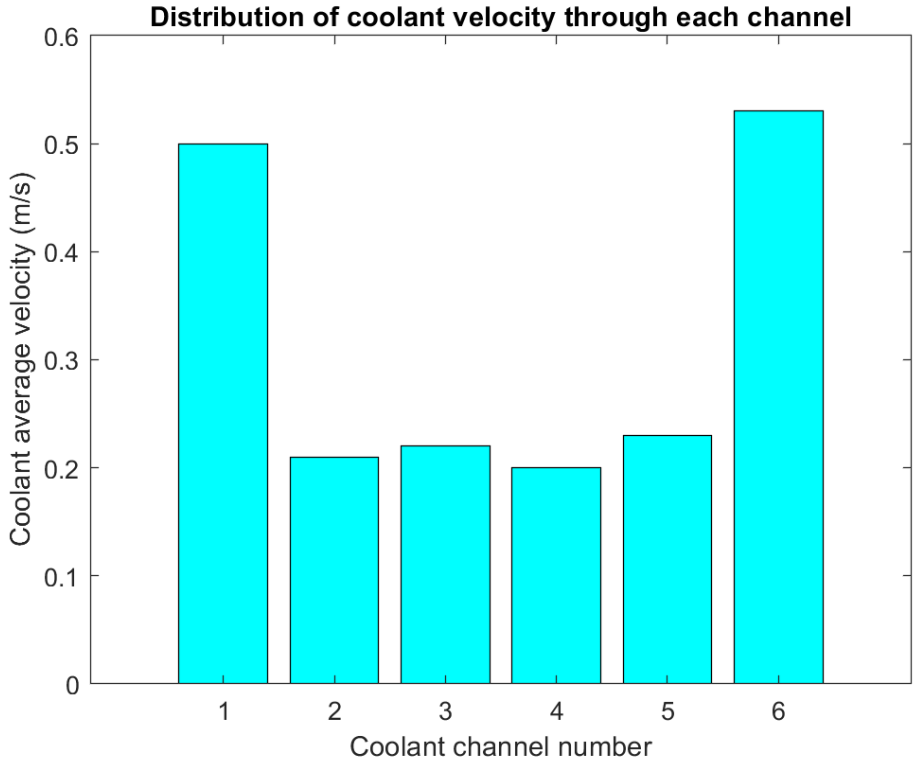

Figure 3.23: The average velocity $V_{u,n}$ at each channel

Fig. 3.23 shows a graph that plots the average velocity at each channel. As seen in 3.23 the average velocity is mostly equal in channels 2-5, similarly the coolant velocity is fairly equal in channels 1 and 6. This results in an average velocity of 0.47 m/s in each section, while the individual values are not exactly the same, they are close enough to be used for analytical analysis. Note that the pressure drop analysis is not performed on just the channels because without the fins the analysis does not represent a realistic scenario. However, the simulated entrance velocity is going to remain the same regardless of the presence of finned the geometry.

3.6.2 Fined Base Design and Optimization

The primary mode of heat transfer from the fins to coolant is through convection. This governed by equation 3.6 shown below.

$$Q_{conv} = hA(T_s - T_\infty)$$

It is clear that in order to maximize the power dissipated, Area(A) and heat transfer coefficient(h) must be maximized. The previous section focuses on designing a coolant block such that the velocity approaching the fins is uniform for all the fins as much as possible. This ensures that the h approaching the fins is equal. Once the fluid is distributed throughout the fins, the value of h will change locally. Additionally, the value of h will be dependent on the geometry of the fin. However, increasing A and h unconstrained starts giving diminishing returns. Equation 3.20 shows the basic principle behind the heat transfer through the fins.

$$Q_{cond} = Q_{conv} \tag{3.20}$$

where the heat generated by the MOSFETs passes through the base of the heat sink and the fins through conduction and then the heat transfer from the fins to the coolant happens via convection. There are various fin geometries such as tear drop fins, elliptical fins, triangular fins, annular fins, cone fins, circular fins, and rectangular fins. Each geometry has its pros and cons. For the purpose of this design, rectangular fins are considered because the offer low pressure drop while having acceptable thermal performance.

Rectangular Staggered Fins

Rectangular fins are an ideal choice for a heat sink design specially with parallel flowing coolant channels because it helps in reducing pressure drop significantly. Depending on the aspect ratio of the rectangular fin, i.e. ratio of the length to width, the approaching flow does not separate around the fin. This reduces turbulence and wake region, thus, reducing the pressure drop. The thermal performance is impacted, however a relatively long fin provides enough surface area for heat transfer despite low turbulence.

Additionally, a staggered fin arrangement is utilized because it is better for heat transfer than a in-line fin arrangement, specially for rectangular fins because the staggered arrangement has superior thermal performance irrespective of fin geometry due to higher surface area, while having minimal impact on the pressure drop. Proper design, arrangement and spacing of these fins can have a significant impact on the temperature distribution and the pressure drop. Equations and analysis below discuss in detail how to optimize fin parameters.

On the other hand, most of the other fin geometries mentioned above are designed and naturally shaped so that the approaching flow is separate into a turbulent wake or form periodic vortexes. Both are highly desirable for heat transfer because it results in more mixing and moving of the fluid, enhancing heat transfer. However, this comes at the expense of separated flow which increases drag, and ultimately increases pressure drop. Similar conclusions were drawn by [40], [41], [42] when investigating different fin geometries.

Fin Modeling Using Entropy Generation Minimization

Entropy is the energy that is unavailable to do work. In a heat sink design this entropy is generated due to the flow of coolant and viscous effects along with the temperature gradient caused by the heat transfer. Since the entropy generated cannot be reversed it results in a system that is unable to use all of its energy to do the"needed" work, in this case cooling the MOSFETs. In general, there exists an optimal design of a heat sink where the rate of heat transfer and pressure drop are balanced so that the total entropy generated is minimized [43]. In order to achieve these optimization goals the heat sink design relies on some basic assumptions listed below.

- Steady state
- Uniform approach velocity V_u
- Incompressible fluid flow
- Heat flux generated uniformly over the fin base top
- No bypassing flow.

As shown in section 3.6.1, the coolant block channels are placed such that the coolant path is directly underneath the MOSFETs. The channels are designed to provide equal velocity, therefore, the total heat sink analysis can be divided into four sections, and the entrance velocity (V_u) is the same for each section. Once one section is optimized, the same design variables can be used for other sections since even the heat flux is uniformly spread. This method greatly simplifies the analysis without sacrificing much accuracy.

Equation 3.21 shows the entropy generation rate by applying laws of conservation of mass and energy with the entropy balance for a fluid flowing across a heat sink [44].

$$\dot{S}_{gen} = \left(\frac{Q_l}{T_{amb}}\right)^2 R_{RFB} + \frac{\dot{m}\Delta P}{\rho T_{amb}} \tag{3.21}$$

Where Q_l is the loss generated by the MOSFETs T_{amb} is the ambient temperature, $\dot{m}$ is the mass flow rate across the heat sink, ΔP is the pressure drop and R_{RFB} is the thermal resistance of the entire finned base.

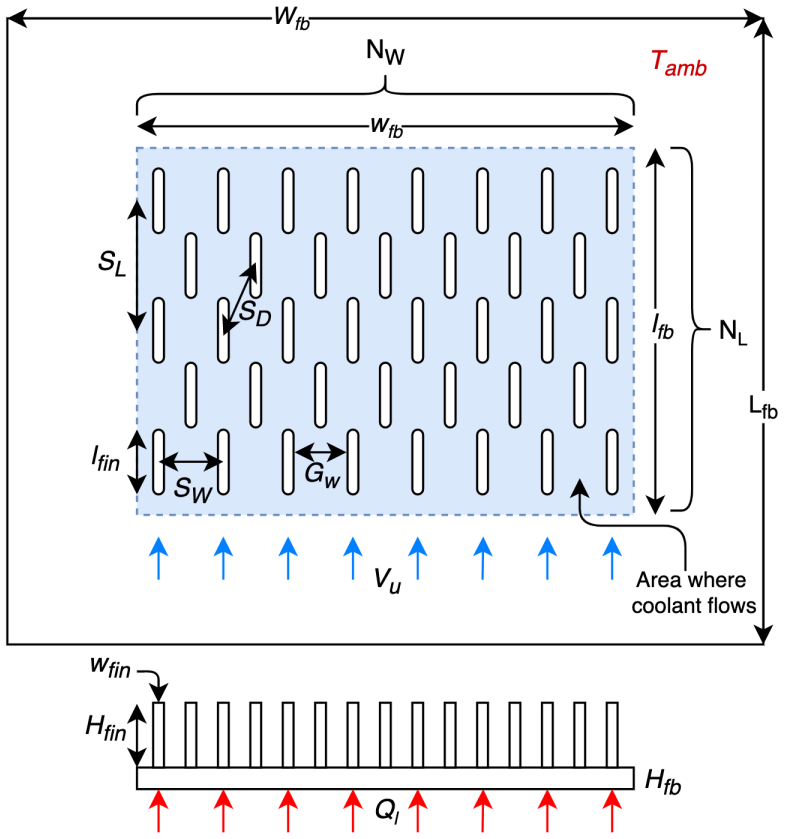

Figure 3.24: A quarter section of heat the sink widthwise W_{fb} along with the fin layout and necessary parameters used in the analysis

$$R_{RFB} = R_{fb} + R_{fins} \tag{3.22}$$

R_{fb} is the thermal resistance of the fin base and R_{fins} is the thermal resistance of the fins.

$$R_{fb} = \frac{H_{fb}}{k_{RFB} A_{fb} W_{fb} L_{fb}} \tag{3.23}$$

H_{fb} is the height of the fin base and k is the thermal conductivity of the heat sink material.

$$R_{fins} = \frac{1}{h_{fin} SA_{RF} N_{fins}} \tag{3.24}$$

$$\eta_{fin} = \frac{tanh(mL_c)}{mL_c} \tag{3.25}$$

$$SA_{RF} = 2(l_{fin} H_{fin}) + w_{fin} l_{fin} + 2\pi w_{fin} H_{fin} + \frac{\pi {w_{fin}}^2}{4} \tag{3.26}$$

$$SA_{CPF} = \frac{\pi {D_{fin}}^2}{4} + H_{fin} 2\pi \frac{D_{fin}}{2} \tag{3.27}$$

R_{fin} is the thermal resistance of all fins, h_{fin} is the heat transfer coefficient around the fins, SA_{RF} is surface area of one rectangular fin, SA_{CPF} is surface area of one circular pin fin and N_{fins} is the number of fins.

$$m = \sqrt{\frac{4h_{fin}}{k_{RFB}L_c}} \tag{3.28}$$

$$L_c = H_{fin} + \frac{w_{fin}}{2} \tag{3.29}$$

m is fin constant and is dependent on fin geometry. L_c is the characteristic length, the L_c of a rectangular fin is given below. For a circular fin L_c is the diameter of the fin (D_{fin}).

$$Nu_{fins} = 0.35(\frac{S_W}{S_L})^2 Re^{0.6} Pr^{0.36} \tag{3.30}$$

Nu_{fins} is the Nusselt number of staggered pin fins, and is it determined experimentally by [45]. Re is the Reynolds number corresponding to entrance velocity velocity (V_u) and Pr is the Prandlt number.

$$h_{fins} = \frac{Nu_{fins}k_{co}}{L_c} \tag{3.31}$$

h_{fin} is determined using the relationship between Nusselt number and h shown in equation 3.7. k_{co} is thermal conductivity of the coolant.

$$\Delta P = \frac{f_{fin}\rho V_{max} N_L}{2} \tag{3.32}$$

ΔP is the pressure drop across the rectangular fins.

$$\dot{m}_{fin} = \rho V_u N_W S_W w_{fin} \tag{3.33}$$

$$\dot{m}_{CPFs} = \rho V_u N_W S_W D_{fin} \tag{3.34}$$

$\dot{m}_{fin}$ and $\dot{m}_{CPFs}$ is the mass flow rate through to rectangular and circular fins, N_W is the number of fins rows widthwise, S_W is the widthwise space between two fins and ρ is the density of the coolant.

$$f_{fin} = \frac{3L_c}{G_w} {Re_{max}}^{-0.2} N_L \frac{L_c}{S_L} \tag{3.35}$$

The Darcy friction factor around the fins (f_{fin}) is estimated using Chilton and Generaux Method [46] and is only valid for $50 < Re < 2 \times 10^4$, N_L is the number of fin rows in lengthwise direction, S_L is the lengthwise spacing between centers of two fins and Re_{max} is the Reynolds of the coolant flow corresponding to maximum velocity found around the fins. Equation 3.36 shows how to calculate maximum velocity.

$$V_{max} = max\left(\frac{S_W V_u}{S_W - w_{fin}}, \frac{S_W V_u}{2(S_D - w_{fin})}\right) \tag{3.36}$$

$$S_D = \sqrt{{S_L}^2 + (S_W/2)^2} \tag{3.37}$$

S_D is the diagonal distance between two staggered fins.

It is important to note that the heat transfer coefficient mostly remains the same after the initial interaction with the fins [47], [48], [49], [50], [51] and as seen in the simulation results below, so the heat transfer coefficient calculated analytically is a good representative of the average heat transfer coefficient around the fins.

Lastly, the results are expected to have slightly higher values of a friction factor (f_f) and pressure drop(ΔP) than they would be in actuality. This is because the empirical correlations used to develop equations 3.35 and 3.32 are based on experiments conducted on circular pin fins. However as seen in Fig. 3.24 the rectangular fins have fillets of the size of the fin width. Thus the approaching flow interacts with similar geometry as it would in a circular fin array. This results in a similar fluid behavior for circular fins and the rectangular fins shown in this thesis.

Typically, circular pin fins have higher pressure drop due to turbulent wake or a periodic wake as the flow moves past them. However, many publications have utilized similar pressure drop and friction factor correlations with updated characteristic length to reflect the change in geometry [52] , [53], [54], [52], [55], [56], [57].

The analytical approach shown in this thesis is able to capture the overall physics of the heat, mass, and energy transfer accurately enough. The error in the analytical calculations of pressure drop and heat transfer coefficient is expected to be no more than 10-15 %. This amount of accuracy is enough to create multiple heat sink models and then simulate the most promising ones to get the temperature gradients and a higher accuracy overall.

Equation 3.21 is minimized subjected to following constraints:

1. $(S_L - l_{fin}) \times N_L < (l_{fb} - 0.003)$
2. $(S_W - w_{fin}) \times N_W < (w_{fb} - 0.003)$
3. $S_W \geqslant 0.002$
4. $S_L \geqslant l_{fin} + 0.002$

The constrains above represent design and manufacturing limitations, for example constraint one ensures that the number of fin rows in lengthwise direction do not extend beyond the length where the coolant flows, and also leaves a 1.5mm clearance on top and bottom of the fins to simplify assembly.

Similarly, constraint two ensures that the number of fin rows in widthwise direction do not extend beyond the length where the coolant flows, and also leaves a 1.5mm clearance on the right and left side of the fins to simplify assembly.

Constraints three and four ensure a minimum fin spacing so that the fin don't touch each other and have some space such that they can be machined and casted.

Using Genetic Algorithm (GA) multiple parameters can be optimized at once, however for this heat sink design GA was only used to optimize for S_W and S_L.

Table 3.3 shows boundary conditions used in the heat sink analytical analysis and CFD simulations on Fluent. Note that the the analytical analysis is done on a quarter section of the heat sink widthwise and the CFD analysis is done on the entire heat sink.

Table 3.3: Heat sink boundary conditions for analytical and CFD analysis

Parameters and boundary conditions	Value	Units
Power dissipated by all MOSFETs (Q_l)	60×36	-
Ambient temperature (T_{amb})	105	°C
Entrance velocity at each section (V_u)	0.47	m/s
Thermal conductivity of coolant (Glycol 50/50) (k_{RFB})	0.4578	w/m K
Thermal conductivity of heat sink (Aluminum) (k_{RFB})	176	w/m K
Length of heat sink base (L_{fb})	0.134	m
Width of heat sink base (W_{fb})	0.260	m
Thickness of the heat sink base (H_{fb})	0.003	m
Length of the heat sink where the coolant flows (l_{fb})	0.100	m
1/4 width of the heat sink where the coolant flows (w_{fb})	0.065	m
Length of fin (l_{fin})	0.012	m
Width of fin (w_{fin})	0.003	m
Height of the fin (H_{fin})	0.01125	m

Table 3.4 shows the key parameters to optimize.

Table 3.4: Parameters to optimize and their optimized value

Parameters to Optimize	Optimized value by GA algorithm	Units
Widthwise spacing between fins (S_W)	12	mm
Lengthwise spacing between fins (S_L)	16.8	mm

Fig 3.25(a) shows a CAD model of the optimized fin base that is used for simulations, and (b) shows the fin based used to make the prototype

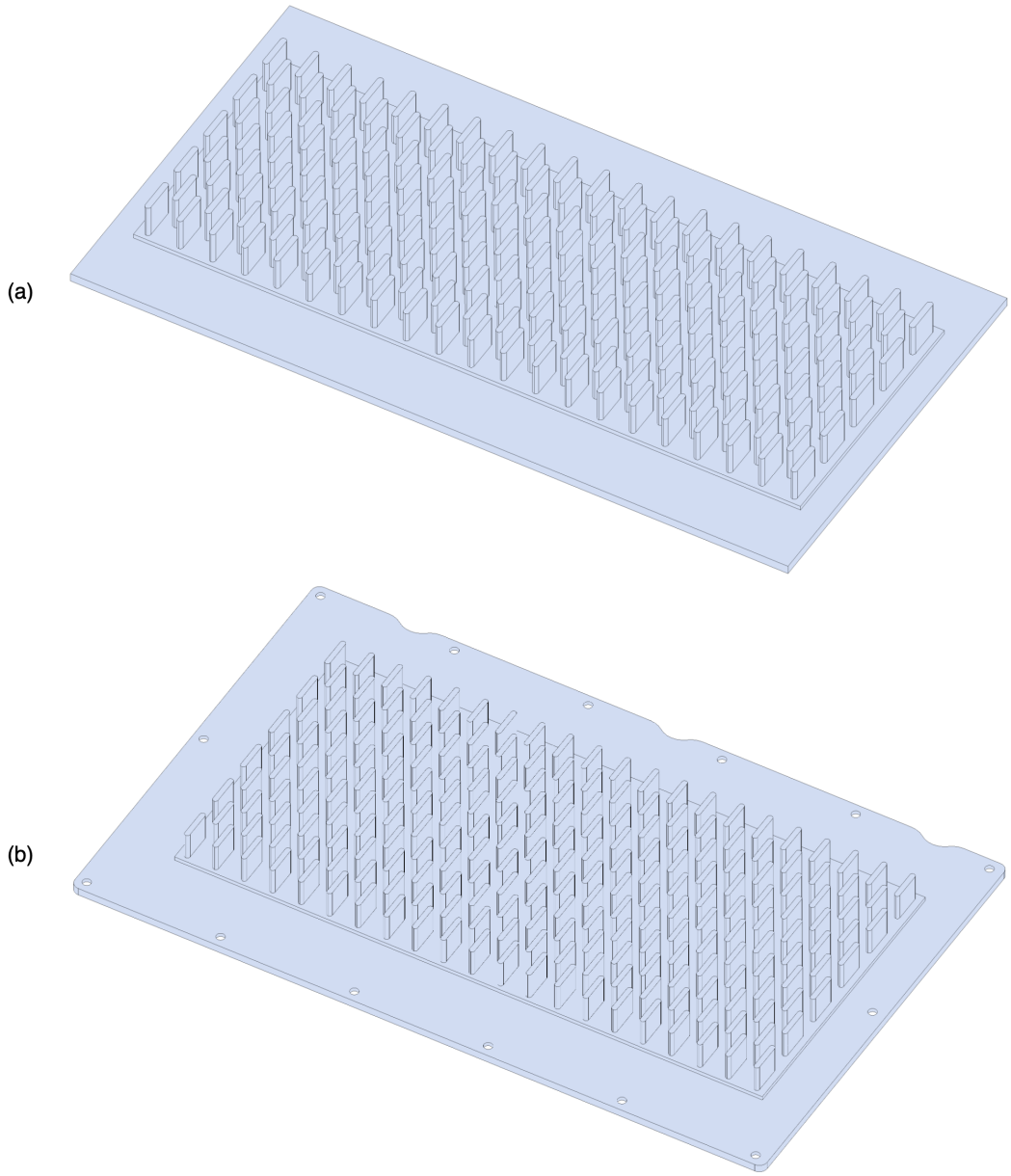

Figure 3.25: Optimized heat sink with rectangular fins (a) Simulation model (b) Prototype model

Simulation Results

Fig. 3.26(a) shows shows the case temperature of the MOSFETs and the pressure drop (b) . The maximum junction temperature of the MOSFETs is 134 ° C and max pressure drop is 7632 Pa.

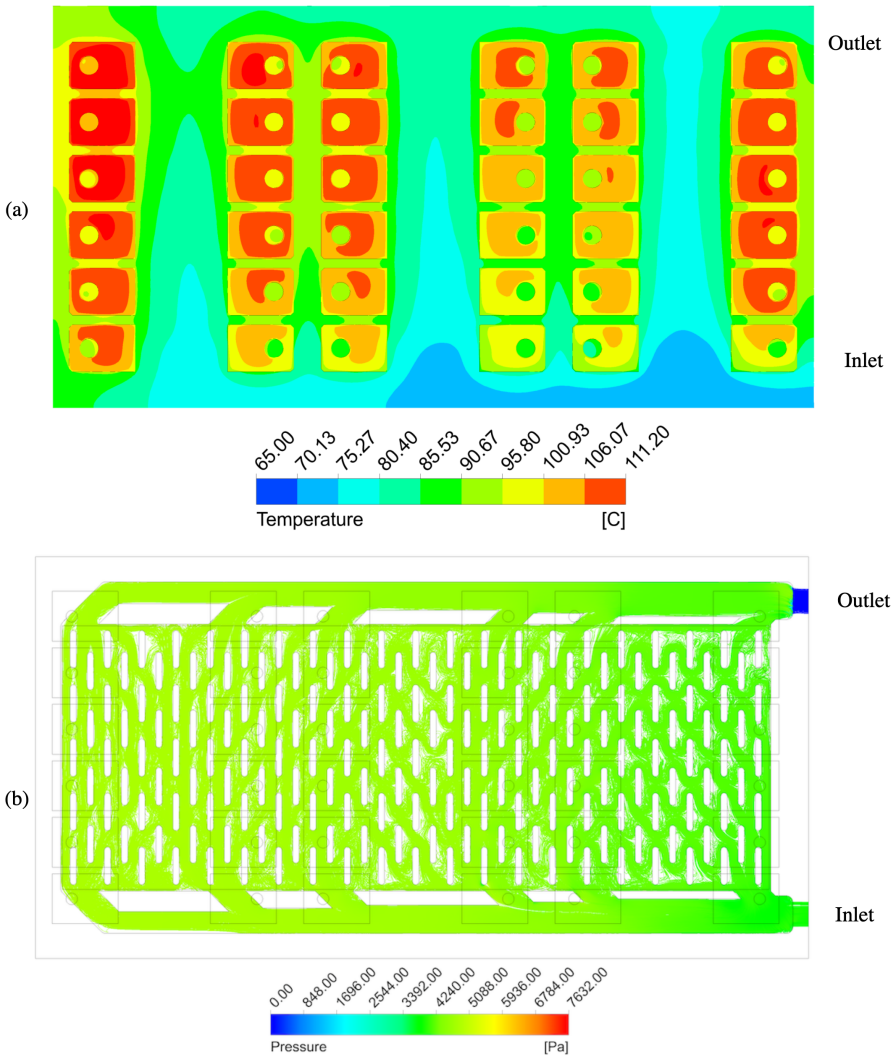

Figure 3.26: (a) MOSFETs case temperature gradients in an optimized finned coolant block (b) Pressure drop in an an optimized finned coolant block

Fig. 3.27 Shows the the velocity around the fins (a) and the heat transfer coefficient of the rectangular fins (b) . The average heat transfer coefficient is 4906 w/m^2 k this value matches closes with the values determined analytically (4304 w/m^2 k) using equation 3.31

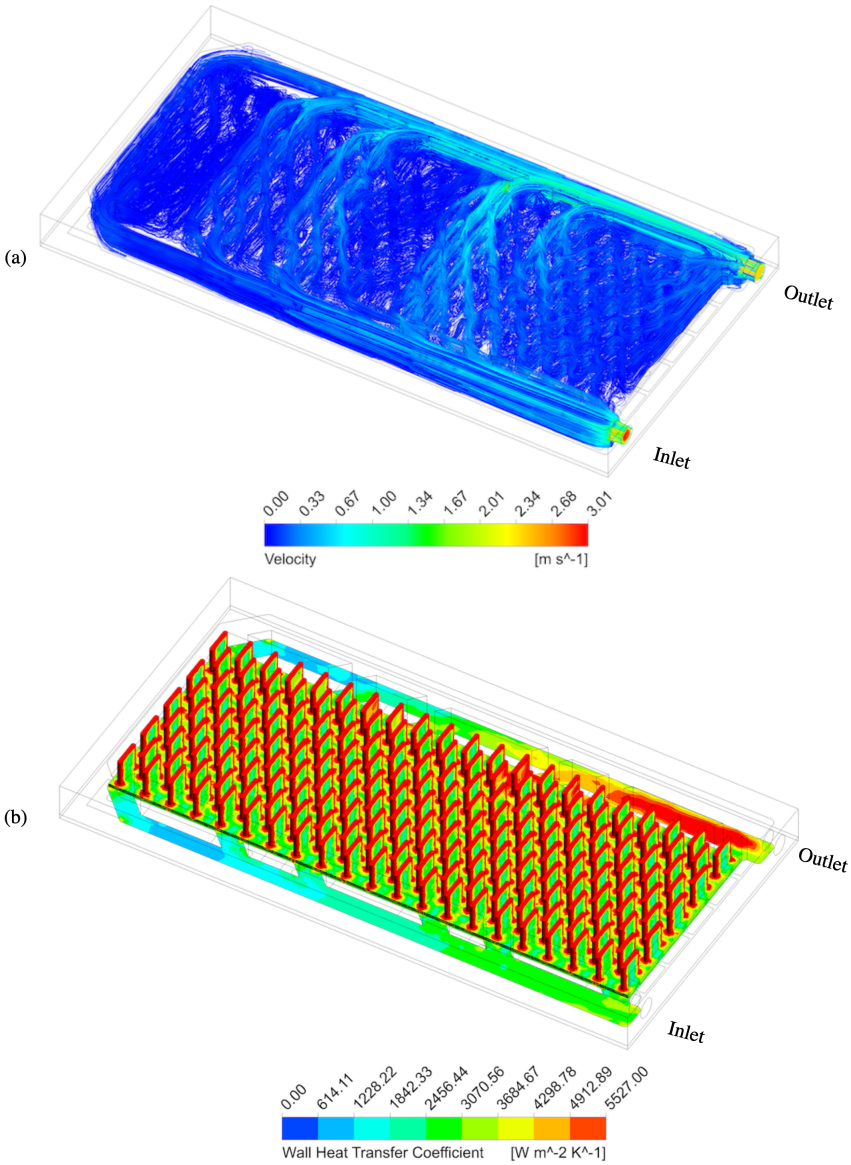

Figure 3.27: (a) Velocity streamline around the fins and the coolant block (b) Heat transfer coefficients around the fins

Table 3.5 summarizes the performance of the coolant block with a fin base. It is clear that this design fulfils all of the design criteria listed in section 3.2. The coolant block and finned based design is relatively light weight compared to the previous designs because the entire design is made from aluminum.

The performance of the finned base can be further improved by making it out of copper, however this will add significant weight, which is unnecessary since the aluminum fin base meets the required specifications.

Table 3.5: Heat sink boundary conditions for analytical and CFD analysis

Parameters and boundary conditions	Value	Units
Max MOSFET case temperature	111.20	°C
Max MOSFET junction temperature (T_j)	135	°C
Temperature Δ among the MOSFETs	6.2	°C
Total pressure drop ΔP	7632	Pa
Weight of the coolant (Glycol 50/50)	0.310	kg
Weight of the heat sink (Aluminum)	0.457	kg
Weight of coolant block (Aluminum)	0.415	kg
Total weight of the cooling components	1.18	kg

3.7 Summary

In this chapter important design criteria are defined for an ideal automotive cooling system. Three different cooling system designs are presented with analytical and FEA based approach to calculating pressure drop temperature gradients in a cooling system.

Analytical and FEA based solving approach is used to design and optimize the cooling system. This combined approach produces truly optimal design solution while requiring fraction of a computational and development time. Based on the analysis all the three proposed cooling systems, a coolant block with a rectangular finned base is the most optimal choice for the ANPC 120kW inverter because it provides excellent thermal performance without huge pressure drops. Table 3.6 shows a comparison between all the cooling systems presented and designed on key metrics.

Table 3.6: Comparison of pipe embedded cold plate, serpentine channel cold plate and coolant block with rectangular fin base on key parameters

Cooling System	Max T_j (°C)	Max TΔ between MOSFETs (°C)	ΔP (Pa)	Total weight (kg)
4 channel pipe embedded cold plate	140	11	6873	1.27
6 channel pipe embedded cold plate	126.5	8	1200514	0.893
6 channel serpentine horizontal cold plate	142.7	11.3	11325	1.71
6 channel serpentine vertical cold plate	161.4	19	5357	1.85
Optimized finned base with coolant block	134	6.2	7632	1.18

Chapter 4

Inverter Component Packaging for Improved Power Density

4.1 Component Selection

An optimal packaging of inverter components is not only important to achieve a high power density, but it is also important to simplify the assembly. Additionally, high voltage and high power inverters ($>$ 400V and $>$125kW) require special considerations during component placement to ensure that the high power components and low power components are isolated with adequate shielding and protection.

The selection of switching device package, capacitor package and cooling system also significantly affects the overall power density, packaging and assembly complexity. Sections below discuss solutions and techniques to minimize the weight and volume without negatively impacting power density.

4.1.1 Switching Device Package Selection

In chapter two, an optimal cooling system for the 120kW SiC ANPC inverter was presented. The inverter was built using discrete switching devices because currently, a power module package or an ANPC topology is unavailable Fig.4.1 shows a 2-level 350 kW power module package with its over all dimensions.

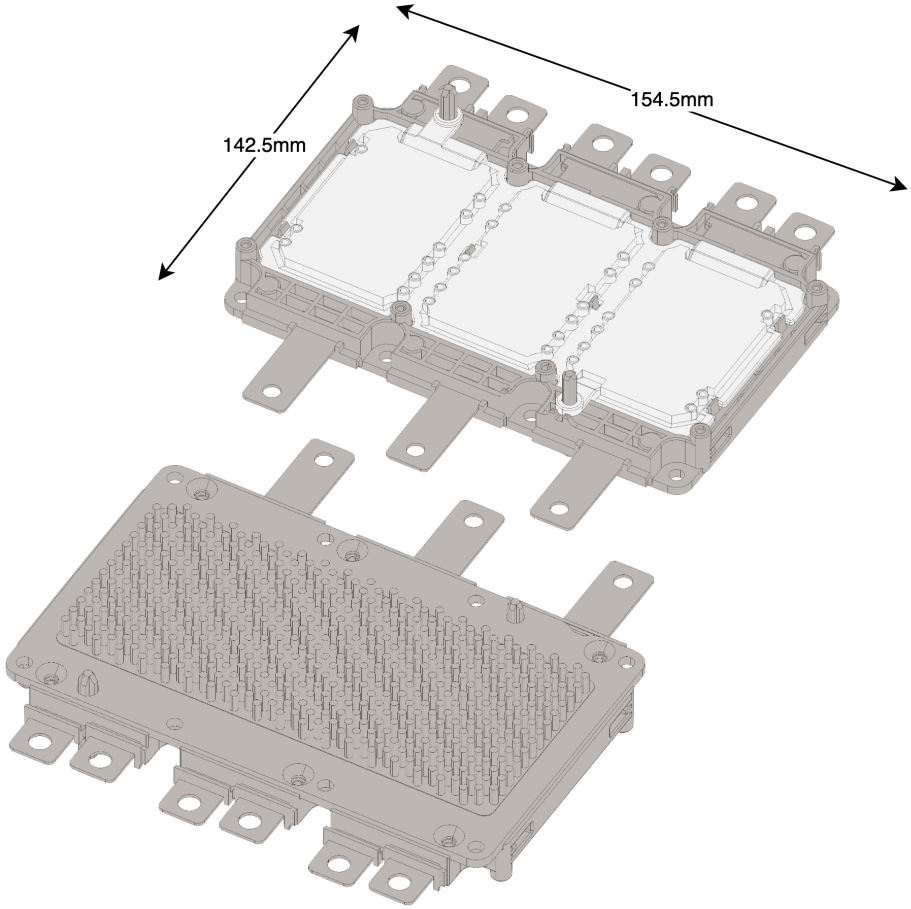

Figure 4.1: A 350kW power module: (a) Top ISO view, (b) Bottom ISO view

Fig. 4.2 shows the ANPC switches with an optimized heat sink designed in chapter 3.

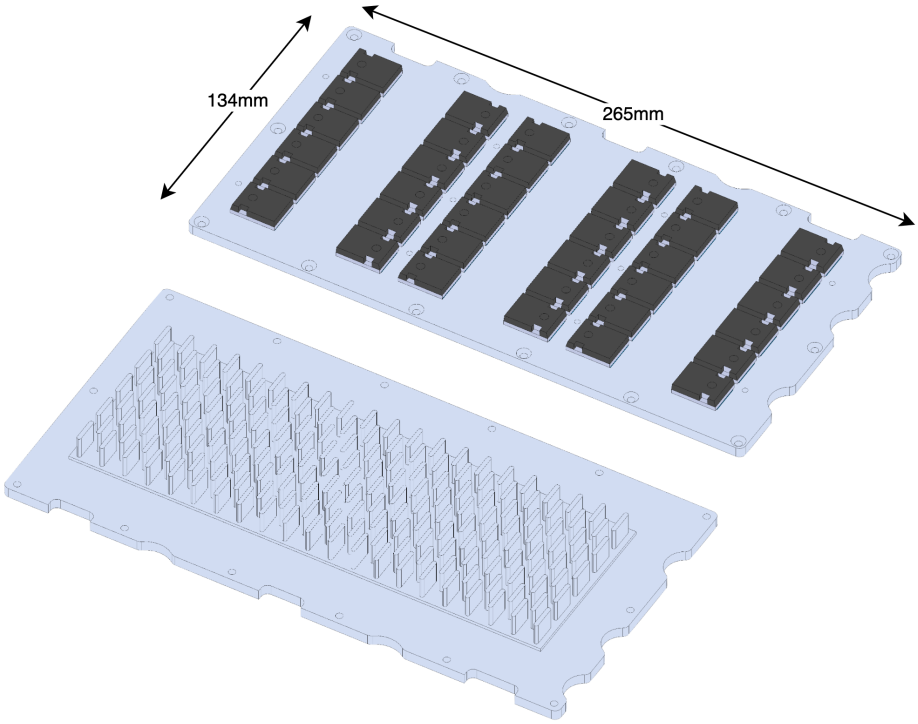

Figure 4.2: Discrete switching devices for the 120 kW ANPC inverter arranged underneath an optimized heat sink : (a) Top ISO view, (b) Bottom ISO view

It is clear that a power module is able to provide almost three times the power while occupying less than 46% of the surface area. The extreme difference in size is not only attributed to the limitations in power PCB design and gate driver design for discrete switching devices, but also to the physical size of the MOSFETs' case and the inverter topology.

Both the power module and the discrete devices use MOSFET dies of approximately the same size however in a power module package the dies are covered with a gel like encapsulation compared to a resin or plastic base potting for a MOSFET case in discrete devices. This occupies significantly more volume, and has a higher case to junction thermal resistance compared to a finned base of a power module package. The SO-247-4 package used in this thesis has a die size of approximately 4mm×6mm, while the entire package size is 15.5mm×21.5mm, which is more than 170% larger in surface area.

An additional benefit of utilizing a power module package is that the thermal management of the inverter is simplified because, typically, power modules especially high power module packages come with a finned base. Thus, additional analysis is not need to design a finned base. A coolant block that can provide a reliable coolant flow to the power module is needed, however this a relatively simpler challenge to solve. The inclusion of the heat sink and switching devices as a compact package also reduces assembly complexity and the number of parts needed to assemble the thermal management.

Lastly, a power module package has widespread adoption in the automotive industry, therefore auxiliary components such as current sensors that can easily integrate with power modules are readily available. The power terminals on the power modules are relatively unrestricted in their thermal performance because they are made of solid copper. Compared to discrete devices where either a PCB or busbar is needed to conduct the high currents. This not only adds additional components and complexity, but also increases weight.

4.1.2 Capacitor Package Selection

Similar to the switching device selection, capacitor selection is also important for packaging and assembly considerations in addition to electrical specifications. A bulk capacitor package is usually preferred over a discrete package. This is because discrete capacitors need to be soldered and are only held in place through the strength of the solder joints. This is not only suitable for mass production because of assembly complexity, but also because it cannot sustain any vibrations or mechanical loads which are unavoidable in a automotive application. Potting the discrete capacitors in place with resin can easily mitigate the mechanical issues but make the entire inverter un-serviceable, and does not solve the issue of assembly.

Generally, as the power density increases the ripple currents in the capacitor also increase. Conducting higher ripple currents require cooling of the capacitor. While the cooling does not need to be as aggressive as it is for the power module, it is still critical for reliable performance. Most of the solutions found in the literature regarding inverter thermal management [58], [59], [60], [61] focus only on the the thermal management of the switching devices. The SiC MOSFETs can withstand temperature of upto 175 °C , but the film capacitors can only handle 105 °C of temperature. A vehicle is expected to perform reliably and continuously at ambient temperatures of 105 °C. At steady state, even if the capacitor does not conduct ripple currents the temperature of the capacitor will be equal to the ambient temperature. Thus a cooling solution is necessary for the capacitor, unless it is designed for lower ambient temperatures.

4.1.3 Power Module Specification

Fig. 4.3 shows the circuit topology of a 2-level three-phase inverter for a motor drive system. The three-phase SiC power module used in this analysis is rated for 1200 V and 480 A continuous drain. While the power module is capable of 350kW, the capacitors and HVDC harness is not rated for such high currents, therefore the power is limited to only 250kW.

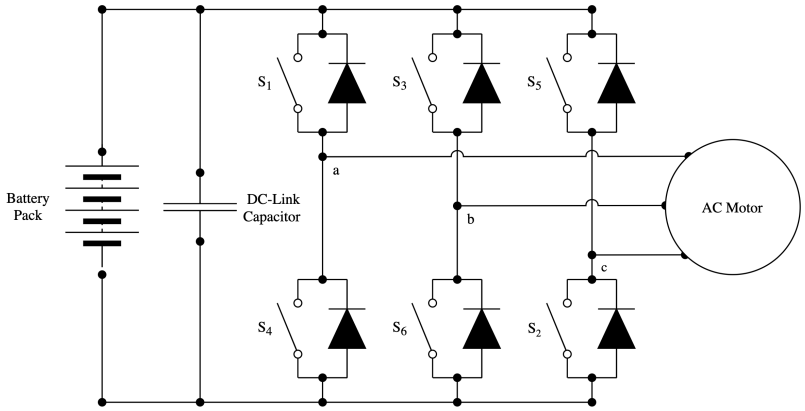

Figure 4.3: A 2 level VSI circuit topology

A typical power module package is an assembly that contains the switching devices and the diodes. These components are placed on top of multiple layers as shown in Fig. 4.4. The main purpose of these layers is to provide an electrical path for the current and gating signals as well to absorb the heat from the SiC MOSFETs, and transfer it to the layers underneath. The proper selection and design of the number of layers, layer thickness, and material is important. This is because the size of MOSFETs is small relative to the amount of heat flux generated by them. This high heat flux can cause significant temperature rise that can damage the switching devices or degrade the reliability of the power module package.

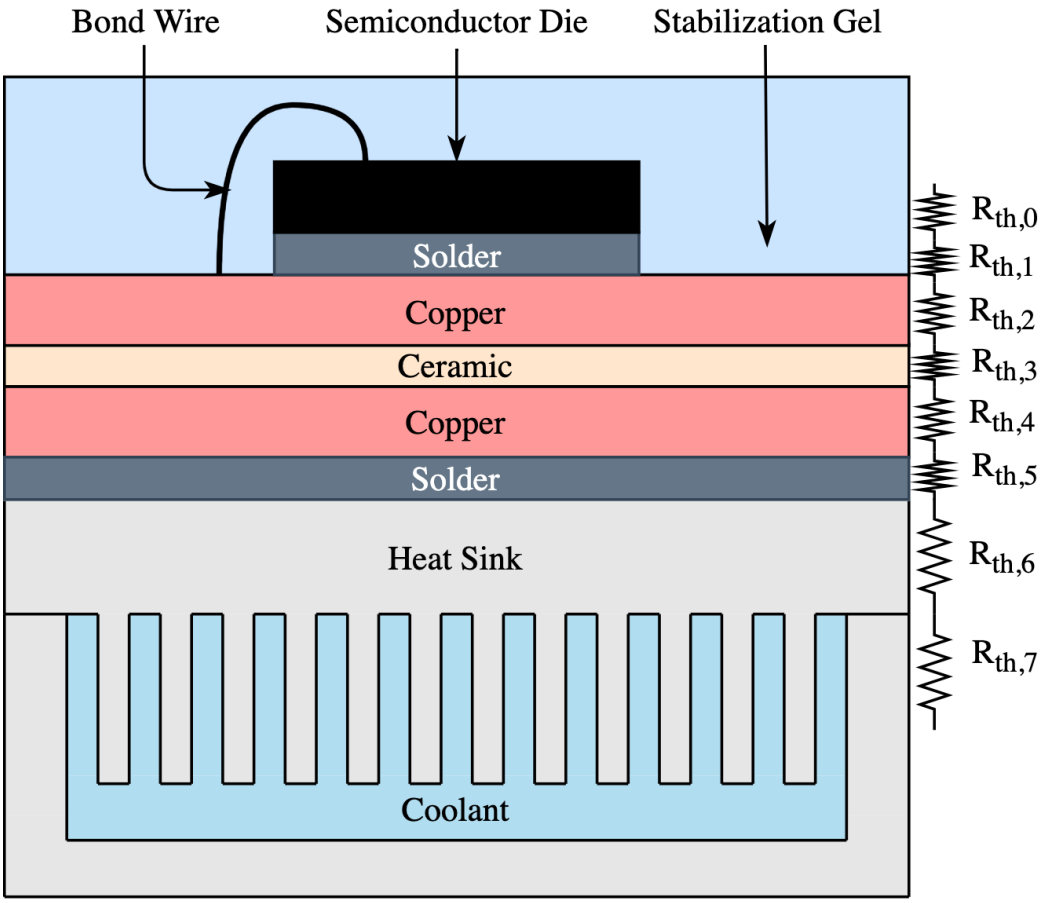

Figure 4.4: Layers and their respective thermal resistances in a power module package

In Fig. 4.4 $R_{th,0}$ - $R_{th,7}$ are the thermal resistances of the materials and layers of the power module. The goal of the cooling system design is to minimize $R_{th,7}$ by designing a coolant block that provides uniform coolant flow at highest possible velocity without increasing pressure drop beyond diminishing returns. $R_{th,6}$ cannot be changed because its value is determined by the design of power module.

4.1.4 DC-link Capacitor Specification

The DC-link capacitor used in this analysis is rated for 820 DC voltage. The internal structure is relatively simple compared to the power module. Fig. 4.5 shows the layers of the capacitor. The capacitor housing consists of capacitor cells sandwiched between the positive and negative busbars. $R_{th,0}$ - $R_{th,9}$ are the thermal resistances and the goal is to minimize $R_{th,0}$ and $R_{th,1}$. Typically, original equipment manufacturer (OEM) specifications require one of the capacitor's surface to be maintained at a specific temperature. In this design the top surface needs to be maintained at 75 °C while the maximum power loss from the capacitor is 60 watts.

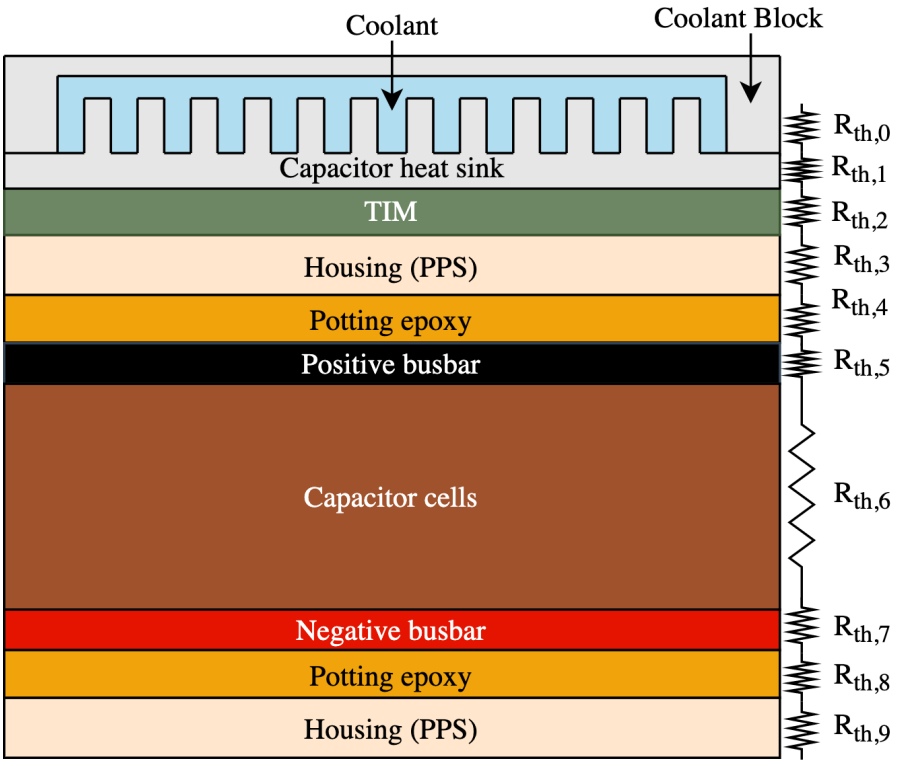

Figure 4.5: Layers and their respective thermal resistances in a bulk capacitor package

4.2 Switching Device and Capacitor Thermal Management

Since both the switching device and the capacitor require thermal management, it is important to carefully consider the placement and design of different thermal management solutions so that it can provide effective cooling for both the components. Fig. 4.6 shows a power module and a bulk capacitor package placed side by side. This is the most common topology and it is utilized in many designs shown in the literature [62], [63], [64], [65] [66]. However none of them have any thermal management for the capacitor.

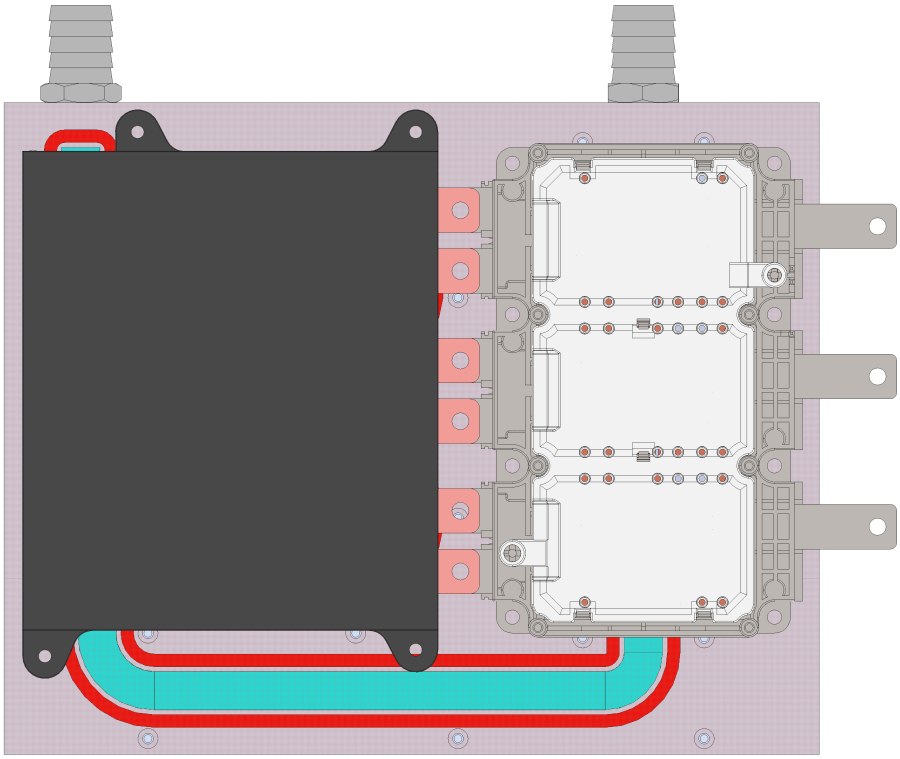

Figure 4.6: Arranging power module and the capacitor side by side with thermal management solution underneath

The thermal management of such a topology can include a mix of serpentine coolant channels and an integrated coolant block for the power module that floods the pin fin base.

Fig. 4.7 shows an exploded view of one of the considered thermal management solutions. Based on the analysis shown in chapter 3, the pressure drop in this system is expected to be very high.

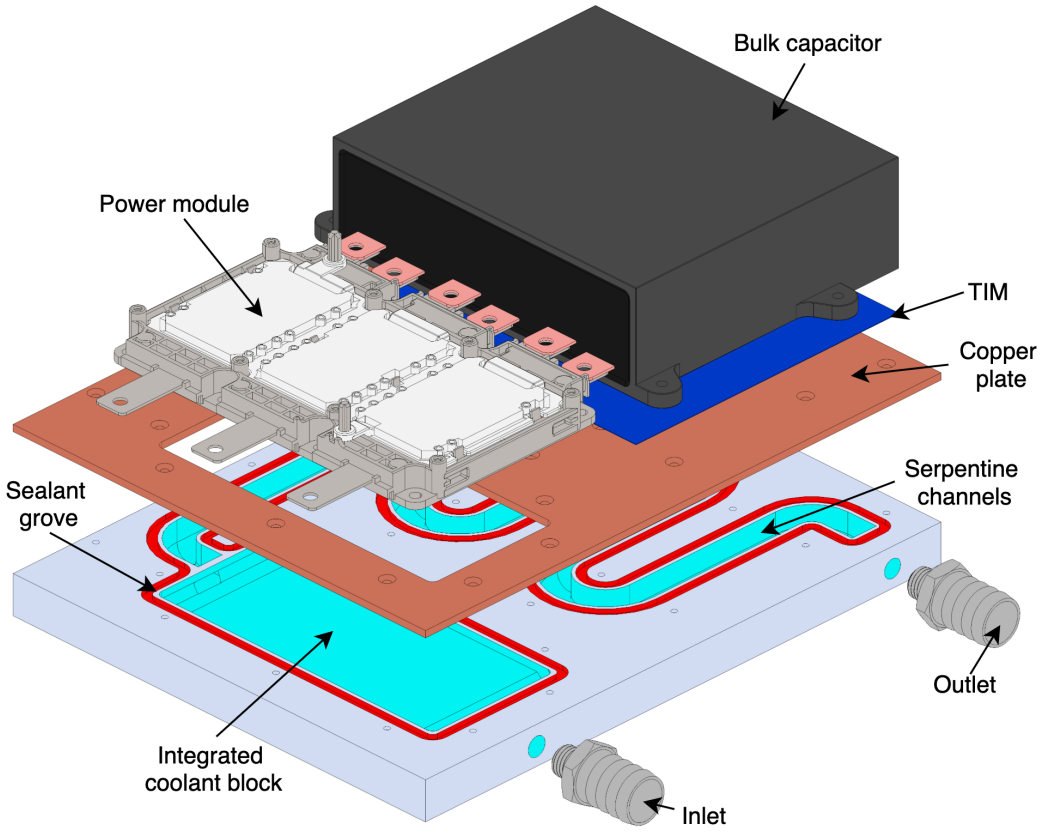

Figure 4.7: An Isometric exploded view of a cooling system from power module and the capacitor arranged side by side

Fig 4.8 shows the serpentine coolant channels and the coolant block. Fig. 4.6 and 4.8 show a side by side thermal management solution. It occupies excessive volume (1.1 L) and is also the heaviest design presented so far (3.7 kg). A significant portion of the weight is due to the copper cold plate, (1.3 kg), an aluminum plate can be used instead of copper, however this will impact thermal performance.

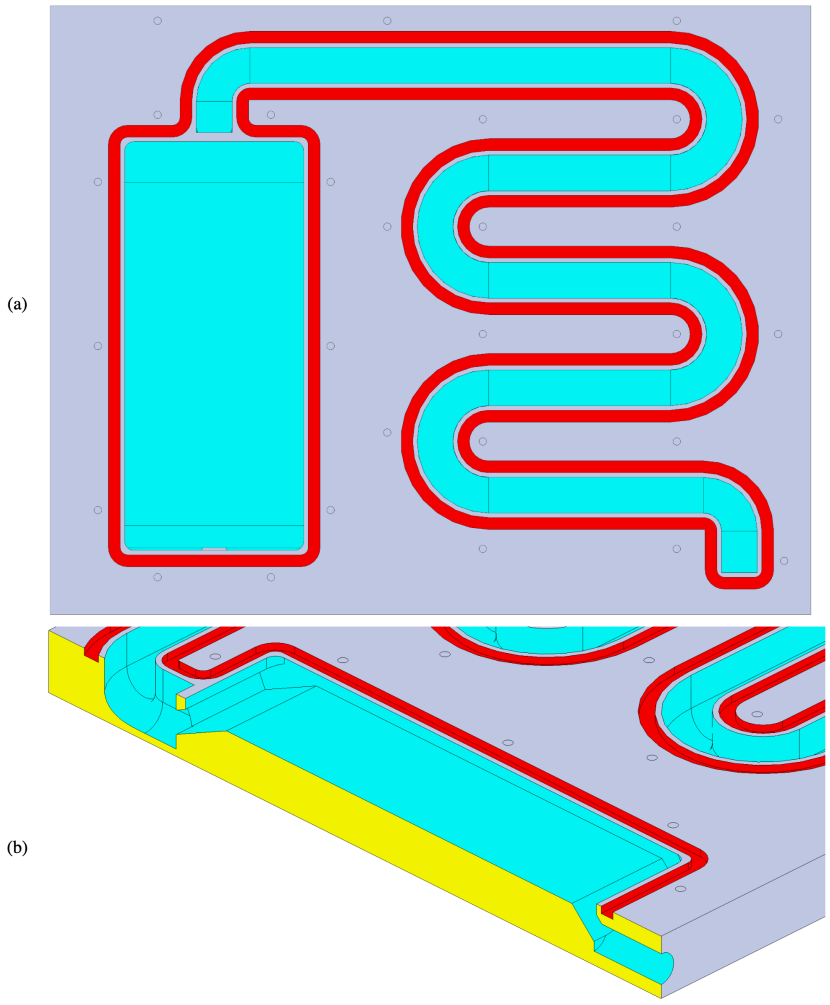

Figure 4.8: A serpentine channel and coolant block based cooling system for a power module and bulk capacitor: (a) Top view (b) Cross sectional view of the integrated coolant block

4.2.1 Proposed Stacked Cooling System

Rather than having two separate cooling systems for the power module and the capacitor the proposed solution involves designing a stacked cooling system where a coolant sits between the power module and the capacitor as shown in Fig. 4.9

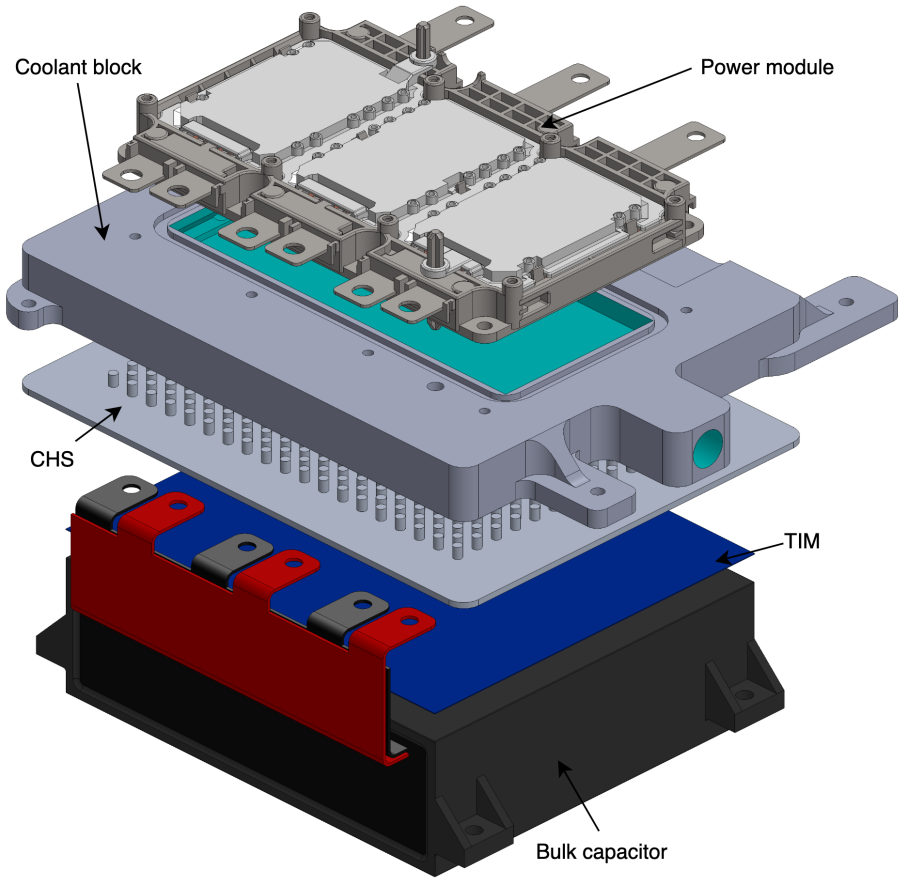

Figure 4.9: An exploded view of the proposed stacked cooling system

One of the primary goals of an ideal thermal management solution is to provide a compact design, thus the design shown in 4.7 is not ideal. A typical power module package comes with a circular pin fin base that is designed by the supplier. The DC-link capacitor is designed by another supplier and it generally requires thermal management on either the top or the bottom of the capacitor surface.

In order to incorporate two different cooling mechanisms of the power module and DC-link capacitor, the cooling system is split into two main components: the coolant block and the CHS, as shown in Fig. 4.9

Adding CHS over a flat plate heat sink has three main advantages:

- The CHS can be designed to complement the power module's pin fin design so that uniform coolant flow can be achieved on both top and bottom sections.
- The circular pin fins help in mixing of the coolant, increasing the turbulent kinetic energy, and thus enhancing the rate of heat transfer.
- The pin fins are more effective in transferring heat from the capacitors via conduction, as compared to a flat surface.

While the circular pin fin geometry increases the pressure drop, an optimized design will minimize the pressure drop. Additionally, the increase in pressure drop is not significant enough to negatively impact the design. Lastly, achieving a comparable thermal performance from flat plate heat sink is not possible while occupying same weight and volume.

One one of the minor challenges associated with the stacked cooling system is that the busbar that makes connection with power module and the capacitor is large, and thus increases the stray inductance. If the stray inductance is very high it can result in voltage overshoot that can damage the switching devices and also the capacitor. Guidelines and techniques presented in [67], [4] are used to design and optimize busbar design to minimize stray inductance.

While the stray inductance of arrangement shown in Fig. 4.7 is going to be lower than the one shown in Fig. 4.9, it is important to realize that the configuration shown in Fig. 4.9 occupies is 73 % less volume and is 102 % lighter. Only the weight of the cooling system and coolant is considered since the power module and bulk capacitor used in both analysis are the same.

The last, challenge associated with a stacked cooling system is that the entire mechanical load from the coolant block, power module, current sensors, AC and DC harness is applied on the top surface of the capacitor. Most modern capacitor housings are made from a thermo-plastic such as Polyphenylene Sulfide (PPS) therefore it is not ideal to subject the entire capacitor to the mechanical load form the components above it. This can be easily mitigated by providing supports in the housing for the coolant block to rest on. Thus load from the coolant block and components above it are equally dispersed into the housing and not just the capacitor, this also adds mechanical rigidity to the structure. The overall benefits of a stacked cooling system significantly outweighs the potential challenges hence it is an ideal choice of arrangement for a high power density.

4.2.2 Capacitor Heat Sink (CHS) Design

The capacitor heat sink is responsible for dissipating the heat flux generated by the capacitor. In order to compliment the pin fin design of the power module, a staggered pin fin arrangement is used for CHS. The CHS is designed using the same techniques and similar equations shown in chapter 3. In this analysis in addition to dissipating 60 watts of power from the heat sink, the maximum surface temperature of the thermal interface material touching the capacitor should not exceed 75 °C.

Thus a sweeping search of minimum entrance velocity needed is performed to ensure that capacitor surface temperature is maintained at a given value. The sweeping space is narrowed by determining maximum possible velocity in the lower section, assuming all of the flow is directed to the bottom section. The maximum velocity in the bottom section is calculated to be 2.164 m/s using equation 3.18, since the max flow rate and the cross sectional area (in the bottom section) needed for the equation is known.

Velocity in increments of 0.01 m/s up to the max velocity of 2.164 is fed to the GA optimizer until the velocity that maintains temperature of 70 °C or less (safety margin of 5 ° C) is determined along with the fin spacing in lengthwise and widthwise direction. The ideal velocity is found to be 0.08 m/s. Since the cross sectional area of the bottom section is constant, the flowing sections will show how the coolant block is designed so that the flow rate is redirected to achieve the needed entrance velocity.

Fig. 4.10 shows a layout of the CHS and the parameters that are optimized.

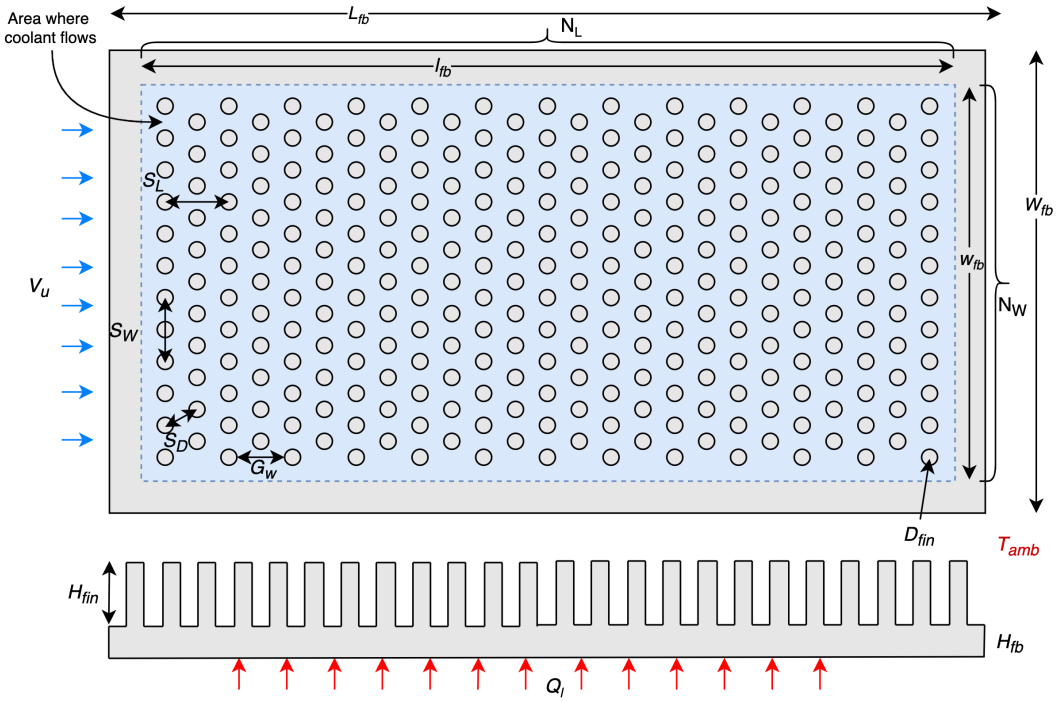

Figure 4.10: CHS along with the fin layout and the necessary parameters used in analysis

Figure 4.11 shows the CAD model of the CHS used for simulation

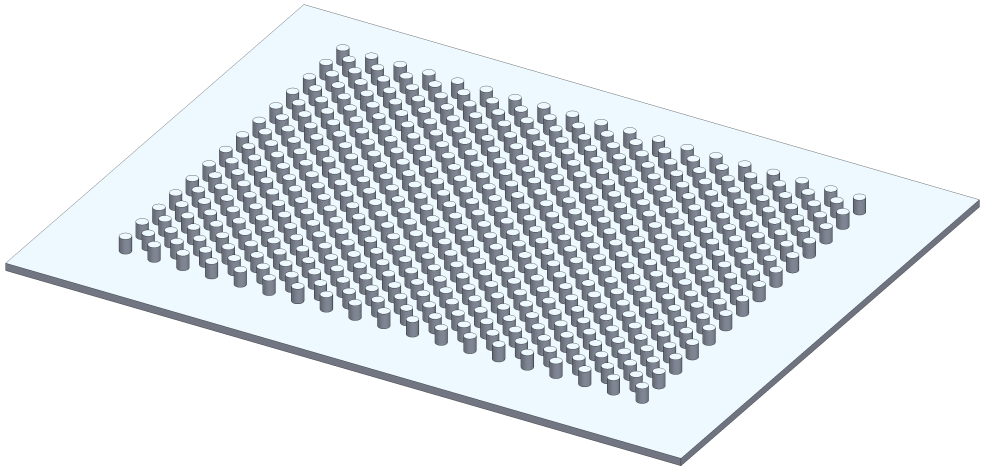

Figure 4.11: CAD model of CHS used for simulation

The boundary conditions for CHS analysis are listed in table 4.1

Table 4.1: Heat sink boundary conditions for analytical and CFD analysis

Parameters and boundary conditions	Value	Units
Power dissipated by all MOSFETs (Q_l)	1300	-
Ambient temperature (T_{amb})	105	°C
Entrance velocity around CHS (V_u)	0.08	m/s
Thermal conductivity of coolant (Glycol 50/50) (k_{co}	0.4578	w/m K
Thermal conductivity of heat sink (Aluminum) (k_{RFB})	167	w/m K
Length of heat sink base (L_{fb})	0.183	m
Width of heat sink base (W_{fb})	0.140	m
Thickness of the heat sink base (H_{fb})	0.002	m
Length of the heat sink where the coolant flows (l_{fb})	0.145	m
width of the heat sink where the coolant flows (w_{fb})	0.115	m
Height of fin (l_{fin})	0.004	m
Diameter of the fin (w_{fin})	0.003	m

Table 4.2 shows the parameters that are optimized in the CHS design.

Table 4.2: CHS optimized values

Parameter to optimize	Value	Units
Ideal entrance velocity V_u from sweeping search	0.08	m/s
GA optimized widthwise spacing between fins (S_W)	0.00685	m
GA optimized lengthwise spacing between fins (S_L)	0.00736	m

4.2.3 Double Sided Coolant Block Design

The coolant block is responsible for providing a path for the coolant to flow through the power module pin fins and the DC-link capacitor heat sink. The geometry of the coolant block is crucial as it dictates the coolant velocity, the uniform distribution of the coolant velocity, and the pressure drop. These factors ultimately influence the heat transfer coefficient, the design principles and motivation is similar to the ones discussed in chapter 3.

The coolant block in this section is designed for perpendicular coolant flow as compared the parallel flow in 3.6.1. The main motivation behind designing for perpendicular flow is that the power module fins are designed for perpendicular flow. Additionally, the distance coolant has to travel across the pin fins is relatively short, thus the pressure drop and the temperature distribution is expected to be relatively low in perpendicular flow.

Fig.4.12 shows the cross sectional view of the coolant block.

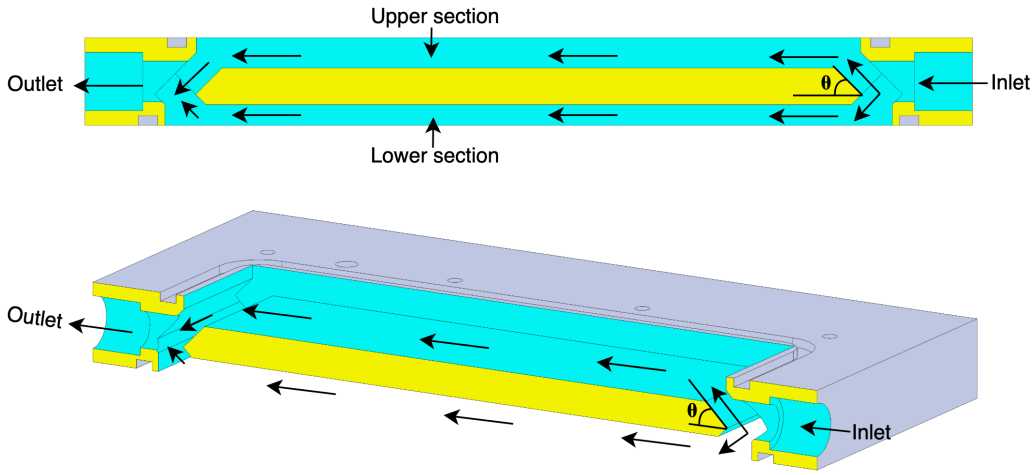

Figure 4.12: Cross sectional view of the coolant block for double sided cooling

As seen in Fig 4.12 the inlet flow rate is split so that some of the flow is redirected to the bottom section. The percentage of the flow redirected is based on the minimum entrance velocity (V_u) needed to maintain 75 °C on the capacitor surface and was calculated earlier.

Using equation 3.18 the minimum flow rate needed to maintain a entrance velocity of 0.08 m/s^2 across the bottom section is 2.44 L/min. Thus in order to achieve a flow rate of 2.44 L/min in the the bottom section approximately 37 % of the flow must be redirected from an initial value of 8L/min. This is achieved by adjusting the angle θ shown in figure 4.12

Simulation Results

Fig. 4.13 shows the surface temperature of the capacitor surface, it is about 5 °C less than the maximum allowable value.

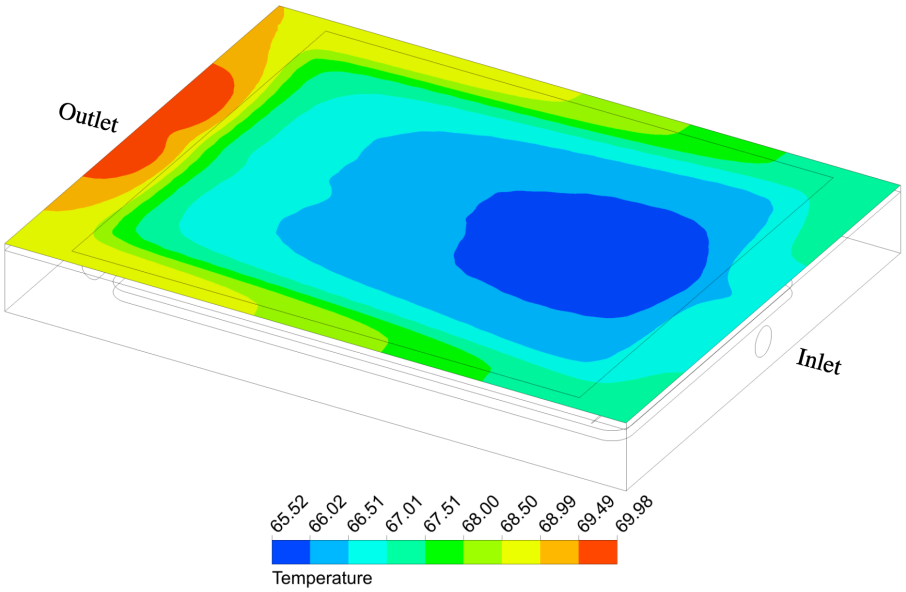

Figure 4.13: Temperature of the top capacitor surface

Fig. 4.14 shows the temperature gradients of the power module and SiC die temperatures along with the pressure drop. The max SiC temperature is 97.7 °C and the maximum pressure drop is 6101 kPa. The temperature delta of the MOSFETs is only 9 °C.

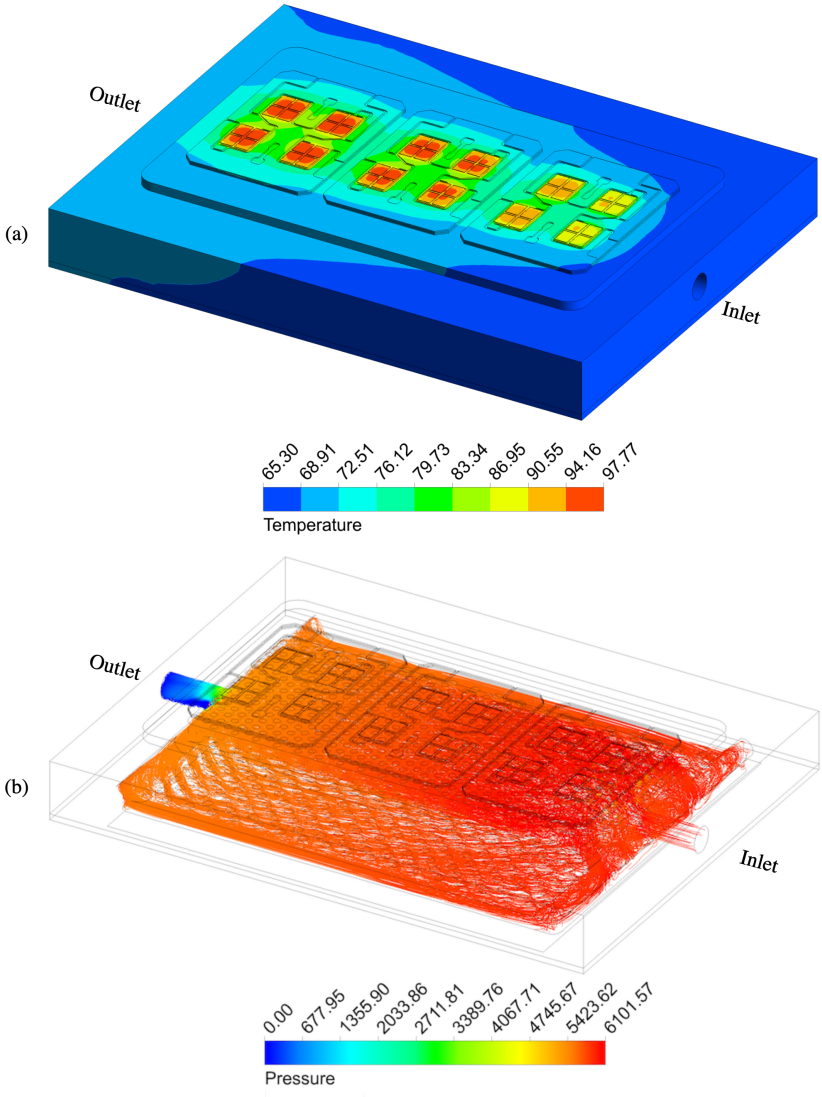

Figure 4.14: Double sided coolant block simulation results: (a) SiC temperature gradients (b) Pressure drop

Fig. 4.15 shows the heat transfer coefficient around the power module pin fins and the CHS. The average heat transfer coefficient is 5550 $w/m^2\,k$ around the power module fins and 4930 $w/m^2\,k$ around the CHS. These values closely match the analytical results.

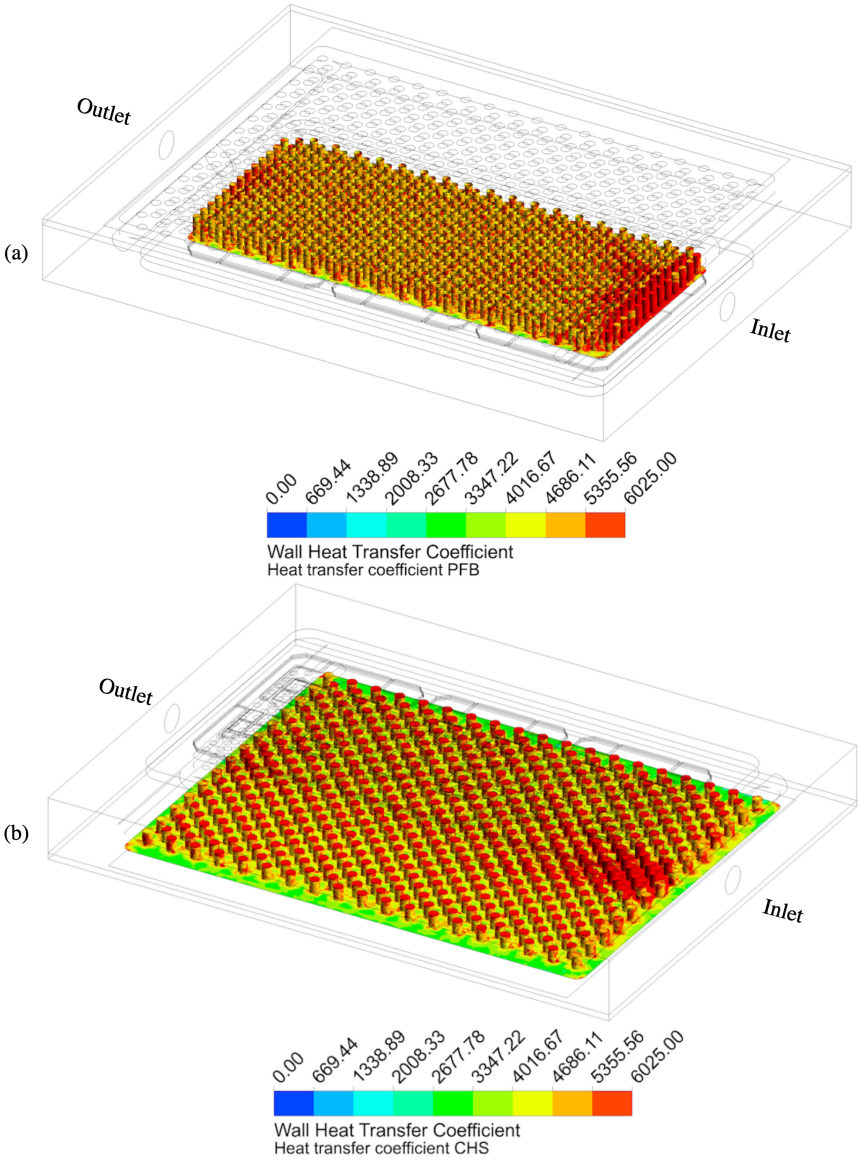

Figure 4.15: Double sided coolant block simulations results:(a) Power module pin fins heat transfer coefficient (b) CHS heat transfer coefficient

4.3 Strategic Integration of the Thermal Management into the Housing

The strategic integration of the thermal management into the inverter housing is extremely important. A proper integration allows for a compact design that occupies minimal volume. After the power module and DC-link capacitor the cooling system is the third largest component inside the inverter. Historically, inverters have utilized off the shelf cooling systems to speed up the design process and save development time and costs.

However, as the trend moves towards high power low volume inverters it becomes less feasible to implement an off the shelf component into a traction inverter meant for production. This is because an off the shelf components does not offer the flexibility and adaptivity to fit the numerous design constrains of an inverter. Instead the inverter housing needs to be designed around the cooling system. This also reduces the scalability of the design.

The goal of this section is to present how the thermal management solutions designed earlier can be integrated into inverter housing design while maintaining low volume, low weight and have a high power density. A 120kW, 30.3 kW/L SiC ANPC inverter design using discrete devices is presented along with a 250kW, 47kW/L 2-level SiC power module based inverter design. Each of the proposed designs adhere to strict automotive standards while following some of the most basic DFMA guidelines to improve manufacturability and assembly process.

4.3.1 120kW 3-ANPC SiC Inverter

Fig 4.16 shows an exploded view of the entire 120kW ANPC inverter assembly with all of its components

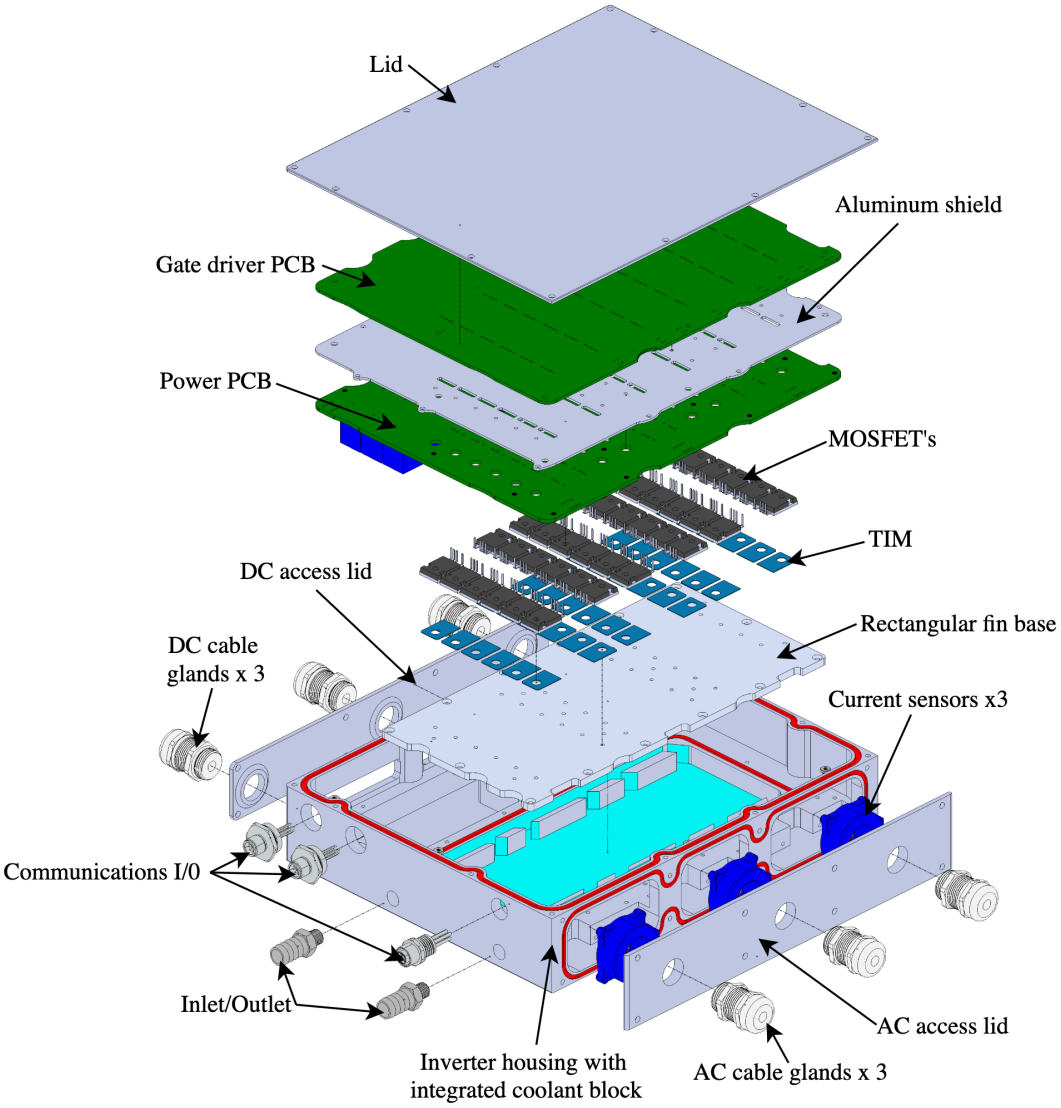

Figure 4.16: Exploded view of the 120sikW ANPC inverter

Fig. 4.17 shows the coolant block shown if Fig. 3.20 integrated into an housing design for the 120kW ANPC inverter. By integrating the coolant block into the housing the number of assembly steps along with weight and volume of the assembly have been reduced.

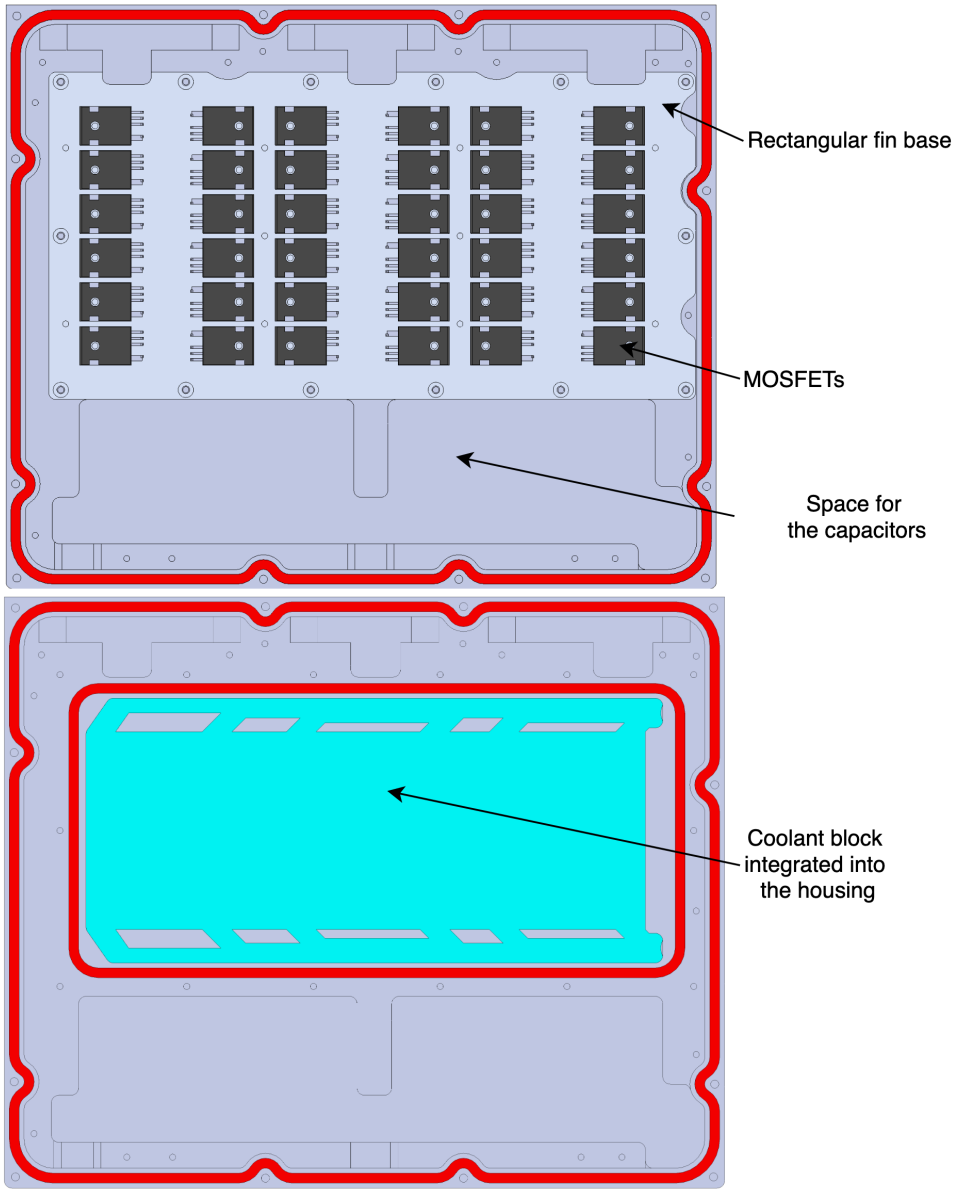

Figure 4.17: Integrating coolant block into the Inverter housing

Figure 4.18 shows the machined and assembled prototype of the 120kW ANPC inverter. Coolant pressure tests were done to ensure that the coolant does not leak during normal operation.

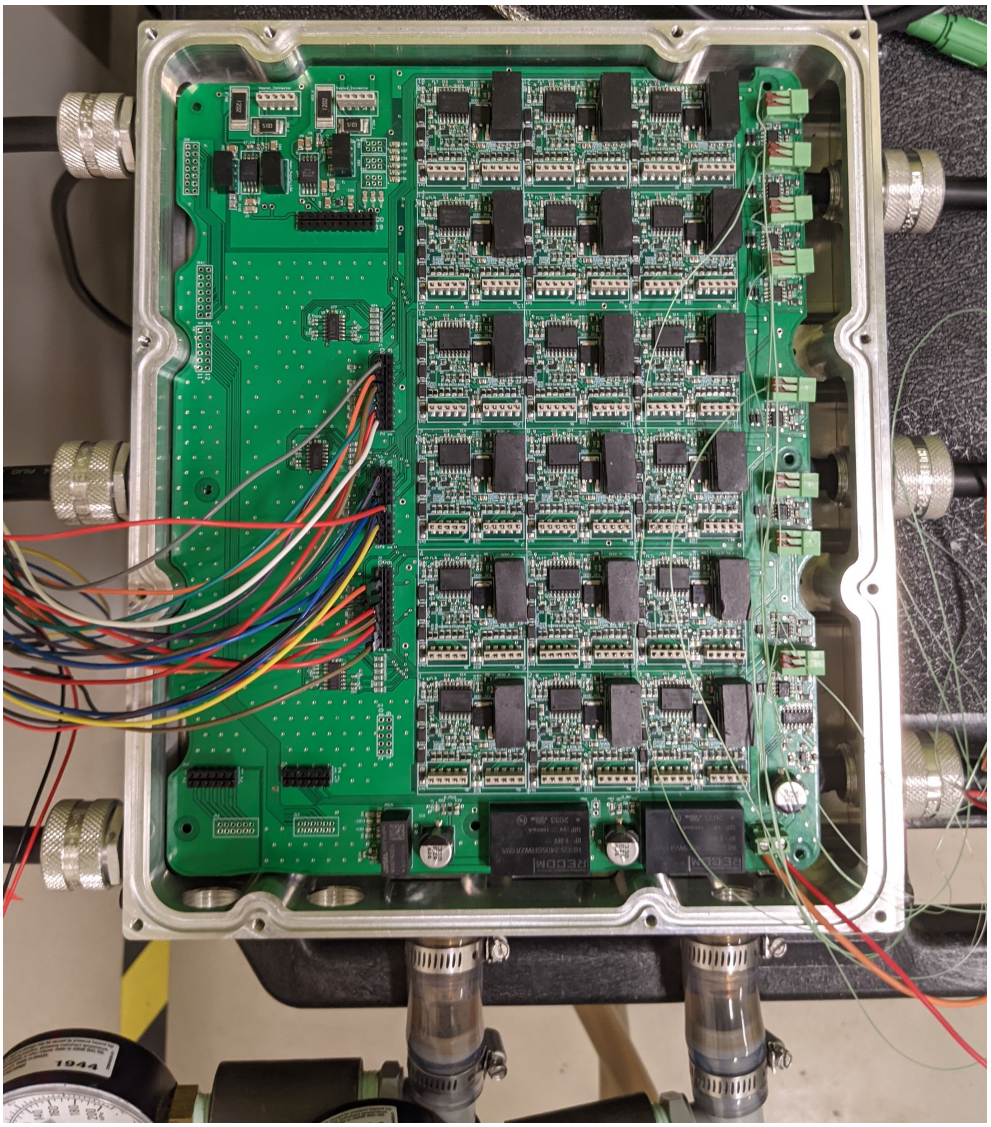

Figure 4.18: Top view of the assembled 120kW ANPC inverter without lid.

Figure 4.19 shows the the 120kW ANPC inverter with its over all dimensions. Fig.4.20 shows the front view of the inverter. The proposed design has a power density of 30.3 kW/L and the final weight of the the components including all the fasteners is about 7.2 kg.

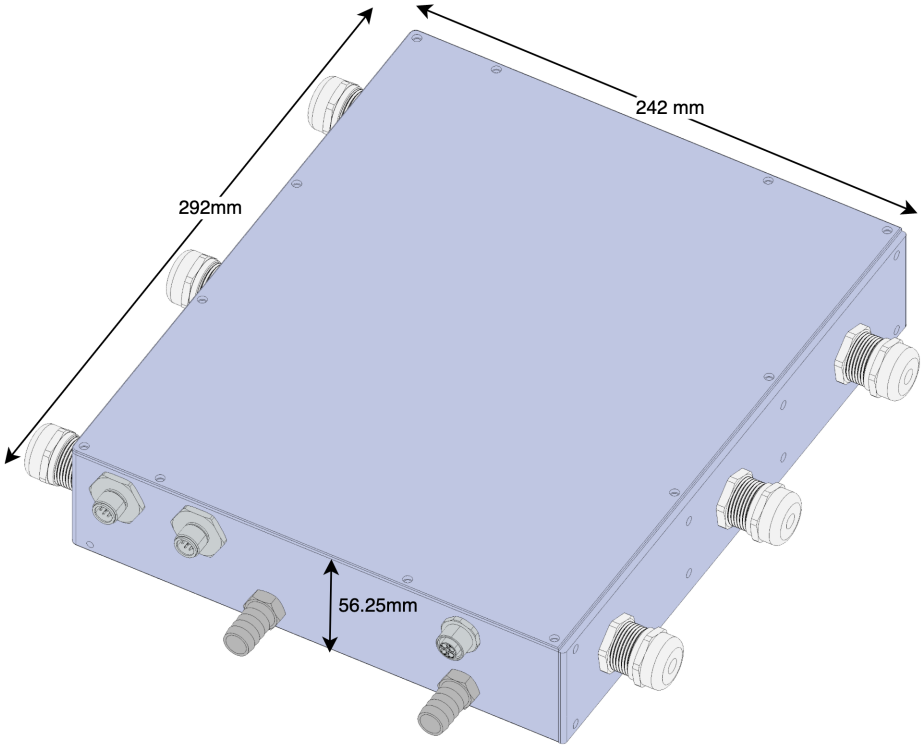

Figure 4.19: ISO view of the 120kW ANPC inverter with its overall dimensions

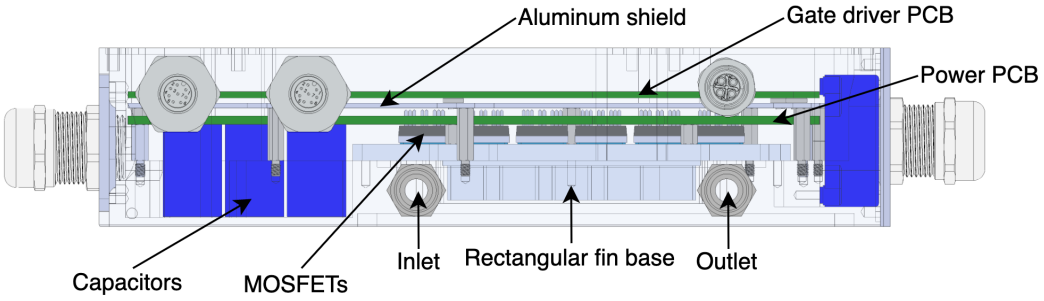

Figure 4.20: Front view of the 120kW ANPC inverter that shows how the PCBs are stacked above the MOSFETs

4.3.2 250kW 2-Level SiC Inverter

Figure 4.21 shows an exploded view of a propsed 250 kW SiC 2-level inverter using a power module package and a stacked double sided cooling system. Additionally, Just like the 120kW ANPC inverter, this inverter can also be easily assembled top down, with the exception of the communications I/0

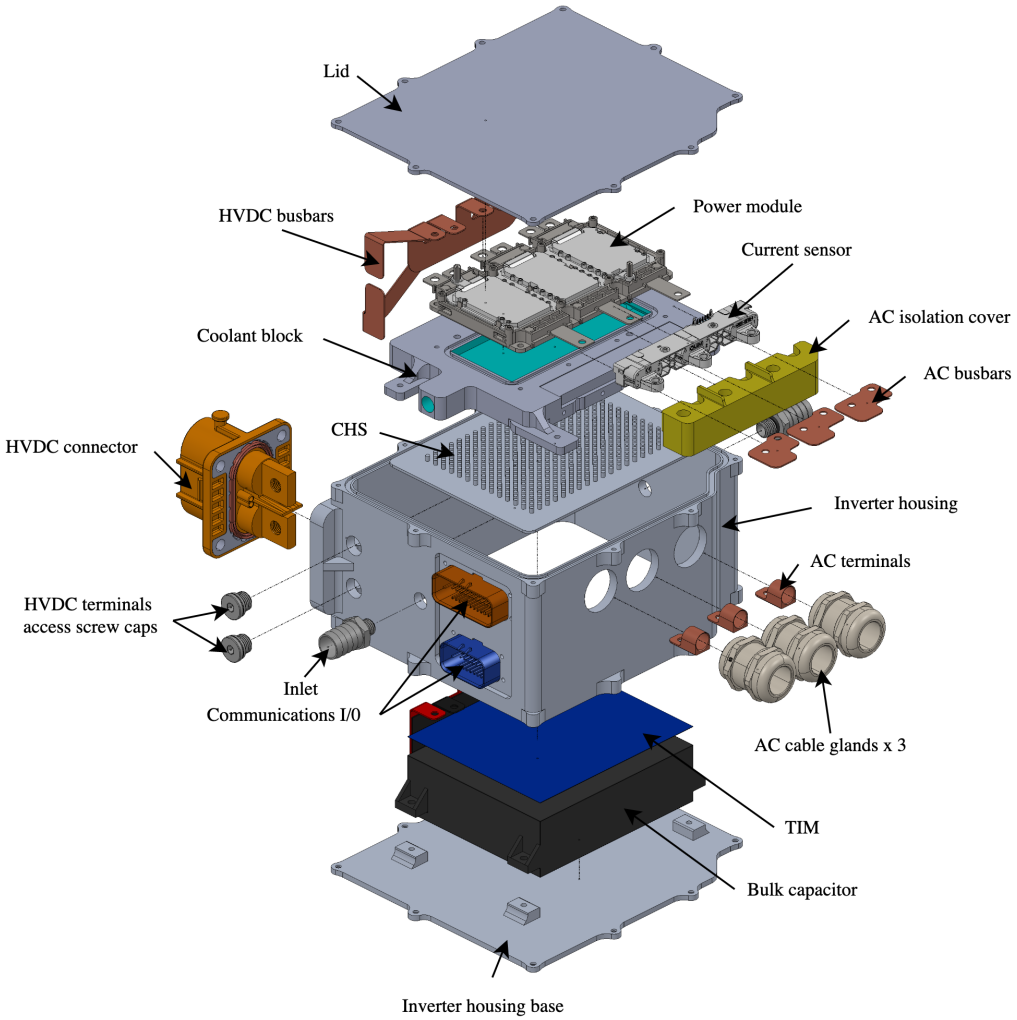

Figure 4.21: Exploded view of the 250kW ANPC inverter

Fig 4.22 shows the stacked cooling system shown in 4.9 integrated into the inverter housing. The four locations (circled in red) are part of the housing body and provide mounting locations for the coolant block and act as load distribution points.

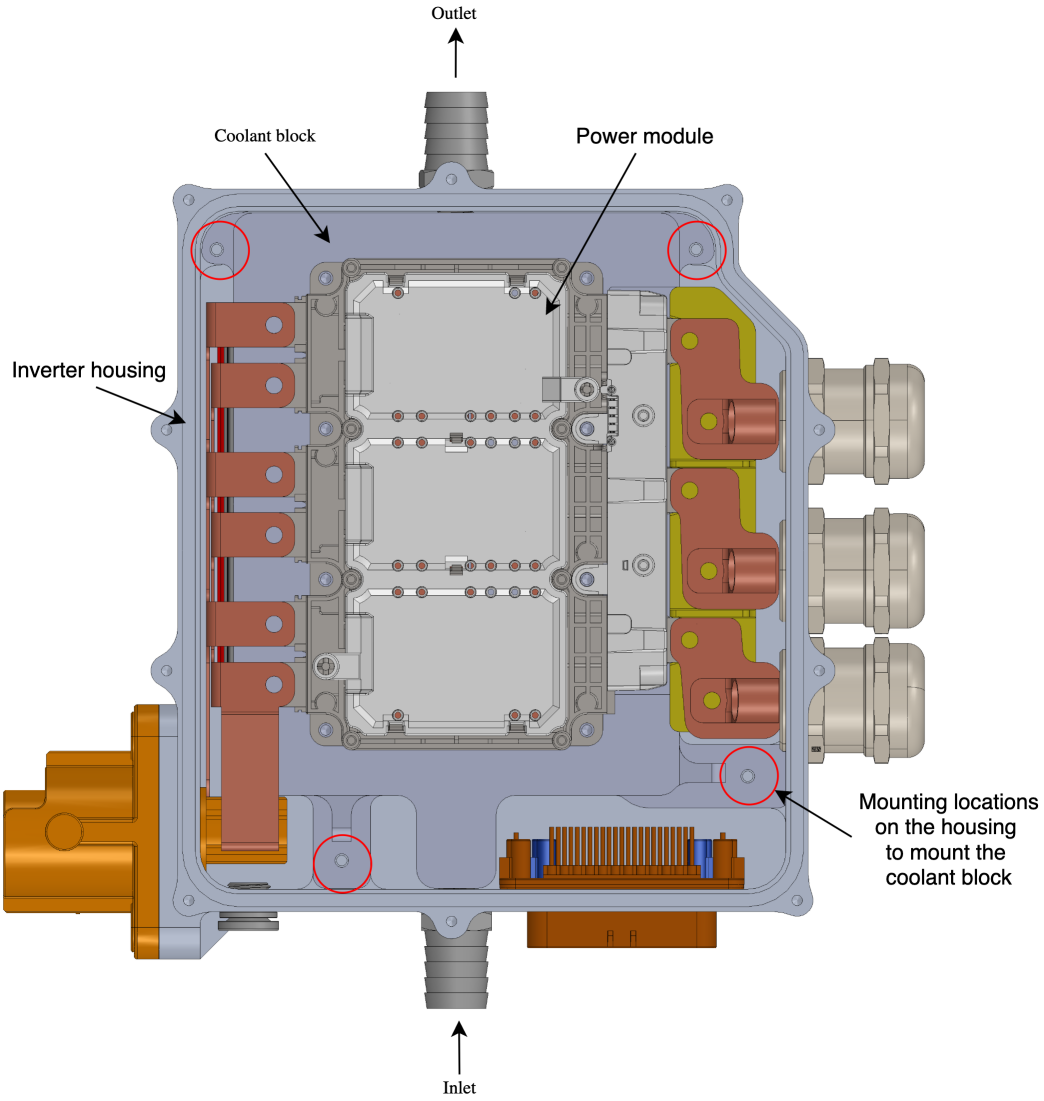

Figure 4.22: Top view of 250kW 2-level SiC inverter

Fig 4.23 shows the overall dimensions of the 250kW SiC 2-level inverter. Utilizing a bulk capacitor package and power module package certainly helps in improving the power density, provided it comes at an expense of a 2-level topology, and the coolant inlet and outlet ports are on opposite sides. The estimated weight of the proposed design is about 6.5 kg

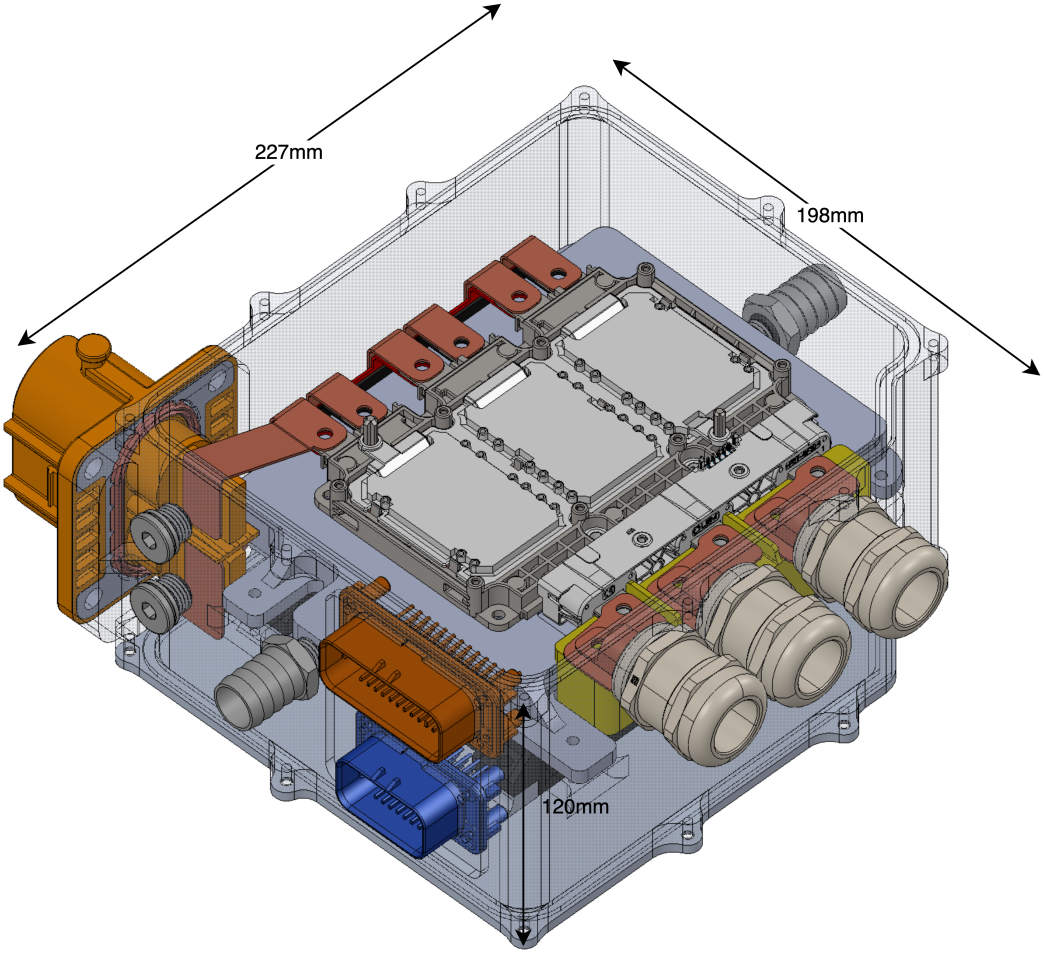

Figure 4.23: ISO view of 250kW 2-level SiC inverter with its overall dimensions

4.4 Summary

This chapter presents an comprehensive analysis on components that can help in improving the power density of the inverter. Typically, as the power density increases the capacitor also starts requiring some level of thermal management. In order tackle the issue of providing cooling for the switching devices and the capacitor, a compact, lightweight and optimized double sided cooling system is presented. Using this design, a 250kW, 47kW/L 2-level SiC inverter utilizing a power module package is presented. Additionally, a 120 kW, 30.3kW/L 3-level ANPC inverter housing design is presented that utilizes the optimized rectangular finned based cooling system presented in chapter three.

Table 4.3: Summary of the two inverter designs presented

Topology	ANPC 3-Level	2-Level
Power (kW)	120	250
Power density (kW/L)	30.3	47
Weight (kg)	7.2	6.5
Cooling system type	Finned base with coolant block	Stacked double sided cooling
Switching device package	discrete SO-247-4 package	Power module
DC-link capacitor package	Discrete capacitor cells	Bulk capacitor

Chapter 5

Vibrational Analysis of Inverter Housing

5.1 Mechanical Loads Analysis

A typical traction inverter is expected to experience various mechanical loadings from vibrations generated during vehicle operation. Vibration is a physical phenomenon that occurs in any moving object. For a vehicle, even simple day to day activities such as driving can induce these vibrations that move through chaises of the car and vibrate the inverter. Generally, determining what causes these vibrations, their exact frequency and the magnitude is extremely challenging.

With the emergence of integrated drives, vibrations from the gearbox and motor can also induce mechanical loads on the inverter because of its close proximity, in addition to the scenarios described earlier. Lastly, auxiliary moving components such as pumps, compressors and radiator fans inside a vehicle generate vibrations as they operate, these vibrations can also move through the chassis, get amplified and vibrate the inverter.

Generally, Standards such as ISO 16750-3 have been used to define potential vibrations with specified magnitude and frequency in ICE vehicles. However, well defined standards for vibrational analysis on EV integrated drives do not exist yet, thus various OEMs have developed their own standards in addition to applying standards made for ICE vehicles.

The first step in conducting vibration analysis is performing modal analysis, the results of modal analysis are used to conduct various vibration analysis such as harmonic analysis, random vibration analysis, transient dynamic analysis and spectrum response.

For the purpose of this thesis only modal and harmonic analysis are conducted on the 120kW ANPC inverter. The Harmonic analysis is used to predict the steady state dynamic response of the inverter subjected to sinusoidally varying loads. The frequency and the magnitude of the loads will be discussed in the following sections.

5.2 Modal Analysis

Modal analysis is a linear analysis that provides dynamic characteristics of a system. It does not utilize any loads or excitations to perform the analysis, instead the modal analysis is only a function of the stiffness of the system and its mass. Thus, it is important to represent the geometry and the materials as accurately as possible. If the information cannot be represented accurately, then the natural frequencies and modal shape extracted will not representative of the actual system

Typically modal analysis is conducted to determine the natural frequencies and the corresponding modal shapes of a given system. Once the natural frequencies are known, it is critical to ensure that the system is not excited at the extracted natural frequencies, otherwise the system will undergo resonance that generates stresses which can cause damage and excessive displacement. Equation 5.1 describes the equation of motion with basic force balance.

$$[M]\{\ddot{S}\} + [C]\{\dot{S}\} + [K_{st}]\{S\} = \{f(t)\} \tag{5.1}$$

For modal analysis, the equation is simplified to

$$[M]\{\ddot{S}\} + [K_{st}]\{S\} = 0 \tag{5.2}$$

Where, $[M]$ is the mass matrix, $[C]$ is the damping matrix and $[K_{st}]$ is the stiffness matrix. $\{f(t)\}$ is the force as a function of time, and $\{S\}$, $\{\dot{S}\}$ and $\{\ddot{S}\}$ represents the displacement, velocity and acceleration respectively.

Equation 5.2 basically represents a system without acceleration (sitting still), or moving at a constant velocity in the time the domain. This equation by its self does not represent any meaningful loading conditions to the system, thus it is assumed that every element of the system experiences harmonic motion. This shifts the system from time domain to frequency domain. Substituting, the following equations into equation 5.2.

$$S = \phi_i sin(\omega_i t + \theta_i) \tag{5.3}$$

$$\ddot{S} = {\omega_i}^2 \phi_i sin(\omega_i t + \theta_i) \tag{5.4}$$

The equation of motion in frequency domain becomes,

$$(K_{st} - {\omega_i}^2 M)\phi_i = \{0\} \tag{5.5}$$

where, ϕ_i is the amplitude, ω_i is the angular frequency and θ_i is the phase angle. This a typical eigenvalue problem that is solved by the Ansys using FEA.

Theoretically, a system has same number of modal shapes as the Degrees of Freedom (DOF). This means that even simple structures can have hundreds, if not thousands of natural of mode shapes. Generally it is impractical to extract thousands of mode shapes.

In order to determine if enough mode shapes are extracted the mode participation factors and effective mass ratios of the analysis is checked. The mode participation factor is a measure of how much mass moves in a specified direction for the given mode. Generally, a higher value means that the mode will be excited by excitation in that direction. Effective mass ratio is the ratio of the mass that is excited compared to the mass of the system.

Initially, arbitrary number of mode shapes are extracted, then the mode participation and effective mass ratio is checked through the FEA software. A effective mass ratio close to one indicates that that enough mode shapes have been extracted because modal shapes that cause significant mass excitation have been identified. While it is possible to obtain a effective mass ratio of one for an unconstrained system, for constrained systems the mass participation cannot be one. An unconstrained system will have three modal shapes at a natural frequency close to zero or at zero, each representing unconstrained movement of the system as whole in X,Y and Z space.

For a constrained system some of the mass is fixed, therefore the DOF in the system are reduced, thus reducing the number of modal shapes and the effective mass ratio. In general, constraining the system is desirable as it increases the stiffness of the system, making it less prone to vibrations, effectively shifting the values of natural frequencies up. The modal analysis is done on all the inverter components, including the power PCB and gate driver PCB. Since the stiffness of the PCBs will be higher due to the layering, copper tracing and components soldered on the PCB, the results shown are a bit conservative.

5.2.1 Modal Analysis Simulation Results

Initially, 80 modal shapes were extracted, however the average effective mass ratio for X, Y and Z directions was 0.44, 0. 75 and 0.23. In order to improve the reliability of the simulations additional 120 mode shapes were extracted.

The effective mass ratio for this analysis was 0.94, 0.93 and 0.88 respectively. Most of the mode shapes identified were associated with the power and gate driver PCBs. Figs. 5.1- 5.4 show some of the mode shapes with the highest excitation in their respective directions. Note that the total deformation value shown in the plots has no physical significance because no loads are applied.

The first mode shape of the inverter is at 123.02Hz, and is associated with the gate driver PCB. The simplest solution to shift up the natural frequencies is to increase the stiffness of the PCBs by supporting it better (adding more fasteners and mounting locations).

However, adding fasteners on the power power PCB and the gate driver is constrained by the PCB design process, which is out of the scope of this thesis. Additionally, the stiffness of the PCB in this analysis is underestimated, thus the significance of a low natural frequency depends on the peak displacement and stresses experienced at resonance.

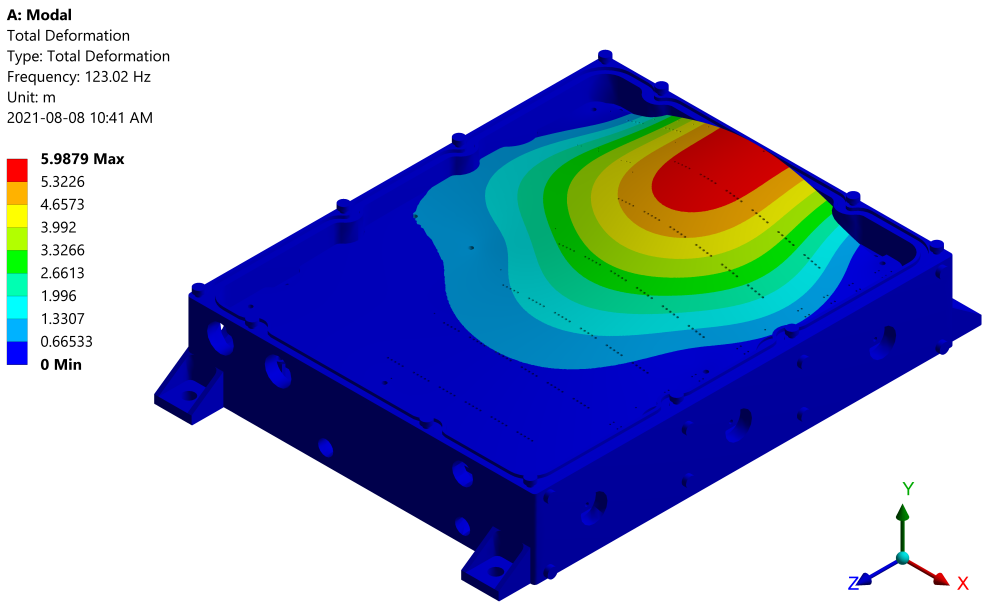

Figure 5.1: Modal analysis:Mode shape 1 with natural frequency of 123.02 Hz, the gate driver has highest excitation in Y direction

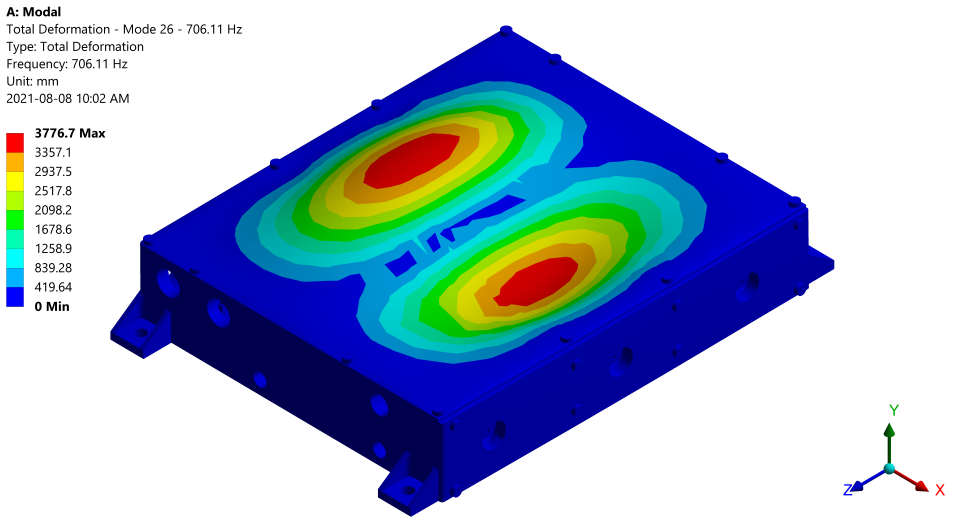

Figure 5.2: Modal analysis: Mode shape 26 with natural frequency of 706.11 Hz, the lid has highest excitation -Y direction

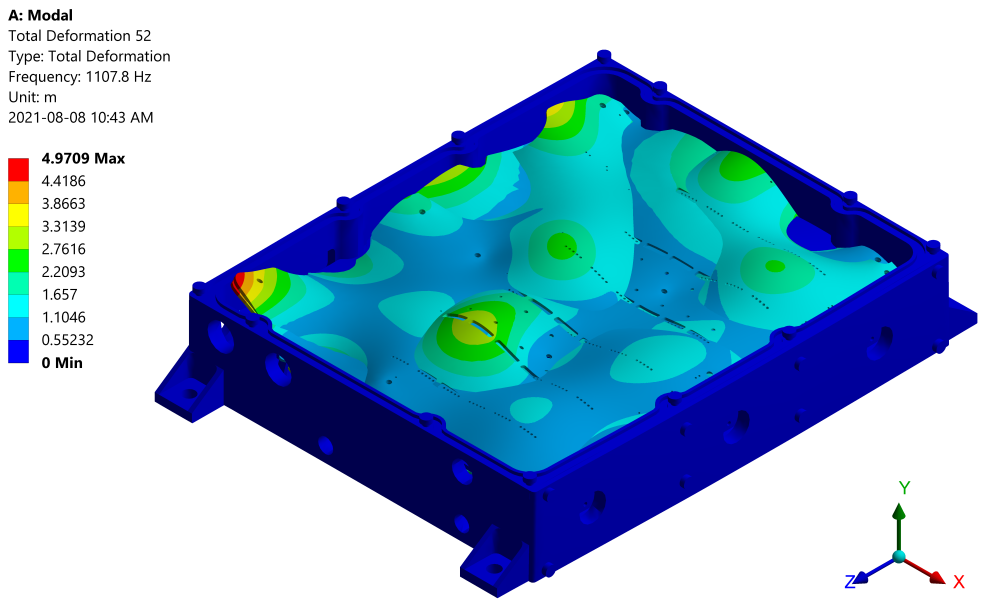

Figure 5.3: Modal analysis: Modal shape 56 with natural frequency of 1107.8 Hz, the gate driver has highest excitation -Y direction

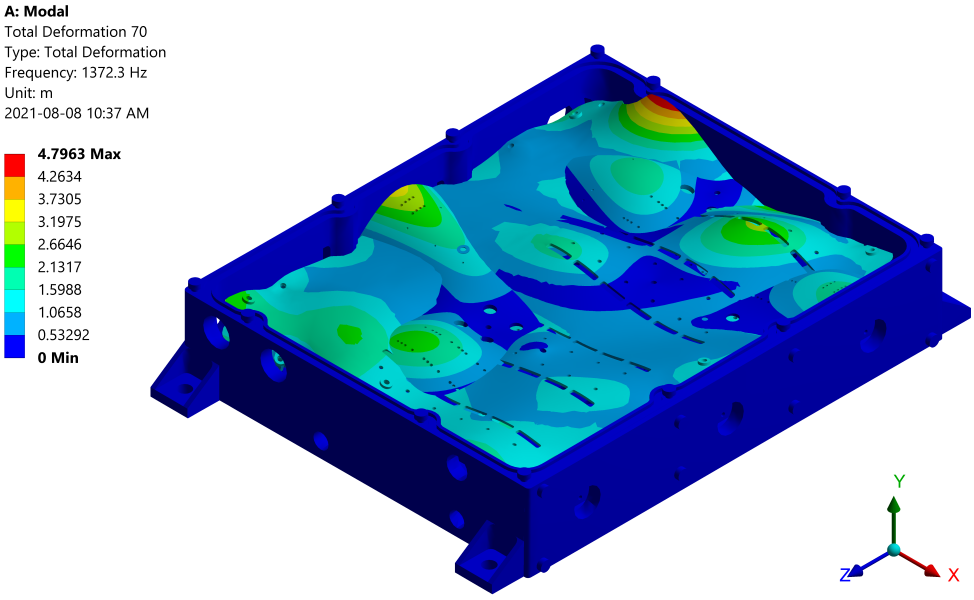

Figure 5.4: Modal analysis: Mode shape 70 with natural frequency of 1372.3 Hz, the aluminum shield highest excitation X direction

5.3 Harmonic Analysis

In order to determine the peak dynamic response of the inverter a harmonic analysis is conducted. In harmonic analysis the inverter is subjected to loads at various frequencies with a specified interval along with natural frequencies of the inverter. The maximum displacements and stresses at these frequencies are evaluated. For the purpose of this thesis frequencies in the sweeping range of up to 6.5 kHz are considered with loads corresponding to a maximum acceleration of 2.5 g in X, Y and Z directions.

The motivation behind a sweeping frequency range is to capture a wide range of excitation frequencies and magnitudes that the inverter could potentially be subjected to. This is because predicting the location and magnitude of all induced vibrations in a vehicle is extremely challenging.

The harmonic analysis conducted in this thesis for an inverter serves three main purposes:

- Ensure maximum displacement does not separate the rectangular fin base from the inverter housing where the coolant flows because this can cause the coolant to leak.
- Ensure minimum displacement on all PCBs so that they do not break or loose contact with other connected PCBs or components.
- Ensure that the stress observed due to resonance or otherwise on all inverter components does not exceed the yield stress of respective materials.

5.3.1 Harmonic Analysis Simulation results

Based on the criteria described above and due to the nature of the inverter assembly and failure modes, displacements in Y diction are most critical for the cooling system and also the PCBs. Figs 5.5 and 5.6 show the frequency vs amplitude of each component due to loads corresponding to 2.5 g of acceleration in Y direction.

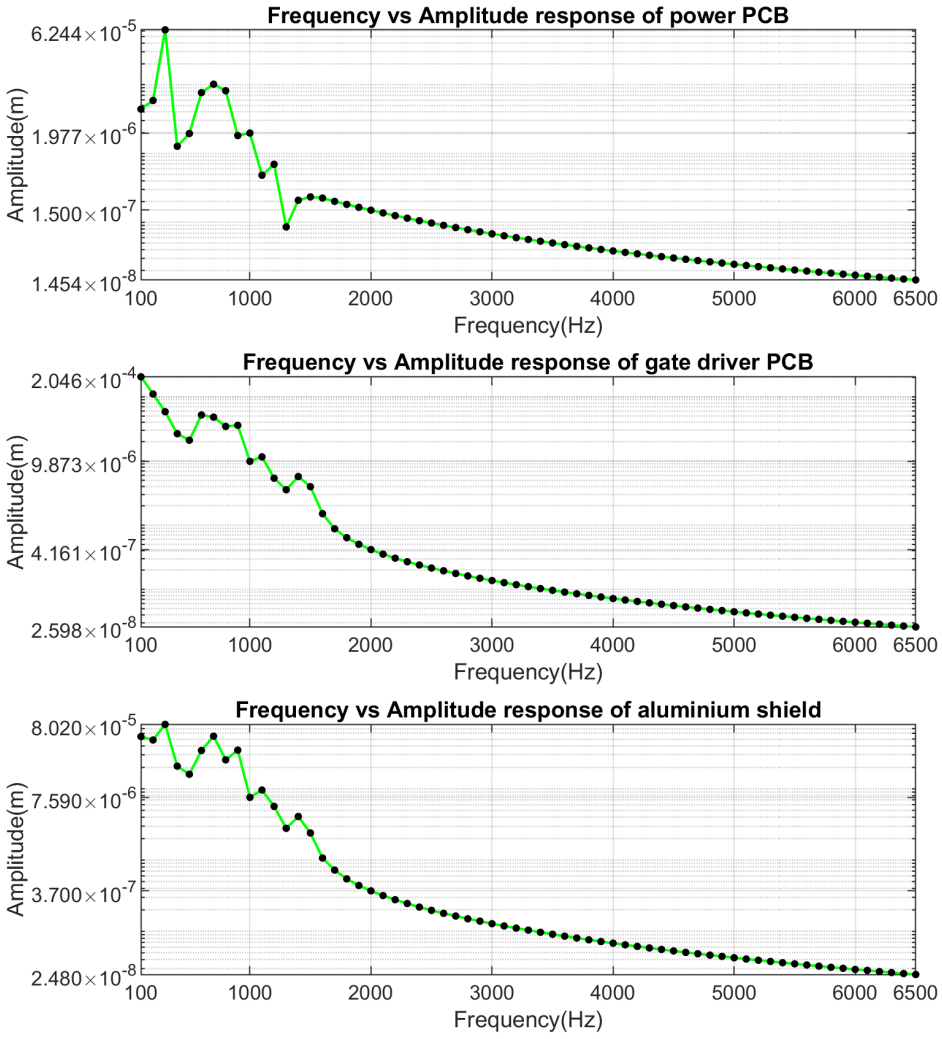

Figure 5.5: Frequency vs amplitude response of the power PCB, gate driver PCB and the aluminum shield respectively

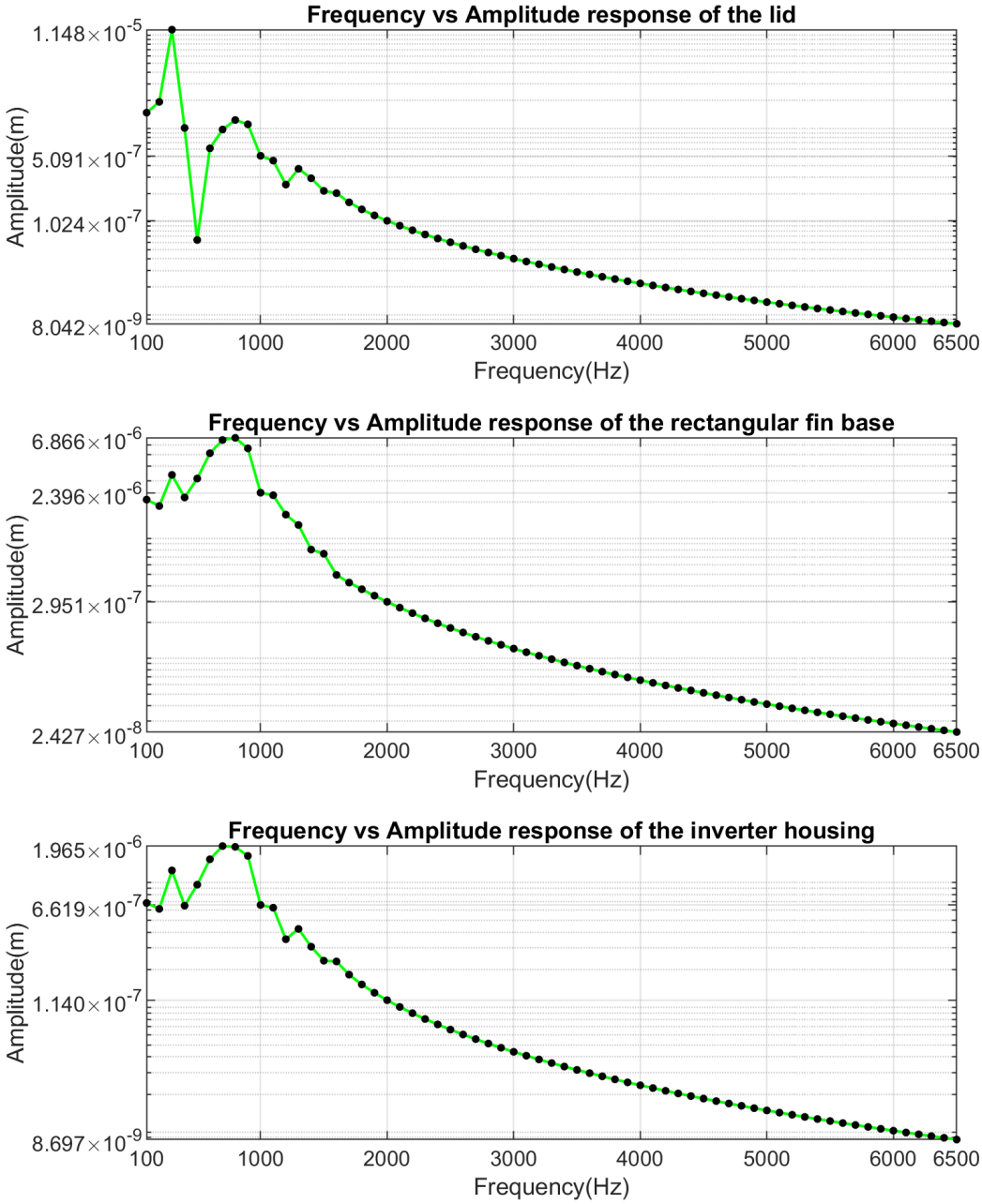

Figure 5.6: Frequency vs amplitude response of the lid, rectangular fin base and the aluminum housing respectively

Figs 5.7-5.12 show the maximum stress seen by each inverter component due to loads corresponding to a 2.5 g acceleration in Y direction

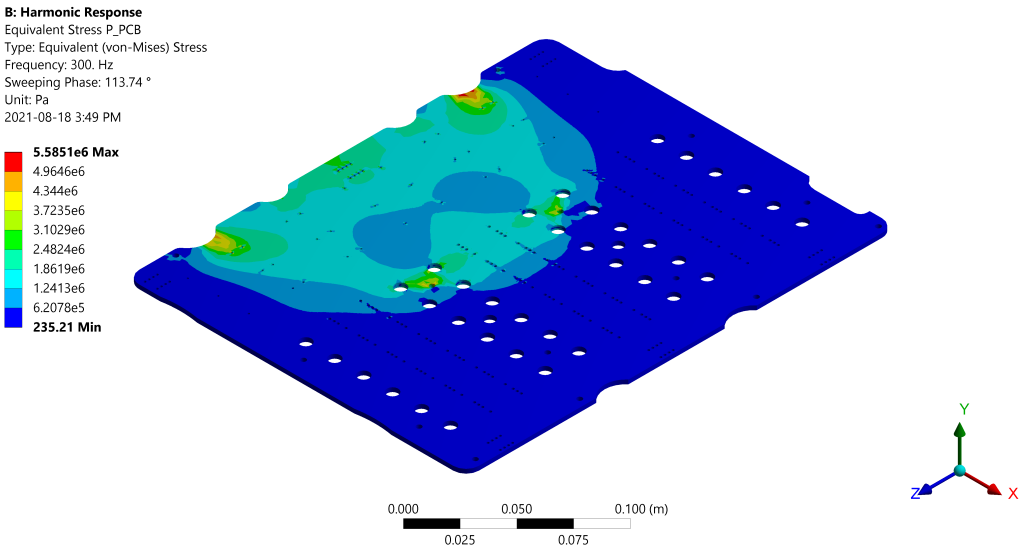

Figure 5.7: Contour plot of von-Miess stress in power PCB

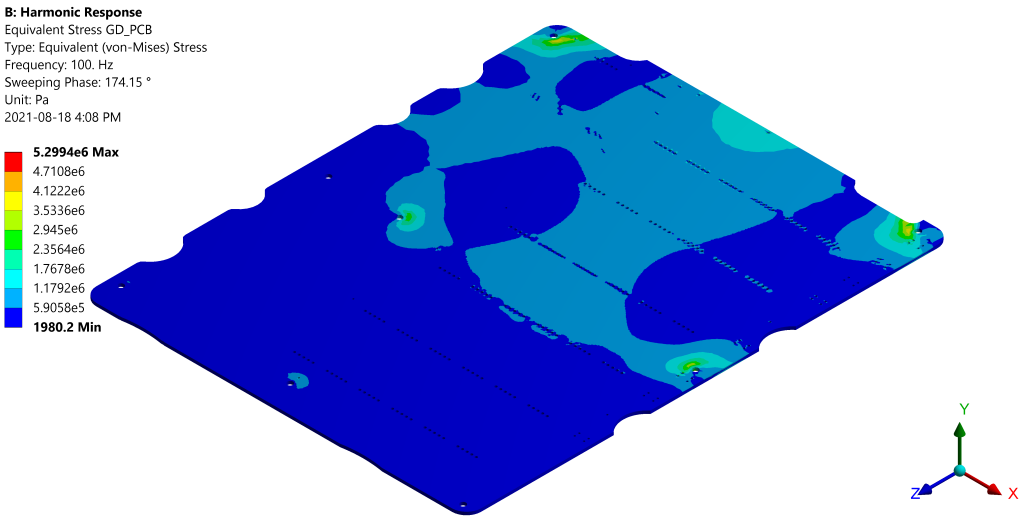

Figure 5.8: Contour plot of von-Miess stress in gate driver PCB

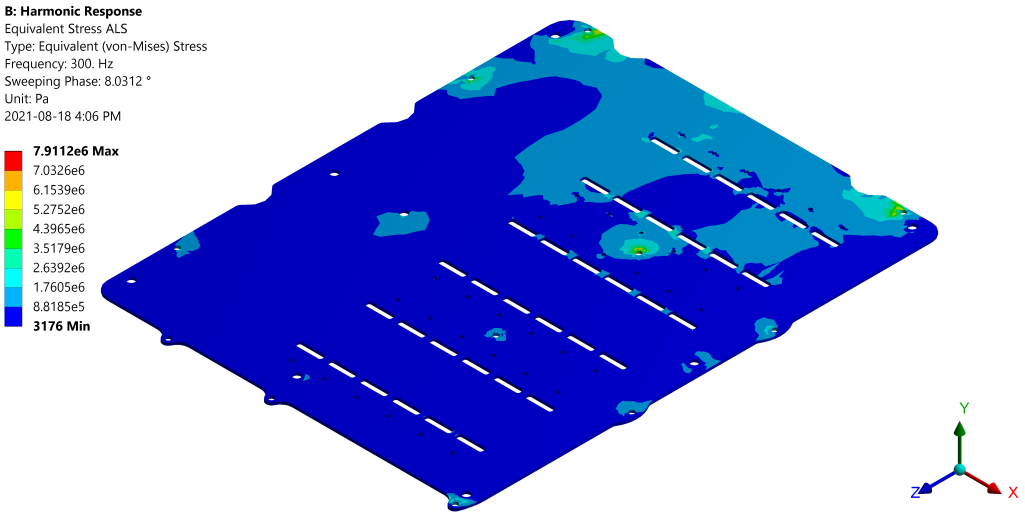

Figure 5.9: Contour plot of von-Miess stress in aluminium shield

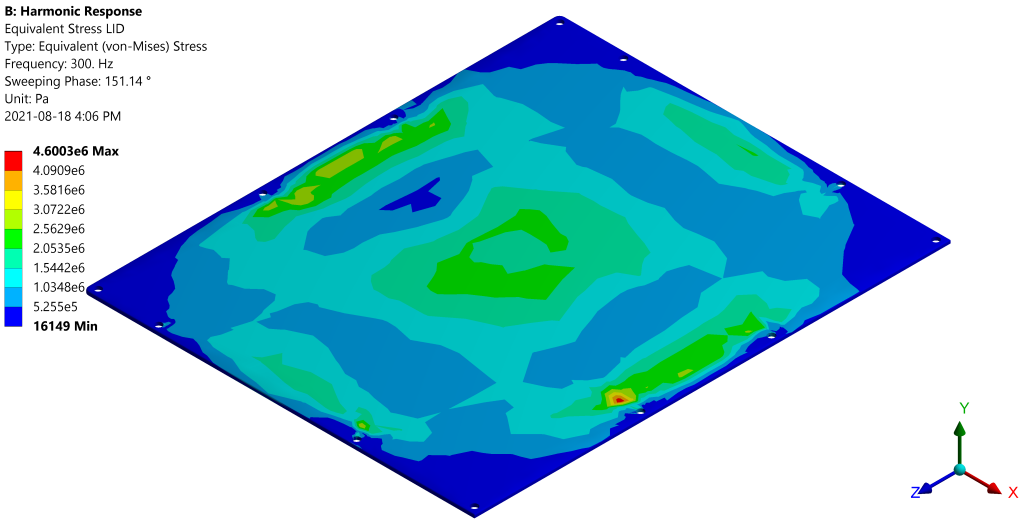

Figure 5.10: Contour plot of von-Miess stress in lid

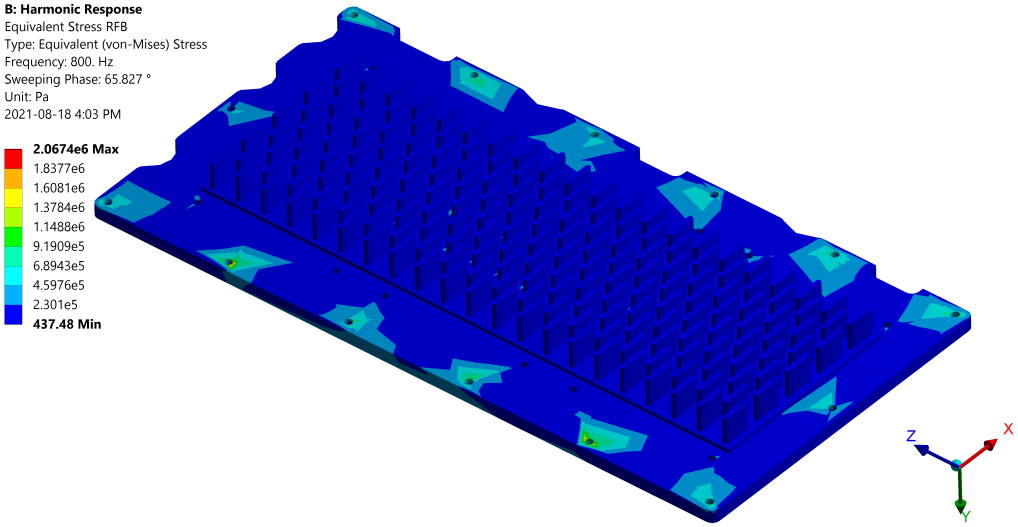

Figure 5.11: Contour plot of von-Miess stress in rectangular fin base

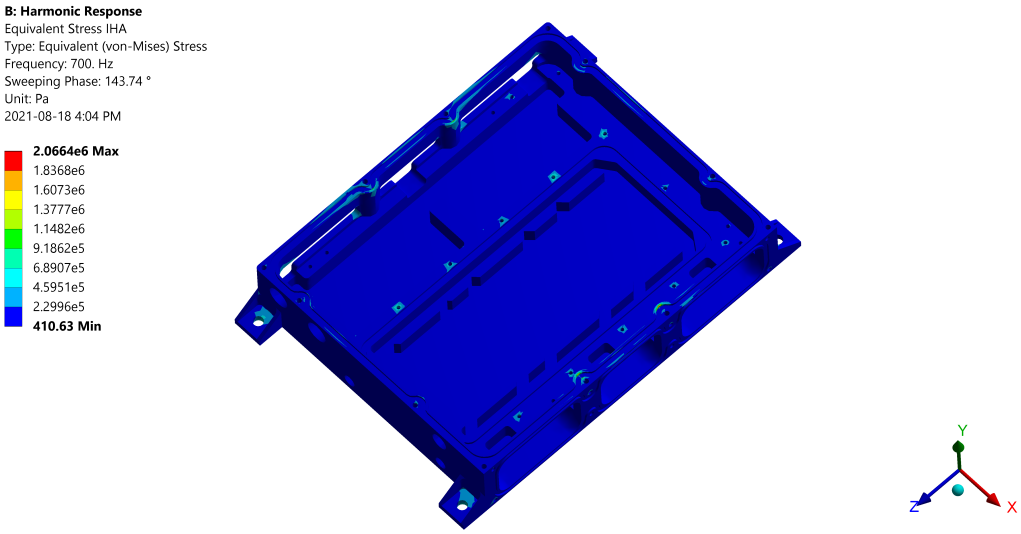

Figure 5.12: Contour plot of von-Miess stress in inverter housing

It is clear from the simulation results, summarized in Table 5.1 that the inverter components do not experience stresses and displacements beyond their yielding limits. Additionally, both modal and harmonic analysis are considered linear analysis, thus the magnitude of stresses and displacement are expected to increase linearly with an increase in the magnitude of the load.

Based on this relationship the inverter components can withstand stresses and displacements even if the acceleration load is four times higher (10 g) than the one shown in simulations. Lastly, the 120 kW ANPC inverter design presented satisfies the design criteria defied above, for loads corresponding to both 2.5 g and 10 g.

Table 5.1: CHS Summary of stress and displacements in each component for loads applied in Y direction

	Power PCB	Gate driver PCB	shield	Lid	Rectangular fin base	Inverter housing
Material	FR-4	FR-4	Al 6061-T6	Al 6061	Al 6061	Al 6061
Yield stress (Pa)	2.62×10^8	2.62×10^8	2.8×10^8	2.8×10^8	2.8×10^8	2.8×10^8
Max displacement (mm) for 2.5 g	0.0624	0.2046	0.0802	0.0115	0.0069	0.002
Max von-Misess (Pa) for 2.5 g	5.59×10^6	5.3×10^6	7.91×10^6	4.60×10^6	2.07×10^6	2.07×10^6
Max displacement (mm) for 10 g	0.2496	0.8184	0.3208	0.046	0.0276	0.008
Max von-Misess (Pa) for 10 g	2.24×10^7	2.52×10^7	6.16×10^7	1.84×10^7	$8.28 \times 10^{-}6$	8.28×10^6
Factor of safety for 2.5 g	46.8	49.4	35.3	60.8	126.5	135.2
Factor of safety for 10 g	11.6	10.3	4.5	15.2	33.8	33.8

Note that the analysis does not show stresses and displacements in fasteners and standoffs, this is because the stresses and displacements observed in the fasteners and standoffs are minimal compared to the other components.

5.4 Summary

A Modal analysis of the entire inverter housing is present along with harmonic analysis. The goal of the modal analysis is to determine the natural frequencies and the corresponding modal shapes. In general, it is ideal to avoid loading the inverter at the natural frequencies, however this is not always possible in a realistic scenario. Hence, a harmonic analysis is conducted in order to see the dynamic response of the inverter when it is vibrated at range of frequencies including the natural frequencies. The motivation and design criteria for the vibrational are presented for an automotive traction inverter. The 120kW ANPC inverter is simulated to ensure that the inverter housing can withstand vibrational loads of up to 10 g at frequencies of up to 6500 Hz without reaching the yield limit of any of the components, while satisfying the design criteria listed in this chapter.

Chapter 6

Conclusions and Future Work

6.1 Conclusion

The inverter is one of the most important components in an EV, and there are there are three main challenges to consider when designing an automotive traction inverter.

1. Designing an optimal thermal management solution for the necessary components.
2. Selecting inverter components that meet the desired specifications, allow high power density, enable efficient packaging and also utilize the least weight and volume.
3. Protecting the inverter components in the housing from external mechanical loads.

Components that are necessary, and make up an automotive traction inverter are presented in chapter 2. An extensive review of the existing technologies of these core components is discussed along with some of the challenges and benefits associated with incorporating these components in the inverter, in addition to the potential future trends.

Chapter three focuses on the first challenge- designing an optimal thermal management solution. The basics of thermal analysis is presented, along with some of the most important design criteria for an automotive thermal management system. The motivation behind each of these criteria is also discussed in detail. An optimal thermal management solution for a 120kW 3-level ANPC inverter is presented by combining an analytical equation driven approach with CFD analysis. Note that 120 kW 3-level ANPC inverter is designed using discrete SiC switches. The combination of analytical equation driven approach with CFD analysis yields a truly optimized design that fulfills each of the design criteria while minimizing design and computational efforts. This is in contrast to most thermal management designs which, are heavily dependant on only FEA based CFD analysis, thus making optimization extremely challenging and impractical.

Chapter four focuses on the second challenge- packaging and selecting the inverter components such that power density is increased. In an effort to improve power density, a 250 kW 2-level SiC power module based inverter is presented. The power module based inverter design helps in boosting the power density, however achieving a higher power density also requires thermal management for the DC-link capacitor.

A stacked cooling system is designed that utilizes one coolant block to provide thermal management for both the power module and the DC-link capacitor. The stacked cooling system is also optimized by combining analytical equation driven approach with CFD analysis. This enables the 2-level inverter to achieve a power density of 47 kW/L, while the 3-level ANPC inverter has a power density of 30.3 kW/L. Both of the presented inverters have the highest power density when compared to the inverters design seen in current literature.

Chapter five focuses on the third challenge- encasing the inverter components in a housing that can withstand external mechanical loads. The inverter is bound to experience vibrations while in operation. It is important to insure that these vibrations are not displacing the inverter components to the point where the stresses due to the displacement are beyond the yielding limit of the material in consideration.

Additionally, it is also necessary to make sure the displacements are not significant enough to move normally mated components far apart, for example separation of the lid from the housing. Thus important design criteria for an inverter housing design along with the motivation behind these criteria are presented and discussed in this chapter. A modal and harmonic analysis is conducted on the 120kW 3-level ANPC inverter housing to insure that the inverter design fulfills the presented design criteria. The analysis presented and discussed in this thesis is not mentioned or considered in any of literature at present that involves inverter design.

6.2 Future Work

6.2.1 Transient Thermal Modeling

The thermal management considered in this thesis was based on steady state, worst case analysis. This results in a robust design with high margin of error. However, performing a transient analysis can give important insights on how the thermal management will behave along with resulting junction temperatures during the startup of an EV or during instantaneous acceleration.

6.2.2 Real Time Electro-thermal model

A real time electro-thermal model can be used in drive cycle simulations of an EV to extract live junction temperature. The ability to access junction temperatures in real time also enables advanced switching techniques in multi-level inverter typologies where the coldest MOSFETs can conduct more currents, while the warmest ones conduct less current. This can help minimize losses, and ultimately boost efficiency.

6.2.3 NVH Analysis

Further vibrational analysis of the inverter housing can be conducted to determine the perceived noise generated by the inverter during nominal operation. Additionally, random vibration analysis and transient dynamic analysis of the inverter housing can also provide valuable insights of the inverter behaviour when it is subjected to non-linear loads.

References

[1] M. R. Ahmed, R. Todd, and A. J. Forsyth, "Analysis of sic mosfets under hard and soft-switching," in *2015 IEEE Energy Conversion Congress and Exposition (ECCE)*, 2015, pp. 2231–2238. DOI: 10.1109/ECCE.2015.7309974.

[2] S. Chowdhury, E. Gurpinar, and B. Ozpineci, "High-energy density capacitors for electric vehicle traction inverters," in *2020 IEEE Transportation Electrification Conference Expo (ITEC)*, 2020, pp. 644–650. DOI: 10.1109/ITEC48692.2020.9161588.

[3] S. Seal and H. A. Mantooth, "High performance silicon carbide power packaging past trends, present practices, and future directions," *Energies*, vol. 10, no. 3, 2017, ISSN: 1996-1073. DOI: 10.3390/en10030341. [Online]. Available: https://www.mdpi.com/1996-1073/10/3/341.

[4] A. D. Callegaro, J. Guo, M. Eull, B. Danen, J. Gibson, M. Preindl, B. Bilgin, and A. Emadi, "Bus bar design for high-power inverters," *IEEE Transactions on Power Electronics*, vol. 33, no. 3, pp. 2354–2367, 2018. DOI: 10.1109/TPEL.2017.2691668.

[5] H. Miyaki and Y. Mizutani, "Trend of high voltage harness technology that supports hybrid-electric vehicles," in *2007 Power Conversion Conference - Nagoya*, 2007, pp. 1346–1351. DOI: 10.1109/PCCON.2007.373139.

[6] B. Wu and M. Narimani, "Two-level voltage source inverter," in *High-Power Converters and AC Drives*. 2017, pp. 93–117. DOI: 10.1002/9781119156079.ch6.

[7] A. Choudhury, P. Pillay, and S. S. Williamson, "Comparative analysis between two-level and three-level dc/ac electric vehicle traction inverters using a novel dc-link voltage balancing algorithm," *IEEE Journal of Emerging and Selected Topics in Power Electronics*, vol. 2, no. 3, pp. 529–540, 2014. DOI: 10.1109/JESTPE.2014.2310140.

[8] S. Mukherjee, S. Kumar Giri, S. Kundu, and S. Banerjee, "A generalized discontinuous pwm scheme for three-level npc traction inverter with minimum switching loss for electric vehicles," *IEEE Transactions on Industry Applications*, vol. 55, no. 1, pp. 516–528, 2019. DOI: 10.1109/TIA.2018.2866565.

[9] Z. Chen, D. Boroyevich, and R. Burgos, "Experimental parametric study of the parasitic inductance influence on mosfet switching characteristics," in *The 2010 International Power Electronics Conference ECCE ASIA*, 2010, pp. 164–169. DOI: 10.1109/IPEC.2010.5543851.

[10] W. Zhou, X. Zhong, and K. Sheng, "High temperature stability and the performance degradation of sic mosfets," *IEEE Transactions on*

Power Electronics, vol. 29, no. 5, pp. 2329–2337, 2014. DOI: 10.1109/TPEL.2013.2283509.

[11] Z. Ni, X. Lyu, O. P. Yadav, and D. Cao, "Review of sic mosfet based three-phase inverter lifetime prediction," in *2017 IEEE Applied Power Electronics Conference and Exposition (APEC)*, 2017, pp. 1007–1014. DOI: 10.1109/APEC.2017.7930819.

[12] L. C. Yu, G. T. Dunne, K. S. Matocha, K. P. Cheung, J. S. Suehle, and K. Sheng, "Reliability issues of sic mosfets: A technology for high-temperature environments," *IEEE Transactions on Device and Materials Reliability*, vol. 10, no. 4, pp. 418–426, 2010. DOI: 10.1109/TDMR.2010.2077295.

[13] E. Ugur, F. Yang, S. Pu, S. Zhao, and B. Akin, "Degradation assessment and precursor identification for sic mosfets under high temp cycling," *IEEE Transactions on Industry Applications*, vol. 55, no. 3, pp. 2858–2867, 2019. DOI: 10.1109/TIA.2019.2891214.

[14] T. J. Han, J. Nagashima, S. J. Kim, S. Kulkarni, and F. Barlow, "High density 50 kw sic inverter systems using a jfet based six-pack power module," in *8th International Conference on Power Electronics - ECCE Asia*, 2011, pp. 764–769. DOI: 10.1109/ICPE.2011.5944668.

[15] M. Chinthavali, J. A. Tawfik, and R. V. Arimilli, "Design and analysis of a 55-kw air-cooled automotive traction drive inverter," in *2011 IEEE Energy Conversion Congress and Exposition*, 2011, pp. 2345–2352. DOI: 10.1109/ECCE.2011.6064080.

[16] B. Wrzecionko, D. Bortis, and J. W. Kolar, "A 120 °c ambient temperature forced air-cooled normally-off sic jfet automotive inverter system," *IEEE Transactions on Power Electronics*, vol. 29, no. 5, pp. 2345–2358, 2014. DOI: 10.1109/TPEL.2013.2294906.

[17] S. Sato, K. Matsui, Y. Zushi, Y. Murakami, S. Tanimoto, H. Sato, and H. Yamaguchi, "Forced-air-cooled 10 kw three-phase sic inverter with output power density of more than 20 kw/l," in *Silicon Carbide and Related Materials 2010*, ser. Materials Science Forum, vol. 679, Trans Tech Publications Ltd, Apr. 2011, pp. 738–741. DOI: 10.4028/www.scientific.net/MSF.679-680.738.

[18] Y. A. Ç. A. J. Ghajar, *Heat and mass transfer : fundamentals and applications*, 6th ed. Mcgraw-Hill Education, 2020.

[19] H. Bostanci, D. Van Ee, B. A. Saarloos, D. P. Rini, and L. C. Chow, "Spray cooling of power electronics using high temperature coolant and enhanced surface," in *2009 IEEE Vehicle Power and Propulsion Conference*, 2009, pp. 609–613. DOI: 10.1109/VPPC.2009.5289793.

[20] L.-J. Jiang, S.-L. Jiang, W.-L. Cheng, Y.-L. Nian, and R. Zhao, "Experimental study on heat transfer performance of a novel compact spray cooling module," *Applied Thermal Engineering*, vol. 154, pp. 150–156, 2019, ISSN: 1359-4311. DOI: https://doi.org/10.1016/j.applthermaleng.2019.03.078. [Online]. Available: https://www.sciencedirect.com/science/article/pii/S1359431118370078.

[21] L. C. Robert G. Mertens, R. B. C. Kalpathy B. Sundaram, L. T. Daniel P. Rini, and B. A. Saarloos, "Spray cooling of igbt devices," *ASME Journal of Electronics Packaging*, 2007.

[22] L. J. Turek, D. P. Rini, B. A. Saarloos, and L. C. Chow, "Evaporative spray cooling of power electronics using high temperature coolant," in *2008 11th Intersociety Conference on Thermal and Thermomechanical Phenomena in Electronic Systems*, 2008, pp. 346–351. DOI: 10.1109/ITHERM.2008.4544290.

[23] N. Souris, H. Liakos, and M. Founti, "Impinging jet cooling on concave surfaces," *AIChE Journal*, vol. 50, no. 8, pp. 1672–1683, 2004. DOI: https://doi.org/10.1002/aic.10171. eprint: https://aiche.onlinelibrary.wiley.com/doi/pdf/10.1002/aic.10171. [Online]. Available: https://aiche.onlinelibrary.wiley.com/doi/abs/10.1002/aic.10171.

[24] J. Jörg, S. Taraborrelli, G. Sarriegui, R. W. De Doncker, R. Kneer, and W. Rohlfs, "Direct single impinging jet cooling of a mosfet power electronic module," *IEEE Transactions on Power Electronics*, vol. 33, no. 5, pp. 4224–4237, 2018. DOI: 10.1109/TPEL.2017.2720963.

[25] K. Gould, S. Q. Cai, C. Neft, and A. Bhunia, "Liquid jet impingement cooling of a silicon carbide power conversion module for vehicle applications," *IEEE Transactions on Power Electronics*, vol. 30, no. 6, pp. 2975–2984, 2015. DOI: 10.1109/TPEL.2014.2331562.

[26] UmitedSiC, *Uj4c075018k4s,750v-18 mili ohm sic fet*, version A, Oct. 2020. [Online]. Available: https://unitedsic.com/datasheets/DS_UJ4C075018K4S.pdf.

[27] D. Bergogne, H. Morel, D. Planson, D. Tournier, P. Bevilacqua, B. Allard, R. Meuret, S. Vieillard, S. Rael, and F. MeibodyTabar, "Towards an airborne high temperature sic inverter," in *2008 IEEE Power Electronics Specialists Conference*, 2008, pp. 3178–3183. DOI: 10.1109/PESC.2008.4592442.

[28] G. Müller, G. Krötz, and E. Niemann, "Sic for sensors and high-temperature electronics," *Sensors and Actuators A: Physical*, vol. 43, no. 1, pp. 259–268, 1994, ISSN: 0924-4247. DOI: https://doi.org/10.1016/0924-4247(93)00684-V. [Online]. Available: https://www.sciencedirect.com/science/article/pii/092442479300684V.

[29] K. Sheng, "Maximum junction temperatures of sic power devices," *IEEE Transactions on Electron Devices*, vol. 56, no. 2, pp. 337–342, 2009. DOI: 10.1109/TED.2008.2010605.

[30] H. Lu, C. Bailey, and C. Yin, "Design for reliability of power electronics modules," *Microelectronics Reliability*, vol. 49, no. 9, pp. 1250–1255, 2009, 20th European Symposium on the Reliability of Electron Devices, Failure Physics and Analysis, ISSN: 0026-2714. DOI: https://doi.org/10.1016/j.microrel.2009.07.055. [Online]. Available: https://www.sciencedirect.com/science/article/pii/S0026271409003084.

[31] J. Mistry, Y. Wang, P. Azer, and B. Bilgin, "Design of a compact thermal management system for a high-power silicon carbide traction inverter," SAE Technical Paper, Tech. Rep., 2021.

[32] M. Musallam, C. Yin, C. Bailey, and M. Johnson, "Mission profile-based reliability design and real-time life consumption estimation in power electronics," *IEEE Transactions on Power Electronics*, vol. 30, no. 5, pp. 2601–2613, 2015. DOI: 10.1109/TPEL.2014.2358555.

[33] Lars. (2020). "Using tesla thermal management system parts." Accessed on 06.25.2021, [Online]. Available: https://www.evcreate.nl/using-tesla-thermal-management-system-parts/.

[34] M. Mruzek, I. Gajdáč, Ľ. Kučera, and D. Barta, "Analysis of parameters influencing electric vehicle range," *Procedia Engineering*, vol. 134, pp. 165–174, 2016, TRANSBALTICA 2015: PROCEEDINGS OF THE 9th INTERNATIONAL SCIENTIFIC CONFERENCE. May 7–8, 2015. Vilnius Gediminas Technical University, Vilnius, Lithuania., ISSN: 1877-7058. DOI: https://doi.org/10.1016/j.proeng.2016.01.056. [Online]. Available: https://www.sciencedirect.com/science/article/pii/S187770581600059X.

[35] C.-S. N. Shiau, C. Samaras, R. Hauffe, and J. J. Michalek, "Impact of battery weight and charging patterns on the economic and environmental benefits of plug-in hybrid vehicles," *Energy Policy*, vol. 37, no. 7, pp. 2653–2663, 2009, ISSN: 0301-4215. DOI: https://doi.org/10.1016/j.enpol.2009.02.040. [Online]. Available: https://www.sciencedirect.com/science/article/pii/S0301421509001402.

[36] P. Gerhart, J. Hochstein, and A. Gerhart, *Munson, Young and Okiishi's Fundamentals of Fluid Mechanics*. Wiley, 2020, ISBN: 9781119597308. [Online]. Available: https://books.google.ca/books?id=F6ALEAAAQBAJ.

[37] L. F. Moody, "Friction factors for pipe flow," *Transactions of the ASME*, 1944.

[38] S. E. Haaland, "Simple and explicit formulas for the friction factor in turbulent pipe flow," 1983.

[39] T.-G. Technology, *Tg-a1660 ultra soft thermal pad*, 20200501, version 17. [Online]. Available: https://www.tglobaltechnology.com/wp-content/uploads/2019/07/TG-A1660-3.pdf.

[40] W. A. Khan, J. R. Culham, and M. M. Yovanovich, "The Role of Fin Geometry in Heat Sink Performance," *Journal of Electronic Packaging*, vol. 128, no. 4, pp. 324–330, Feb. 2006, ISSN: 1043-7398. DOI: 10.1115/1.2351896. eprint: https://asmedigitalcollection.asme.org/electronicpackaging/article-pdf/128/4/324/6625116/324_1.pdf. [Online]. Available: https://doi.org/10.1115/1.2351896.

[41] D. Soodphakdee, M. Behnia, and D. W. Copeland, "A comparison of fin geometries for heatsinks in laminar forced convection—part i: Round, elliptical, and plate fins in staggered and in-line configurations," *The International Journal of Microcircuits and Electronic Packaging*, vol. 24, no. 1, pp. 68–76, 2001.

[42] A. Bejan and A. M. Morega, "Optimal Arrays of Pin Fins and Plate Fins in Laminar Forced Convection," *Journal of Heat Transfer*, vol. 115, no. 1, pp. 75–81, Feb. 1993, ISSN: 0022-1481. DOI: 10.1115/1.2910672.

eprint: https://asmedigitalcollection.asme.org/heattransfer/article-pdf/115/1/75/5745688/75_1.pdf. [Online]. Available: https://doi.org/10.1115/1.2910672.

[43] A. Bejan, *Entropy Generation Minimization: The Method of Thermodynamic Optimization of Finite-Size Systems and Finite-Time Processes*, ser. Mechanical and Aerospace Engineering Series. Taylor & Francis, 1995, ISBN: 9780849396519. [Online]. Available: https://books.google.ca/books?id=pP6cZkun4VoC.

[44] A. Bejan and J. Kestin, "Entropy Generation Through Heat and Fluid Flow," *Journal of Applied Mechanics*, vol. 50, no. 2, pp. 475–475, Jun. 1983, ISSN: 0021-8936. DOI: 10.1115/1.3167072. eprint: https://asmedigitalcollection.asme.org/appliedmechanics/article-pdf/50/2/475/5456977/475_2.pdf. [Online]. Available: https://doi.org/10.1115/1.3167072.

[45] E. M. Sparrow, J. P. Abraham, and J. C. Tong, "Archival correlations for average heat transfer coefficients for non-circular and circular cylinders and for spheres in cross-flow," *International Journal of Heat and Mass Transfer*, vol. 47, no. 24, pp. 5285–5296, 2004, ISSN: 0017-9310. DOI: https://doi.org/10.1016/j.ijheatmasstransfer.2004.06.024. [Online]. Available: https://www.sciencedirect.com/science/article/pii/S0017931004002686.

[46] T. H. Chilton and A. P. Colburn, "Mass transfer (absorption) coefficients prediction from data on heat transfer and fluid friction," *Industrial & Engineering Chemistry*, vol. 26, no. 11, pp. 1183–1187, 1934. DOI: 10.

1021/ie50299a012. eprint: https://doi.org/10.1021/ie50299a012. [Online]. Available: https://doi.org/10.1021/ie50299a012.

[47] Y. E. H., "Convection heat transfer and pressure drop of air flowing across triangular pitch banks of finned tubes," *AIChE Chem. Eng. Prog. Symp. Sen*, vol. 59, 1965.

[48] W. R. L., "Air-side heat transfer in finned tube heat exchangers," *Heal Transfer Eng*, vol. 1, 1980.

[49] G. E. D., "Correlation and utilization of new data on flow resistance and heat transfer for crossflow of gases over tube banks," *Trans. ASME*, vol. 54, 1937.

[50] J. S. L., "Tube spacing in finned tube banks," *Trans.ASME*, vol. 67, 1945.

[51] A. NIR, "Heat transfer and friction factor correlations for crossflow over staggered finned tube banks," *Heat Transfer Engineering*, vol. 12, no. 1, pp. 43–58, 1991. DOI: 10.1080/01457639108939746. eprint: https://doi.org/10.1080/01457639108939746. [Online]. Available: https://doi.org/10.1080/01457639108939746.

[52] R. T. J., "Heat transfer and pressure drop of typical air cooler finned tubes," *Trans. ASME*, vol. 107, 1985.

[53] W. C., "Correlations ease the selection of finned tubes," *Oil and Gas J*, 1976.

[54] S. E. A., "Heat transfer coefficients and other data on individual serrated-finned surfaces," *Trans. ASME*, vol. 67, 1945.

[55] Y. E. H., "Heat transfer and pressure drops of air in forced convection across triangular pitch banks of finned tubes," *AIChE Chem. Eng. Prog. Symp. Ser*, vol. 55, 1959.

[56] H. K., "Heat transfer and pressure drop characteristics of finned tubes in crossflow," *Heat Transfer Eng*, vol. 2, 1981.

[57] S. W. A., "General correlation of friction factor for surfaces in crossflow," *Trans. ASME*, vol. 67, 1945.

[58] H. S. Seo and D. Shin, "Development of parallel and direct cooling system for ev/fcev inverter," in *WCX World Congress Experience*, SAE International, Apr. 2018. DOI: https://doi.org/10.4271/2018-01-0454. [Online]. Available: https://doi.org/10.4271/2018-01-0454.

[59] C. Qian, A. M. Gheitaghy, J. Fan, H. Tang, B. Sun, H. Ye, and G. Zhang, "Thermal management on igbt power electronic devices and modules," *IEEE Access*, vol. 6, pp. 12 868–12 884, 2018. DOI: 10.1109/ACCESS.2018.2793300.

[60] D. Rahman, A. J. Morgan, Y. Xu, R. Gao, W. Yu, D. C. Hopkins, and I. Husain, "Design methodology for a planarized high power density ev/hev traction drive using sic power modules," in *2016 IEEE Energy Conversion Congress and Exposition (ECCE)*, 2016, pp. 1–7. DOI: 10.1109/ECCE.2016.7855018.

[61] C. Buttay, J. Rashid, C. Mark Johnson, P. Ireland, F. Udrea, G. Amaratunga, and R. K. Malhan, "High performance cooling system for automotive inverters," in *2007 European Conference on Power*

Electronics and Applications, 2007, pp. 1–9. DOI: 10.1109/EPE.2007.4417363.

[62] F. Xu, T. J. Han, D. Jiang, L. M. Tolbert, F. Wang, J. Nagashima, S. J. Kim, S. Kulkarni, and F. Barlow, "Development of a sic jfet-based six-pack power module for a fully integrated inverter," *IEEE Transactions on Power Electronics*, vol. 28, no. 3, pp. 1464–1478, 2013. DOI: 10.1109/TPEL.2012.2205946.

[63] Y. Hinata, M. Horio, Y. Ikeda, R. Yamada, and Y. Takahashi, "Full sic power module with advanced structure and its solar inverter application," in *2013 Twenty-Eighth Annual IEEE Applied Power Electronics Conference and Exposition (APEC)*, 2013, pp. 604–607. DOI: 10.1109/APEC.2013.6520272.

[64] W. Chou, A. Kempitiya, and O. Vodyakho, "Reduction of power losses of sic mosfet based power modules in automotive traction inverter applications," in *2018 IEEE Transportation Electrification Conference and Expo (ITEC)*, 2018, pp. 1035–1038. DOI: 10.1109/ITEC.2018.8450130.

[65] F. Carastro, Z. Chen, A. Streibel, and O. Muehlfeld, "Dcm™1000x – automotive power module technology platform optimized for sic traction inverters," in *2021 IEEE Applied Power Electronics Conference and Exposition (APEC)*, 2021, pp. 2364–2368. DOI: 10.1109/APEC42165.2021.9487446.

[66] A. Bubert, K. Oberdieck, H. Xu, and R. W. De Doncker, "Experimental validation of design concepts for future ev-traction inverters," in *2018*

IEEE Transportation Electrification Conference and Expo (ITEC), 2018, pp. 795–802. DOI: 10.1109/ITEC.2018.8450253.

[67] Y. Wang, J. Mistry, P. Azer, and B. Bilgin, "Integrated busbar design for stray inductance and volume reduction in a high-power sic traction inverter," SAE Technical Paper, Tech. Rep., 2021.